# MODAL DAMPING PREDICTION FOR VIBRATING SOLIDS: CONSTITUTIVE MODELS AND FINITE ELEMENT COMPUTATIONS

*Thesis submitted to the*
*Indian Institute of Technology, Kharagpur*
*For award of the degree*

*of*

**Doctor of Philosophy**

*by*

**Prasun Jana**

Under the guidance of

**Dr. Anindya Chatterjee**

and

**Dr. Anirvan DasGupta**

**DEPARTMENT OF MECHANICAL ENGINEERING**
**INDIAN INSTITUTE OF TECHNOLOGY, KHARAGPUR**
**SEPTEMBER 2013**

**© 2013, Prasun Jana. All rights reserved.**

# CERTIFICATE OF APPROVAL

Date:____________

Certified that the thesis entitled **“Modal Damping Prediction for Vibrating Solids: Constitutive Models and Finite Element Computations”** submitted by **Prasun Jana** to Indian Institute of Technology, Kharagpur, for the award of the degree of Doctor of Philosophy has been accepted by the external examiners and that the student has successfully defended the thesis in the viva-voce examination held today.

Signature
Dr. Vikranth Racherla
(Member of the DSC)

Signature
Dr. A. K. Samantaray
(Member of the DSC)

Signature
Dr. Arghya Deb
(Member of the DSC)

Signature
Dr. Anindya Chatterjee
(Supervisor)

Signature
Dr. Anirvan DasGupta
(Supervisor)

Signature
Name:_______________
(External Examiner)

Signature
Name:_______________
(Chairman)

# CERTIFICATE

This is to certify that the thesis entitled **"Modal Damping Prediction for Vibrating Solids: Constitutive Models and Finite Element Computations"** submitted by **Prasun Jana** to Indian Institute of Technology, Kharagpur, is a record of bona fide research work under our supervision and is worthy of consideration for the award of the degree of Doctor of Philosophy of the Institute.

| | |
|---|---|
| Dr. Anindya Chatterjee<br>Professor<br>Mechanical Engineering Department<br>IIT Kanpur<br>(Supervisor) | Dr. Anirvan DasGupta<br>Professor<br>Mechanical Engineering Department<br>IIT Kharagpur<br>(Supervisor) |

Date:

# Declaration

I certify that

(a) the work contained in this thesis is original and has been done by me under the guidance of my supervisor(s).

(b) the work has not been submitted to any other Institute for any degree or diploma.

(c) I have followed the guidelines provided by the Institute in preparing the thesis.

(d) I have conformed to the norms and guidelines given in the Ethical Code of Conduct of the Institute.

(e) whenever I have used materials (data, theoretical analysis, figures, and text) from other sources, I have given due credit to them by citing them in the text of the thesis and giving their details in the references. Further, I have taken permission from the copyright owners of the sources, whenever necessary.

Signature of the Student

**Dedicated to**

**my**

**family**

# Acknowledgments

Completing my PhD degree is probably the most rewarding and challenging activity of my life so far. Without the support of several people, completion of this thesis would not be possible. I would like to express my sincerest thanks and appreciation to all of them.

First and foremost, I would like to express my sincerest gratitude to Dr. Anindya Chatterjee, my primary thesis advisor, for his guidance, motivation, enthusiasm, and immense support. I deeply appreciate his devotion to his students' education and success. What I learned from him over these past four years is not just how to pursue academic research, but how to view this world in a new prospective.

I also extend my heartfelt thanks to Dr. Anirvan DasGupta for his supervision during the last one year when Dr. Chatterjee left the institute to join IIT Kanpur. I am deeply grateful to him for his excellent support, both academic and otherwise, towards completion of this thesis.

In addition, I would like to thank Dr. Vikranth Racherla, Dr. Arghya Deb, Dr. A K Samantaray, and Dr. Ranjan Bhattacharya at IIT Kharagpur, and Dr. Anurag Gupta at IIT Kanpur for their kind help and valuable suggestions during various phases of my PhD work.

I also thank Dr. K Bhaskar, my master's thesis supervisor at IIT Madras, for encouraging me to join this PhD program. It was a tough decision for me to go for a regular PhD after five years in industry. I thank him for helping me to take this right decision.

I must thank Department of Mechanical Engineering, IIT Kharagpur and Department of Mechanical Engineering, IIT Kanpur for providing me all the facilities needed for completing my PhD work. I also want to thank Department of Science and Technology, India for providing financial support.

My friends in IIT Kharagpur and IIT Kanpur were sources of laughter, joy, and support. Special thanks go to Kuntal, Anupam, Uttam, Mukul, Rajesh, Sankar, Souvik, Tanmay, Arindam, and Ganesh in IIT kharagpur, Pankaj, Anshul, Saurabh, and Alakesh da in IIT Kanpur. Without you life would have been difficult.

I owe a lot to each and every member of my family, who encouraged and supported me at every stage of my personal and academic life. However, I would like to acknowledge two important people here: my wife, Ranjana and my little son, Praneet. I thank Ranjana for everything. This thesis would not have been possible without her love, kindness and support. I thank Praneet for being a constant source of inspiration for me. His contribution in this thesis is the greatest! Finally, I would like to dedicate this work to my late father whom I lost in a street accident in my childhood. I hope that this work makes him proud.

# Abstract

First principles prediction of the internal vibration damping of engineering components is not routine in finite element packages. With such predictions, designers would be able to assess the noise and vibration levels in engineering systems right from the component design stage. To this end, we revisit the modelling of internal material dissipation under spatially variable triaxial stresses, a research topic that peaked five decades ago but bears reexamination in view of modern computational power.

Internal energy dissipation in many materials, per stress cycle and per unit volume, is known to be frequency-independent and proportional to some power ($m \geq 2$) of a suitable equivalent stress amplitude ($D = \xi \sigma_{eq}^m$). Definition of this equivalent stress amplitude under arbitrary triaxial stress states remains an open question. Such a definition is needed for computing modal damping of arbitrary solid bodies using finite element packages.

In this thesis we develop macroscopic damping constitutive relations, for arbitrary triaxial time-harmonic stresses, by first considering numerous randomly dispersed microscopic dissipation sites. The resulting dissipation models are used in finite element prediction of modal damping in solid objects.

Constrained by empirical evidence, we consider two mathematically simple rate-independent dissipative phenomena in our assumed micromechanical dissipation models: (i) Coulomb friction, and (ii) ambient-temperature plasticity. The first case is a flat crack in an elastic material, with Coulomb friction between the crack faces. The second case involves dissipation due to microscopic elasto-plastic flaws.

For the first model, the macroscopic dissipation is obtained by Monte Carlo averaging of the dissipation from many randomly oriented non-interacting microcracks, and finally fitted using a multivariate polynomial. In the second model, namely distributed microscopic elasto-plastic flaws, we find two limiting special cases that are analytically tractable: spherical flaws, and flaws that are flat and thin. In each of these cases we assume a random distribution of flaw strengths and orientations, and a formula for the macroscopic dissipation is obtained analytically (for spherical flaws) or semi-analytically (for flat and thin flaws). For spherical flaws, the averaged dissipation is governed exactly by the distortional strain energy. For flat and thin flaws, when $m$ is between 2 and about 6, the net dissipation is accurately, but not in general exactly, described by a power of the distortional strain energy.

We finally suggest that for engineering modeling purposes of metallic structures, for moderate $m$, a simple power law based on the distortional strain energy might be reasonable. We demonstrate use of this dissipation model for finite element computation of the modal damping ratios of arbitrary solid objects using both solid and shell elements in ANSYS. The results are then verified with known analytical results for the cases of several analytically tractable geometries. An interesting aspect of these damping results is that the modal damping ratios show a variation of over one order of magnitude over the cases we have considered. Torsion dominated modes have high damping and the purely radial mode of a solid sphere has low damping. We also verify that, at least in some cases, deliberately induced stress concentrations can lead to improved damping for materials where $m > 2$.

**Keywords**: Vibration damping, internal dissipation, frictional microcrack, Monte Carlo, elasto-plastic flaw, inclusion, plasticity, distortional strain energy, effective damping ratio

# Contents

**Title page** i

**Acknowledgments** xi

**Abstract** xiii

**Nomenclature** xix

**List of Figures** xxi

**List of Tables** xxix

**1 Introduction** 1

1.1 Material damping and relevant prior work . . . 3

1.2 Contributions of the thesis . . . 8

1.3 Outline of the thesis . . . 12

**2 Modal damping via dissipation from frictional microcracks** 13

2.1 Introduction . . . 13

2.2 Frictional dissipation in a single microcrack . . . 15

2.2.1 Finite element simulations . . . 18

2.2.2 Dissipation formula using a spring-block system . . . 19

2.3 Dissipation due to multiple cracks: Monte Carlo method . . . 20

2.3.1 Random orientations . . . 22

2.3.2 Nondimensionalization . . . 23

2.3.3 Building block: a single average dissipation calculation . . . 25

2.4 Fitted formula . . . . . 28
2.4.1 A comment on prior efforts . . . . . 28
2.4.2 Inputs to the fitted multivariate polynomial formula . . . . . 29
2.4.3 Multivariate polynomial fit . . . . . 29
2.5 Finite element computation of modal damping . . . . . 35
2.5.1 Effective damping ratio ($\zeta_{eff}$) . . . . . 36
2.5.2 Finite element prediction of effective damping ratio . . . . . 37
2.5.3 Details of $\zeta_{eff}$ computation using ANSYS . . . . . 38
2.5.4 Results for an arbitrary solid object . . . . . 41
2.6 Summary . . . . . 44

**3 Dissipation due to individual microscopic elasto-plastic flaws 47**
3.1 Introduction . . . . . 47
3.2 Unidimensional dissipation model . . . . . 47
3.3 Elasto-plastic inclusion under far-field stresses . . . . . 50
3.3.1 Finite element calculation . . . . . 50
3.3.2 Semi-analytical approach . . . . . 57
3.4 Two special cases . . . . . 62
3.4.1 Spherical inclusions . . . . . 62
3.4.2 Flat and thin ellipsoidal flaws . . . . . 66
3.5 Summary . . . . . 69

**4 Macroscopic dissipation due to dispersed elasto-plastic flaws 71**
4.1 Introduction . . . . . 71
4.2 Spherical flaws . . . . . 72
4.3 Flat and thin flaws . . . . . 73
4.3.1 Averaging over a single plane orientation . . . . . 74
4.3.2 Averaging over plane orientations . . . . . 74
4.3.3 Dissipation: Special cases and symmetries . . . . . 77
4.3.4 Relation to distortional strain energy . . . . . 78
4.3.5 Approximation for large $m$ . . . . . 81

4.4 Summary . . . 84

5 Modal damping computation examples with solid and shell elements 85

5.1 Introduction . . . 85

5.2 Computation of $\zeta_{eff}$ using solid elements . . . 86

5.2.1 Validation of $\zeta_{eff}$ computation with known analytical results . 87

5.3 Computation of $\zeta_{eff}$ using shell elements . . . 91

5.3.1 Analysis method . . . 91

5.3.2 Comparison with known analytical results . . . 93

5.4 Normalization for $m > 2$ . . . 94

5.5 Matlab GUI for automated computation of $\zeta_{eff}$ . . . 96

5.6 Effects of stress concentration on damping . . . 96

5.7 Summary . . . 100

6 Conclusions 101

A Supplementary materials for Chapter 2 105

A.1 On possible waveforms within the dissipation calculation . . . 105

A.2 Simulation results from 2D finite element analysis . . . 105

A.3 The dissipation formula from the spring block model . . . 109

A.3.1 Case 1: zero mean normal stress ($\beta = 0$) . . . 110

A.3.2 Case 2: $-1 < \beta < 1$ . . . 110

A.3.3 Case 3: $\beta < -1$ . . . 111

A.3.4 Case 4: $\beta > 1$ . . . 111

A.3.5 Single formula . . . 111

A.4 Simulation results from 3D finite element analysis . . . 112

A.4.1 Circular crack . . . 112

A.4.2 Triangular crack . . . 114

A.5 Matrix **B** for the constitutive model . . . 118

A.6 Brief review of some topics in vibration theory . . . 118

A.6.1 Response of a typical damped harmonic oscillator . . . . . . . 118

A.6.2 Modal damping . . . . . . . . . . . . . . . . . . . . . . . . . 119

**B Supplementary materials for Chapter 3 123**

B.1 Eshelby tensor for an ellipsoidal inclusion . . . . . . . . . . . . . . . . . 123

B.2 Details of 6 × 6 matrices **G** and **H** . . . . . . . . . . . . . . . . . . . . 125

**C Supplementary materials for Chapter 4 127**

C.1 $D$ from Eq. (4.10) for even integer $m$ . . . . . . . . . . . . . . . . . . . 127

C.2 Mathematical details of the large $m$ approximation . . . . . . . . . . . 128

C.2.1 Corrections terms for $\chi = 0$ or 1 . . . . . . . . . . . . . . . . . . 129

**D Supplementary materials for Chapter 5 131**

D.1 Torsion of a circular rod . . . . . . . . . . . . . . . . . . . . . . . . . . 131

D.1.1 Analytical calculation . . . . . . . . . . . . . . . . . . . . . . . . 131

D.1.2 Finite element computations of $\zeta_{eff}$ . . . . . . . . . . . . . . . 132

D.2 Bending of a thin rectangular plate . . . . . . . . . . . . . . . . . . . . 134

D.2.1 Analytical approach . . . . . . . . . . . . . . . . . . . . . . . . . 134

D.2.2 Computational solution . . . . . . . . . . . . . . . . . . . . . . . 136

D.3 Radial mode of a thin-walled spherical shell . . . . . . . . . . . . . . . 137

D.3.1 Analytical calculation . . . . . . . . . . . . . . . . . . . . . . . . 137

D.3.2 Computational solution . . . . . . . . . . . . . . . . . . . . . . . 138

D.4 Longitudinal vibration of a laterally constrained rod . . . . . . . . . . 140

D.4.1 Analytical approach . . . . . . . . . . . . . . . . . . . . . . . . . 140

D.4.2 Computational solution . . . . . . . . . . . . . . . . . . . . . . . 141

D.5 First radial mode of a solid sphere . . . . . . . . . . . . . . . . . . . . . 142

D.5.1 Analytical calculation for the radial mode . . . . . . . . . . . . 142

D.5.2 Computational solution . . . . . . . . . . . . . . . . . . . . . . . 144

**References 147**

# Nomenclature

| **Symbols** | **Definition** |
|---|---|
| $m$ | Index of the power-law damping formula |
| $\xi$ | Fitted material constant in the power-law damping formula |
| $\lambda$ | Fitted constant between 0 to 1 |
| $\widetilde{\mathbf{S}}$ | Stress “amplitude” matrix |
| $\mathbf{S}$ | Scaled stress “amplitude” matrix |
| $\sigma, \tau$ | Normal and shear stresses respectively |
| $\mu$ | Frictional coefficient between the crack faces |
| $\beta$ | Ratio of the mean to the amplitude of the normal stress |
| $\zeta$ | Ratio of the amplitudes of the shear stress to the normal stress |
| $D$ | Dissipated energy |
| $C$ | Friction-independent fitted constant |
| $\widehat{n}$ | Unit normal |
| $k_f$ | Scaling factor |
| $\mathbf{B}$ | Fitted $20 \times 5$ matrix in the empirical formula |
| $\omega$ | Natural frequency |
| $\zeta_{eff}$ | Effective damping ratio |
| $\overline{E}$ | Total energy of a system averaged over one cycle |
| $-\Delta\overline{E}$ | Energy dissipated per oscillation |

| **Symbols** | **Definition** |
|---|---|
| $\rho$ | Mass density of the vibrating body |
| $\boldsymbol{\phi}$ | Mass-normalized mode shape |
| $\boldsymbol{\epsilon}$ | Strain column matrix |
| $\mathbf{u}$ | Displacement column matrix |
| $\mathbf{N}$ | Column matrix of shape functions |
| $\mathbf{E_s}$, $\mathbf{C}$, $\mathbf{C}^*$ | $6 \times 6$ elastic stiffness matrix (Voigt form) for isotropic material |
| $E$ | Young's modulus |
| $\nu$ | Poisson's ratio |
| $\mathbf{J}$ | Jacobian matrix |
| $C_{ijkl}$ | Element of the elasticity stress tensor |
| $S_{ijkl}$ | Element of the Eshelby tensor |
| $\varepsilon_{ij}$ | Element of the strain tensor |
| $J_2, J_3$ | Second and third invariants of the deviatoric stress |
| $\sigma_{yp}$ | Yield strength of the material |
| $\sigma_d$ | $6 \times 1$ deviatoric stress matrix |
| $W_d$ | Plastic energy dissipation |

# List of Figures

1.1 (a) Finite element model of an arbitrarily chosen object. (b) Its first vibration mode. . . . . . . . . . . . . . . . . . . . . . . . . . . . . 2

1.2 Figures 4 to 6 of Mead and Mallik (1976) are reproduced here by manually extracting the harmonic excitation data (black circles) from those figures. The numbers 1, 2, and 3 here correspond to figures 4, 5, and 6 respectively in their paper. The fitted straight lines on these log-log plots show that $m$ is between 2 to 3 (2.56 for figure 4, 2.27 for figure 5, and 2.90 for figure 6). . . . . . . . . . . . . . . . . . . . . . . 5

2.1 An element with a small embedded frictional crack. . . . . . . . . . . 16

2.2 2D representation of the frictional microcrack. . . . . . . . . . . . . . 17

2.3 Applied normal and shear loads. Sign convention for mean normal stress: compression is positive. . . . . . . . . . . . . . . . . . . . . . . 18

2.4 Analytical formula with a fitted constant $C$ vs. energy dissipation in two dimensional finite element (FE) analysis. Subplot (a) shows all our 2D finite element results. A few points (solid dark circles) show a slight mismatch. These are from a separate sub-calculation for studying never-opening solutions under large compressive mean normal stresses. Subplot (b) shows those results for varying $\beta$ with $\mu = 0.5$, $\sigma_a = 60$ MPa and $\tau_a = 80$ MPa. The mismatch is negligible for our purposes. . . . . . . . . . . . . . . . . . . . . . . . . . . . 21

2.5 A schematic of the cracks at different planes are shown (each plane has four different cracks). Not all possible planes and cracks are shown here. . . . . . . . . . . . . . . . . . . . . . . . . . . . . . . . 22
2.6 50,000 uniformly distributed points on the unit hemisphere. The actual averaging was done with 4.5 million points and will be treated as accurate. . . . . . . . . . . . . . . . . . . . . . . . . . . . . 23
2.7 (a) Mohr's circles and dissipation possibilities (shown hatched). (b) Range of scaled $\sigma_1$ for nonzero dissipation. . . . . . . . . . . . . . . . . 24
2.8 (a) Computed average (Monte Carlo) dissipation with $C = 1$ for tension and pure shear. Here $\mu$ is viewed as a fitted parameter. The stress states remain unchanged for each of the two curves. (b) The ratio of the dissipation for the two stress states against $\mu$, which might in principle be used to estimate $\mu$ (see main text). . . . . . . . . . . 27
2.9 Comparison of Eq. (2.6) against our dissipation model for two $\mu$ values (different least squares fits used in each subplot, for $\lambda_1$ and $\lambda_2$). The plotted straight lines are at 45 degrees, for reference. These plots may be compared against Fig. 2.12 (b) below. . . . . . . . . . . . . . . . . 30
2.10 Dissipation surface plots for two $\mu$ values. . . . . . . . . . . . . . . . 31
2.11 Dissipation plot for other $\mu$ values. . . . . . . . . . . . . . . . . . . . 32
2.12 Dissipation comparison for $\mu = 0.4$ with $C = 1$: (a) superimposed dissipation plots, (b) error plot (Monte carlo − fitted formula). . . . . 34
2.13 Dissipation comparison for all $\mu$ values with $C = 1$ (a 45° line is also shown in this plot). . . . . . . . . . . . . . . . . . . . . . . . . . . 35
2.14 Numerical solution of Eq. (2.15) using Matlab's "ode15s." The initial condition was changed from $\dot{x}(0) = 0$ to $\dot{x}(0) = 10^{-10}$ to avoid the immediate discontinuity at zero. The amplitude envelope approximation of $e^{-ct/\pi}$ matches near-perfectly. . . . . . . . . . . . . . . . . . 37
2.15 10 noded tetrahedral element . . . . . . . . . . . . . . . . . . . . . . 38
2.16 Vibration modes of the solid body: (a) second mode, (b) third mode. The first mode was shown in Fig. 1.1 (b). . . . . . . . . . . . . . . . . 42

2.17 (a) Damping ratios for the first three modes. (b) The ratio of the effective damping ratio of the third mode to that of the first mode. . 43

3.1 One-dimensional dissipation model. . . . . . . . . . . . . . . . . . . . . 48

3.2 Dissipation in the one-dimensional model. (a) Shaded area shows the energy dissipated in one cycle of amplitude $A > \dfrac{f}{k_1}$. (b) Dissipation against amplitude $A$. . . . . . . . . . . . . . . . . . . . . . . . . . 49

3.3 Ellipsoidal elasto-plastic flaw embedded in an elastic material with far-field stresses $\sigma^0_{ij}$. The ellipsoid is given by $\dfrac{x^2}{a_1^2} + \dfrac{y^2}{a_2^2} + \dfrac{z^2}{a_3^2} \leq 1$. . . . 50

3.4 Finite element mesh of the 3D model (quarter portion). A small region around the ellipsoidal flaw ($a_1 = 1\,\text{mm}$, $a_2 = 0.75\,\text{mm}$, and $a_3 = 0.5\,\text{mm}$) is shown enlarged. . . . . . . . . . . . . . . . . . . . . 52

3.5 Plot of von Mises stress in one quarter of the model at a normalized load step of 0.3. The stress plot within the inclusion is uniform. The geometry of the ellipsoid is $a_1 = 1\,\text{mm}$, $a_2 = 0.75\,\text{mm}$, and $a_3 = 0.5\,\text{mm}$; and the far-field loads are of load case 1 of Table 3.2. . . 53

3.6 Plot of $\sigma_x$ in one quarter of the model at a normalized load step of 0.3. The variation of $\sigma_x$ within the inclusion is small. The geometry of the ellipsoid is $a_1 = 1\,\text{mm}$, $a_2 = 0.75\,\text{mm}$, and $a_3 = 0.5\,\text{mm}$; and the far-field loads are of load case 1 of Table 3.2. . . . . . . . . . . . 54

3.7 Plot of $\sigma_x$ at the normalized load step of 0.3 in the quarter portion of the model with a cylindrical flaw. The variation of $\sigma_x$ within the inclusion is seen non-uniform. The cylindrical flaw is of 0.5 mm radius and 1 mm length. The far-field load considered is load case 1 of Table 3.2. . . . . . . . . . . . . . . . . . . . . . . . . . . . . . . . . . . 55

3.8 Stress components inside ellipsoidal elasto-plastic flaw. Here, $a_1 = 1\,\text{mm}$, $a_2 = 0.75\,\text{mm}$, and $a_3 = 0.5\,\text{mm}$ and the far-field stresses are of load case 1 in Table 3.2. . . . . . . . . . . . . . . . . . . . . . . 56

3.9 Stress components inside an ellipsoidal elasto-plastic flaw where $a_1 = 1\,\text{mm}$, $a_2 = 0.75\,\text{mm}$, and $a_3 = 0.25\,\text{mm}$ and the far-field stresses are of load case 2 in Table 3.2. . . . . . . . . . . . . . . . . . . . . . . . 56

3.10 Inhomogeneous inclusion. The subdomain has different elastic moduli than the outer material and contains eigenstrain ($\varepsilon^*_{ij}$). The inclined shaded ellipse in the middle is intended to indicate that the inclusion cannot be fitted inside the cavity without causing additional strain in both the inclusion as well as the outer material. When the eigenstrain is zero the subdomain is called an *inhomogeneity*. When the subdomain has the same elastic moduli as the outer material it is called a *homogeneous inclusion* (or simply an *inclusion*). . . . . . . . . . . . . 57

3.11 Triangular wave form used for the far-field stresses in the cyclic loading case (three load cycles) . . . . . . . . . . . . . . . . . . . . . . . . 61

3.12 Variation of $\sigma^0_{xx}$ component in load case 1 of Table 3.2. . . . . . . . . 61

3.13 Results for cyclic loading. (a) Stress components inside the ellipsoidal region for ellipsoid of $a_1 = 1\,\text{mm}$, $a_2 = 0.75\,\text{mm}$, and $a_3 = 0.5\,\text{mm}$ under maximum far-field load of load case 1 of Table 3.2. The numbers correspond to: 1-$\sigma_x$, 2-$\sigma_z$, 3-$\sigma_y$, 4-$\tau_{xy}$, 5-$\tau_{yz}$ and 6-$\tau_{zx}$. (b) Comparison of the plastic dissipation in this loading case. . . . . . . . . . . . . . 63

3.14 Stress state in a spherical ($r = 1\,\text{mm}$) inclusion, for the three load cases of Table 3.2. . . . . . . . . . . . . . . . . . . . . . . . . . . . 64

3.15 Cyclic dissipation against $\sqrt{J_2}$ for three different load cases of Table 3.2 for a spherical inclusion ($r = 1\,\text{mm}$). . . . . . . . . . . . . . . . . 65

3.16 Cyclic dissipation against $\sqrt{J_2}$ for three different load cases of Table 3.2 for an ellipsoidal inclusion ($a_1 = 1\,\text{mm}$, $a_2 = 0.75\,\text{mm}$, and $a_3 = 0.25\,\text{mm}$). . . . . . . . . . . . . . . . . . . . . . . . . . . . . . 66

3.17 Stress state for a flat and thin ellipsoidal flaw ($a_1 = 1\,\text{mm}$, $a_2 = 0.75\,\text{mm}$, and $a_3 = 0.001\,\text{mm}$) in three load cases of Table 3.2. . . . . 67

3.18 Variation of cyclic dissipation with respect to (a) $\sqrt{J_2}$ and (b) the resolved shear stress ($\tau$ of Eq. (3.14)), for three different load cases of Table 3.2 for a flat and thin ellipsoidal flaw ($a_1 = 1\,\mathrm{mm}$, $a_2 = 0.75\,\mathrm{mm}$, and $a_3 = 0.001\,\mathrm{mm}$). . . . . . . . . . . . . . . . . . . . . . . . 69

4.1 The Weibull distribution plotted for some choices of parameter values. 72

4.2 A typical plane with unit normal $\widehat{n}$ on the surface of a unit sphere. . 75

4.3 Dissipation plots for four $m$ values, normalized in each case so that $D_{\mathrm{ff}} = 1$ at $\chi = 0.5$. . . . . . . . . . . . . . . . . . . . . . . . . . . . 78

4.4 Mohr's circle diagrams to show that $D_{\mathrm{ff}}$ is symmetric about $\chi = 0.5$. . 79

4.5 Comparison of $D_{\mathrm{ff}} \times J_2^{-m/2}$ against $J_2$ for $m = 3$ and 6. . . . . . . . . 81

4.6 Coefficient of variation of $\dfrac{D_{\mathrm{ff}}}{J_2^{m/2}}$. . . . . . . . . . . . . . . . . . . . . . 82

4.7 The leading-order approximations of Eq. (4.15) (i.e. for $\chi = 0$), and Eq. (4.16) with $\chi = 0.5$, against their corresponding correct values. In each case, $\sigma_1 - \sigma_3 = 1$ and only $m$ is varied. . . . . . . . . . . . . . . 83

5.1 Transverse vibration of a simply supported beam. . . . . . . . . . . . 87

5.2 (a) Finite element model of the simply supported beam. (b) Transverse vibration mode from the FE model. Note that the bending is in-plane and this is not the first mode of vibration. However, this is a mode where beam theory is more accurate. . . . . . . . . . . . . . . 89

5.3 SHELL181 stress output at three locations through the element thickness. . . . . . . . . . . . . . . . . . . . . . . . . . . . . . . . . . 92

5.4 Shell model of thin rectangular plate. . . . . . . . . . . . . . . . . . . 94

5.5 Shell model of thin-walled spherical shell. Half of the model is shown on the right. . . . . . . . . . . . . . . . . . . . . . . . . . . . . . . 94

5.6 Matlab based GUI for computing $\zeta_{\mathit{eff}}$ using ANSYS. . . . . . . . . . . 97

5.7 Rectangular plates meshed using solid elements. (a) Uncut plate with dimensions 1 m × 1 m × 0.0365 m (39856 elements). (b) Slotted plate with dimensions 1 m × 1 m × 0.04 m (53590 elements). Near the edges of this plate, 12 rectangular (0.1 m × 0.05 m) slots are cut to introduce stress concentrations. . . . . . . . . . . . . . . . . . . . . . . 98

5.8 First three vibration modes of the rectangular plates. . . . . . . . . . 99

A.1 Some waveforms: (a), (b), (c) are allowed, but (d) is not. The scale is arbitrary, for both stress and time. . . . . . . . . . . . . . . . . . . . 106

A.2 Finite element mesh of the 2D model. A small region is shown enlarged. The rectangles and the arrow were drawn in later, manually and approximately, for visualization. . . . . . . . . . . . . . . . . . . . 108

A.3 Mesh convergence for a particular load case (fifth row of table A.1) using 200 time steps in the loading cycle. . . . . . . . . . . . . . . . . 108

A.4 Effect of changing the number of time steps used. . . . . . . . . . . . 109

A.5 (a) A spring block system under periodic normal and tangential load. (b) Applied normal and shear loads. Note the sign convention: compressive mean normal stress is positive. . . . . . . . . . . . . . . . . . . 110

A.6 One half of the 3D finite element mesh with circular crack. . . . . . . 112

A.7 Convergence study for the circular crack. Mesh refinement, using 100 time steps in the loading cycle. The largest number of solid elements used was 59,410. The dissipation values are fitted fairly well (empirically) by a curve of the form $a_0 + \frac{a_1}{N^2} + \frac{a_2}{N^3}$, where $N$ is the number of elements. The limiting value, $a_0$, matches the last computed value to within about 1 percent, and so further refinement was not attempted. . . . . . . . . . . . . . . . . . . . . . . . . . . 113

A.8 Effect of changing the number of time steps used. Since convergence of the final dissipated amount was rapid, and the computation was slow, more than 100 steps within the cycle were not used. . . . . . . . 113

A.9 Analytical formula for dissipation against computed value from finite element (FE) simulation (with one fitted constant $C$) for the circular crack. The numbers are larger than for the 2D computations because the stresses used here are larger; note, however, that the material is linearly elastic and stress magnitudes are notional. . . . . . . . . . . . 114
A.10 One half of the 3D finite element mesh with a triangular crack. . . . . 117
A.11 Analytical formula for dissipation against computed value from finite element (FE) simulation (with one fitted constant $C$). The crack is an isoceles triangle. . . . . . . . . . . . . . . . . . . . . . . . . . . 117
A.12 Response of the damped oscillator in Eq. (A.6). . . . . . . . . . . . . 119

D.1 Pure torsional vibration of a circular rod. . . . . . . . . . . . . . . . . 131
D.2 FE model of the rounded rod. . . . . . . . . . . . . . . . . . . . . . . 133
D.3 Mode shape of the torsional mode. . . . . . . . . . . . . . . . . . . . 133
D.4 Thin rectangular plate. . . . . . . . . . . . . . . . . . . . . . . . . . 134
D.5 FE model of the rectangular plate. . . . . . . . . . . . . . . . . . . . 136
D.6 First vibration mode of the simply supported rectangular plate. . . . 136
D.7 Radial mode vibration of thin-walled spherical shell (half of the sphere is shown). . . . . . . . . . . . . . . . . . . . . . . . . . . . . . . . . 137
D.8 FE model of the thin sphere. . . . . . . . . . . . . . . . . . . . . . . 139
D.9 Uniform radial mode vibration of the sphere. . . . . . . . . . . . . . . 139
D.10 Laterally constrained rod. $u_y = 0$ on the top and bottom faces. $u_z = 0$ on the front and back faces. Displacements are unconstrained in the right most face. The left most face is fixed. . . . . . . . . . . 140
D.11 FE model of the laterally constrained rod. . . . . . . . . . . . . . . . 141
D.12 First mode of the laterally constrained rod. . . . . . . . . . . . . . . 142
D.13 Radial mode vibration of solid sphere (half of the sphere is shown). . 142
D.14 Free body diagram of the element. . . . . . . . . . . . . . . . . . . . 143
D.15 FE model of the solid sphere. . . . . . . . . . . . . . . . . . . . . . . 145
D.16 Radial mode of the solid sphere. . . . . . . . . . . . . . . . . . . . . 145

D.17 Twisting mode of the solid sphere. . . . . . . . . . . . . . . . . . . . . . 146

# List of Tables

2.1 Dissipation results for five typical cases in the two-dimensional finite element analysis (see Appendix A.2 for more simulation results with several other arbitrarily chosen $\mu$ and stress amplitude values). . . . . 19

2.2 Volumetric coordinates and their nodal values for the SOLID187 element (see ANSYS manual, 2009). . . . . . . . . . . . . . . . . . . . . . 39

2.3 Gauss points and weights for four point Gauss quadrature scheme (see ANSYS manual, 2005). . . . . . . . . . . . . . . . . . . . . . . . 40

3.1 Material properties (chosen arbitrarily) used in all the analyses in this chapter. . . . . . . . . . . . . . . . . . . . . . . . . . . . . . . 51

3.2 Different far-field stresses (MPa) considered in various examples within this chapter. . . . . . . . . . . . . . . . . . . . . . . . . . . . . . 52

4.1 $D_{\text{ff}}$ from Eq. (4.10) with $\bar{\xi} = 1$, for the arbitrarily chosen stress state of $\sigma_1 = 1.26$, $\sigma_2 = 0.87$ and $\sigma_3 = -0.34$. The numerical integration is accurate to several significant digits. . . . . . . . . . . . . . . . . . 77

5.1 Material properties considered in the finite element model. . . . . . . 88

5.2 Values of $\zeta_{\mathit{eff}}$ for six solid models considered. . . . . . . . . . . . . . . 90

5.3 Results for two shell models considered for validation of $\zeta_{\mathit{eff}}$ computations using SHELL181 elements. The results obtained previously using solid elements are also given here. . . . . . . . . . . . . . . . . . 93

5.4 Computed $\zeta_{eff}$ results for both the plates. The uncut plate is denoted as "Plate 1" and the slotted plate is denoted as "Plate 2". For comparison purposes, the $\zeta_{eff}$ values are normalized with respect to the first vibration mode of the uncut plate (Plate 1) for each $m$. . . . . . 100

A.1 Dissipation results for various cases in the two-dimensional finite element analysis. The first 4 rows show that the mean value of the shear stress does not affect the dissipation per cycle. . . . . . . . . . . . . . 107
A.2 Dissipation results for various load cases: flat circular crack. The first 2 rows show that the mean value of the shear stress does not affect the dissipation per cycle. . . . . . . . . . . . . . . . . . . . . . . . . . 115
A.3 Dissipation results for various load cases: flat triangular crack. The first 4 rows show that the mean value of the shear stress does not affect the dissipation per cycle. . . . . . . . . . . . . . . . . . . . . . . 116

D.1 First eight vibration modes of the circular rod and their corresponding normalized $\zeta_{eff}$ values. . . . . . . . . . . . . . . . . . . . . . . . . . . 134
D.2 $\zeta_{eff}$ in the transverse vibration of the rectangular plate. . . . . . . . . 137
D.3 $\zeta_{eff}$ for thin spherical shell. . . . . . . . . . . . . . . . . . . . . . . . . 139
D.4 $\zeta_{eff}$ for solid sphere. . . . . . . . . . . . . . . . . . . . . . . . . . . . 146

# Chapter 1

# Introduction

This thesis is motivated by an engineering design problem. Consider two possible designs (shapes and dimensions) for some engineering component, to be made of some known, lightly dissipative material. Which design has better vibration damping?

The above problem can be relevant to many engineering design situations. Design of automotive components for reduction of the vibration levels is an easy example. Another example would be to control the vibration levels in spacecraft components to improve the accuracy of optical and guidance systems. Improvement of damping behavior of aircraft and space structures equipments still remains an important topic. Therefore, the above question has its own importance.

One can think of using modern computational facilities to address this question. A computational approach would begin with straightforward finite element based modal analysis. However, the commercial finite element packages give only frequencies and mode shapes. Computation of damping values is not routine in such packages. Computation of damping requires a constitutive relation for material damping under time-periodic triaxial inhomogeneous stresses. As discussed below, such a relation is not presently available.

To fix ideas, let us consider the solid object of Fig. 1.1 (a), modeled using a finite element package, with its first mode as shown in Fig. 1.1 (b) (details of this model will be discussed in section 2.5.4). We want to compute the damping ratios for the first several modes of such an object. To do that, we require a multiaxial damping formula that can be used along with the modal analysis results. Such a multiaxial damping relation is not presently available in the literature.

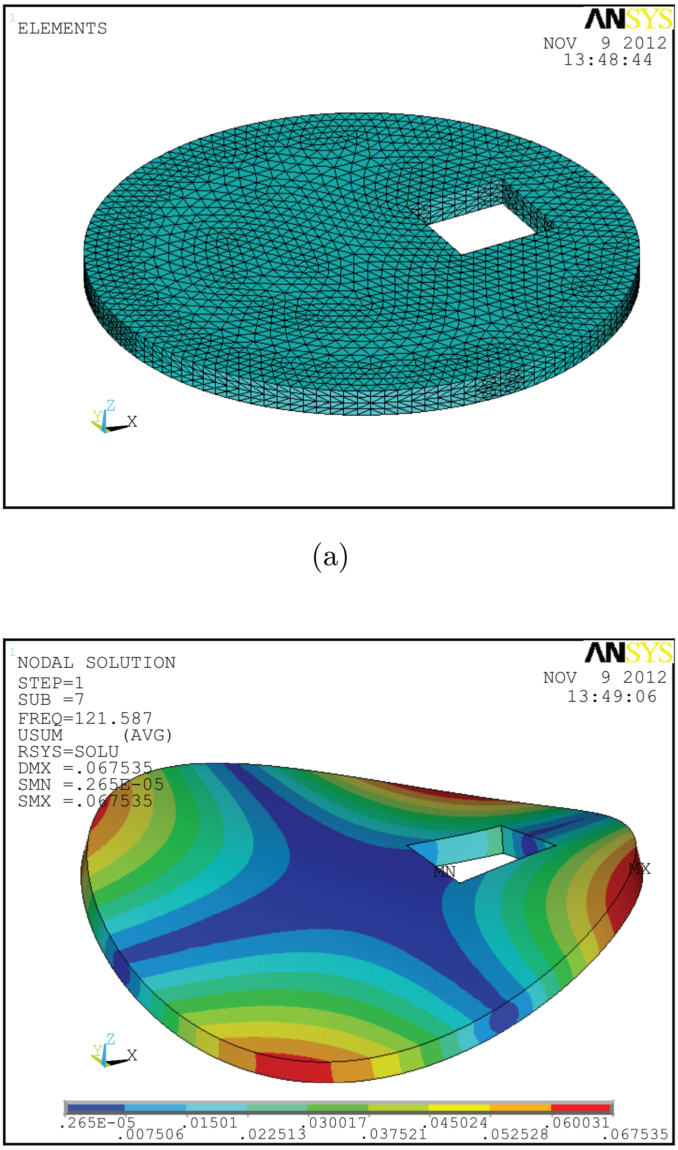
ELEMENTS
ANSYS
NOV 9 2012
13:48:44
Y
Z
X
NODAL SOLUTION
STEP=1
SUB =7
FREQ=121.587
USUM (AVG)
RSYS=SOLU
DMX =.067535
SMN =.265E-05
SMX =.067535
ANSYS
NOV 9 2012
13:49:06
MN
MX
Y
Z
X
.265E-05
.007506
.01501
.022513
.030017
.037521
.045024
.052528
.060031
.067535

(a)

(b)

Figure 1.1: (a) Finite element model of an arbitrarily chosen object. (b) Its first vibration mode.

In this context, in this thesis we have developed, for the first time in the literature, multiaxial macroscopic damping models based on assumed underlying micromechanical models of internal dissipation. In addition, we have demonstrated how these macroscopic models can be used to compute modal damping of any arbitrary solid object within a finite element environment. Therefore, this thesis adds to the existing knowledge of material damping within the framework of multiaxial dissipation in structural components.

Having discussed briefly the goal and the contributions of this thesis, we now give a detail discussion of the topic and the relevant literature below.

## 1.1 Material damping and relevant prior work

Solid bodies undergoing cyclic deformation lose energy. Some energy is lost to the surrounding atmosphere; some goes into supports, joints, and such other dissipative elements; and the rest is dissipated inside the material. This thesis considers the latter means of dissipation, known as material damping or internal friction.

In our study of material damping, we have considered solids undergoing harmonic stress cycles and the energy dissipated therein. It has been empirically observed that, in many solids, the energy dissipated per unit volume and per cycle of deformation is proportional to the stress amplitude raised to some power $m \geq 2$, and largely independent of frequency in the low frequency range (say, on the order of 100 Hz or less). This can be written as

$$D = \xi \sigma_{eq}^{m} \tag{1.1}$$

where $D$ stands for specific material damping, $\sigma_{eq}$ represents a suitable stress amplitude, and $\xi$ is a material constant. For comparison, we note that the commonly assumed linear viscous damping (such as a $c\dot{x}$ term representing damping in a harmonic oscillator) leads to per-cycle dissipation proportional to frequency; while a macroscopic rate-independent dry friction element gives dissipation with $m = 1$. Thus, Eq. (1.1) is not as intuitively obvious as it might initially seem.

There is a huge literature on damping. We have considered works only directly relevant to Eq. (1.1).

Frequency independence in material damping was first observed by Lord Kelvin (1865). Rowett (1914) reported careful static and dynamic experiments in torsion of thin walled tubes and observed frequency independent behavior. He also reported power law damping with $m = 3$ for the tubes as supplied, and found increased values of damping for annealed tubes. For the annealed tubes, his numerical data suggests $2 < m < 3$.

Broader experiments with several different materials involving horizontally supported spinning rods with vertical end loads, were reported by Kimball and Lovell (1927). Internal dissipation caused lateral deflection of the rod. Both frequency independence as well as a rough power law were observed ($m \approx 2$). The authors cited some other data that suggests $m > 2$.

Mead and Mallik (1976) suggested quite reasonably that replacing stress with strain in Eq. (1.1) leads to better units for $\xi$. Although they used an empirical dissipation model with a sum of two power-law terms, their actual experimental results for harmonic torsional oscillations would pass as straight lines on log-log plots, with $2 < m < 3$ (see their figures 4 through 6, reproduced below in Fig. 1.2 by manually extracting the data from their figures). Interestingly their results show that $m$ can have non-integer values.

In a more recent experimental work, Maslov and Kinra (2005) have reported frequency independence (within their experimental scatter) in carbon foams over a large frequency range. Though nonlinear damping behavior was observed for large amplitudes, a power law was not fitted and appears inappropriate. Their data adds one more solid material with frequency independent damping to the remarkable list begun by Kimball and Lovell (1927).

When we come to modeling dissipation, we first mention Lazan's well known book in 1968 (Lazan, 1968). He took a phenomenological approach, noted power-law behavior for intermediate stress ranges for several materials (including fractional powers), and also discussed a variety of simple models. These models included elements with friction and plasticity, but not the statistical distribution of strengths that we assume here in order to theoretically obtain the power law behavior with $m \geq 2$.

From a more theoretical background, Granato and Lücke (1956) proposed an explanation of material damping based on dislocation pinning by impurity particles. Dawson (1978) considered an unknown function of nondimensionalized stress, for-

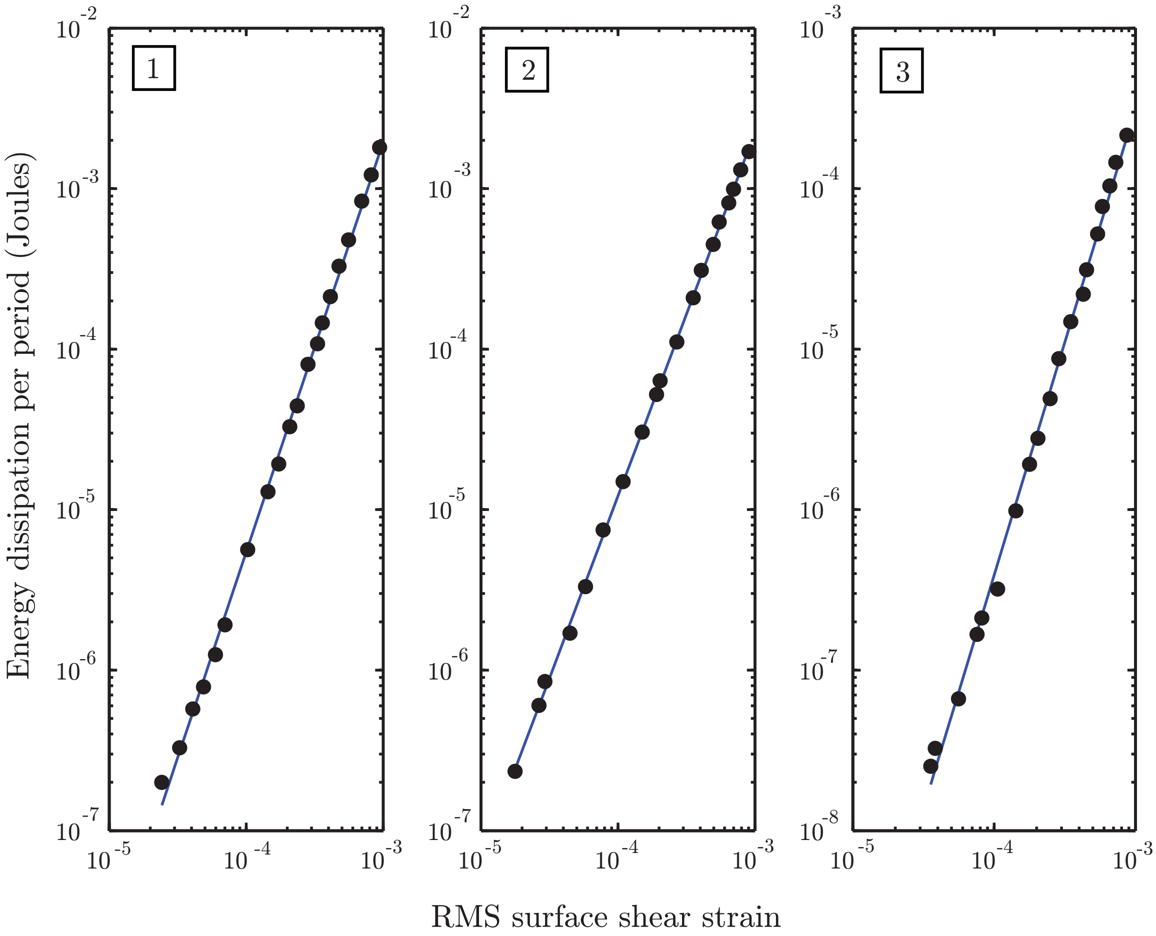

Figure 1.2: Figures 4 to 6 of Mead and Mallik (1976) are reproduced here by manually extracting the harmonic excitation data (black circles) from those figures. The numbers 1, 2, and 3 here correspond to figures 4, 5, and 6 respectively in their paper. The fitted straight lines on these log-log plots show that $m$ is between 2 to 3 (2.56 for figure 4, 2.27 for figure 5, and 2.90 for figure 6).

mally expanded in a Taylor series using even powers only, leading by assumption to $n = 2$ for small stresses.

In addition to the above empirical and theoretical papers and approaches, there are some *procedural* papers that develop *ad hoc* one-dimensional nonlinear differential equation formulations that model frequency independent dissipation. These approaches could be useful in time domain simulations of damped systems. We mention Muravskii (2004) and Spitas (2009) as examples. In the context of such papers, we note that while $m = 2$ in the power law whenever the damping is linear, the converse is not true: nonlinear damping relations can give $m = 2$ as well.

We note an important point here that the literature we discussed above only considers dissipation in uniaxial cases. However, we are interested in dissipation in multiaxial stress states. No convincing mechanically-based engineering model for the same is presently available. For example, the stress state in Kimball and Lovell's experiment (Kimball and Lovell, 1927) was predominantly uniaxial. The empirical laws in Lazan (1968) also do not identify the equivalent stress of Eq. (1.1) under arbitrary triaxial load. Dislocation-based models as in Granato and Lücke (1956) involve several parameters related to the crystal structure, yet to be translated into measurable external macroscopic model parameters. The approach of Dawson (1978) also does not identify the role of multiaxial stresses in the dissipation model. As a final example, Hooker (1969) proposed that the equivalent stress amplitude should be computed as

$$\begin{aligned} \sigma_{eq}^2 &= (1-\lambda)(I_1^2 - 3I_2) + \lambda I_1^2 \\ &= (1-\lambda)\sigma_d^2 + \lambda\sigma_v^2, \quad \text{with } 0 < \lambda < 1, \end{aligned} \tag{1.2}$$

where $I_1$ and $I_2$ are the first and second stress invariants respectively, $\sigma_d^2$ and $\sigma_v^2$ are proportional to the distortional and dilatational strain energies respectively, and $\lambda$ is a fitted parameter. The above is motivated by the fact that it is a linear combination of distortional and dilatational strain energies[1]. Similar combinations and interpolations were considered, with varying degrees of experimental support, by several other authors, including Robertson and Yorgiadis (1946), Whittier (1962), Torvik *et al.* (1963), and Mentel and Chi (1964). These attempts to incorporate multiaxial stresses are given below.

Robertson and Yorgiadis (1946) studied several materials (metallic and nonmetallic), and found that dissipation per cycle was frequency independent and proportional to the *cube* of a suitable stress amplitude (unlike Kimball and Lovell (1927) but matching Rowett (1914)). More interestingly, Robertson and Yorgiadis (1946) sought an equivalence between damping in extension and torsion of tubes, and found that in order for the dissipation under the two kinds of loads to be identical, the shear stress in the torsion experiment needed to be $k$ times the longitudinal stress in the extension-compression experiment, with $k$ ranging from 0.48 to 0.60. It is notable that if damping was a function of distortional strain energy alone, then $k$ would be 0.577.

---

[1] It is tempting to conclude that such a split is intuitively obvious but we will show reasonable micromechanics that predicts otherwise.

Whittier (1962) presented a study of vibration amplitude decay rates of circular steel plates and rectangular steel beams in vacuum. The experiments were well conceived and executed with the objects supported on nodal circles and nodes respectively, and displacements measured using noncontacting capacitive probes. In our opinion, the attention to possible sources of error and demonstration of their smallness, just in themselves, make this excellent paper well worth reading. It was found that for somewhat larger stresses dissipation varies as the cube of stress amplitude, and that both distortional and dilatational strain energy contribute to the observed macroscopic damping.

Torvik *et al.* (1963) discussed biaxial test results for several materials. The tests, done at the University of Minnesota, involved axial and torsional loading of tubes through crank arrangements. Load and deformation measurements were through strain gages. Dissipation was measured by the area of the hysteresis loop for a range of principal stress ratios, and was therefore limited to somewhat larger dissipation ranges. The empirical theory proposed was based on dissipation through small plastic deformation, and biaxial damping models proposed were motivated in their mathematical form by various failure theories for engineering materials, with variable degrees of success. Different qualitative behaviors were obtained for different materials, the theories used were not developed from underlying micromechanics, and the results cannot be easily compared with ours.

Subsequent related experiments were performed by Mentel and Chi (1964), also in Minnesota. Damping was measured in thin-walled cylindrical specimens (made of manganese-copper alloy) subjected to combined internal pressure and axial loading. Crank assemblies were used for the load application. In this experiment, the biaxial stress ratio ($-1 \leq \sigma_2/\sigma_1 \leq 1$) covered a larger range than in Torvik *et al.* (1963). Dissipation was measured by measuring areas of hysteresis loops. The results showed a small contribution of dilatational strain in the dissipation.

Several *ad hoc* damping models proposed by these *biaxial* experimental measurements were later combined by Hooker (1969) to prescribe a formula (given in Eq. (1.2)) based on a weighted sum of the two strain energies (distortional and dilatational). No physical basis was presented for this model. Experimental investigations in this area were again reported, more recently, by Hooker and co-authors (see Hooker (1981), Hooker and Mead (1981) and Hooker and Foster (1995)). These studies were mostly targeted towards devising experimental setups for careful damping measurements in biaxial settings, and not geared towards formulating constitutive models for general triaxial stress states. Their experimental improvements mostly lie in lowering extraneous losses, achieving more uniform stress distributions for a full range of stress ratios, application of mean loading, simplicity in operation, etc.

In summary, we can say that there have been several prior studies of dissipation under biaxial stress states, especially for materials whose internal dissipation is relatively high or at stress levels where the dissipation is high. Theoretical development of models such as we are going to present in this thesis has been missing, as has any experimental verification of any model under triaxial stress states. Data for materials with low dissipation, in addition, suffers from large scatter as expected.

## 1.2 Contributions of the thesis

We conclude from the above discussions that it is worthwhile, both academically as well as towards possibly designing special damping materials, to develop physically based multiaxial damping models that lead to Eq. (1.1) with $m \geq 2$. In this thesis, we have developed multiaxial damping model that rationalizes, physically and mathematically, the material damping behavior of Eq. (1.1). Then those dissipation models are used in finite element prediction of modal damping ratios in arbitrary solid objects.

Our damping models may be summarized as follows. We assume that the dissipation within the vibrating object is due to a multitude of random distribution of microscopic, rate-independent, dissipation sites or flaws. We consider two mathematically simple micromechanical dissipative phenomena that can be modeled as rate-independent: (i) Coulomb friction, and (ii) ambient-temperature plasticity. In the first, we consider a flat crack in an elastic material, with Coulomb friction between the crack faces. In the second, we consider dissipation due to microscopic elasto-plastic flaws.

For the first model with frictional microcracks, we begin with a single-crack embedded within a linearly elastic solid under far-field time-periodic tractions. The material is assumed to contain many such non-interacting microcracks. Single-crack simulations, in two and three dimensions, are conducted using ABAQUS. The net cyclic single-crack dissipation under arbitrary triaxial stresses is found to match, up to one fitted constant, a formula based on a pseudostatic spring-block model. We use that formula to average the energy dissipation from many randomly oriented microcracks using Monte Carlo averaging for arbitrary triaxial stress. We develop a multivariate fitted formula using the Monte Carlo results. The fitted formula is used in finite element simulation of solid objects for the computation of the net cyclic energy dissipation via elementwise integration. The net dissipation is then used to compute equivalent modal damping ratios. We note that this model in the absence of pre-stress always gives $m = 2$ in Eq. (1.1).

In the second approach, we consider dissipation due to distributed microscopic elasto-plastic flaws. For analytical tractability, we choose ellipsoidal elastic perfectly-plastic flaws or inclusions which is embedded inside an elastic matrix. We use finite element simulation in ABAQUS to obtain the state of stress within the ellipsoidal inclusion under far-field cyclic loads. We also develop a semi-analytical method with the help of Eshelby's (Eshelby, 1957) formula for inclusion problems. Computed results using this semi-analytical approach are found to match, with excellent accuracy, the finite element simulation results. We identify two limiting special cases from these simulations and consider them for our analytical development of macroscopic dissipation formulas. In the first limiting case, plastic flaws or inclusions are assumed to be of spherical shape where the single flaw dissipation is governed by $J_2$, the second deviatoric stress invariant, which is proportional to the distortional strain energy. In the second limiting case, we consider flaws that are near-flat and thin wherein the dissipation is governed by the far-field resolved shear stress applied on the plane parallel to the near-flat surface of the flaw. In both these cases, we assume a random distribution of flaw strengths and orientations, and obtain the net macroscopic dissipation analytically. We show that in these dissipation models arbitrary $m > 2$ can be incorporated. We also find from the first case that the net dissipation is exactly described by a power of the distortional strain energy. However from the second limiting case, we show that, when $m$ is between 2 and 6, the net dissipation is accurately described by a power of the distortional strain energy (and exactly so, for $m = 2$ and 4). For large $m$, separate asymptotic formulas are found for this second case, showing that the dissipation deviates from a function of distortional strain energy alone.

We finally suggest that for engineering modeling purposes of metallic structures, for moderate $m$, a simple power law based on the distortional strain energy might be reasonable. We then demonstrate use of this dissipation model to compute the modal damping ratios of arbitrary solid objects using commercial finite element package ANSYS.

We first use $m = 2$ in the distortional strain energy formula for the computation of effective damping ratio ($\zeta_{\mathit{eff}}$). The effective damping ratio is a measure of equivalent viscous damping in any lightly damped structure. We first use solid element (SOLID187) in ANSYS for our $\zeta_{\mathit{eff}}$ computation. Our finite element calculation of effective damping uses modal analysis results from ANSYS complemented by our own volume integrals for the dissipation. The results are then verified with known analytical results for the cases of several analytically tractable geometries. An interesting aspect of these damping results is that the $\zeta_{\mathit{eff}}$ shows a variation of over one order of magnitude over the cases we have considered even when the power ($m$) is 2. The torsion dominated mode has the greatest damping and for the radial mode of the solid sphere the damping ratio is the least of all.

Subsequently, noting that many engineering components can have thin-walled geometries, we extend our $\zeta_{eff}$ computation using shell elements (SHELL181) in ANSYS. The net cyclic dissipation in this case is also calculated from modal analysis followed by our own appropriate volume integrals. The results are verified with known analytical results.

Finally, we consider arbitrary $m \geq 2$. The $\zeta_{eff}$ results in these cases are normalized with respect to the average volumetric strain energy density for clean (size-independent) comparison. Effective damping results for various $m$ values are reported for a pair of objects of less analytically tractable shape.

In the course of this work, we have also developed an automated Matlab based graphical user interface (GUI) for fast and reliable computations of the effective damping ratios using Matlab's graphical user interface development environment (GUIDE). Development of this GUI makes use of the advantage of ANSYS's APDL (ANSYS Parametric Design Language) and its easy interface with Matlab. Some details of this practical contribution are provided.

Therefore, the main contributions of this thesis may be viewed as following.

1. We develop, for the first time, multiaxial damping formulas based on micromechanically motivated rate-independent dissipative phenomena as opposed to *ad hoc* proposals like Eq. (1.2).

2. We show that Eq. (1.1) can result from dispersed microscopic dissipation sites in an appropriate statistical framework; and therefore, Eq. (1.1) is less arbitrary than it might initially seem.

3. We develop two multiaxial damping models considering two mathematically simple rate-independent dissipation phenomena. The first model considers dissipation due to frictional microcracks whereas the second model involves dissipation in elasto-plastic flaws.

4. Based on a theoretical study of materials with small elasto-plastic flaws we sug-

gest that for engineering modeling purposes of metallic components, a simple power law formula based on the distortional strain energy might be reasonable when the index ($m$) of the power law is between 2 to 6.

5. We finally demonstrate how these multiaxial damping formulas can be used for finite element computation of modal damping ratios of arbitrary solid objects using both solid and shell element in ANSYS.

## 1.3 Outline of the thesis

We give an outline of the rest of the thesis here. As discussed earlier, in this thesis, we initially develop multiaxial damping models based on physically based rate-independent damping mechanisms. And then, we have demonstrated how these models can be used in a finite element environment to compute modal damping of any arbitrarily shaped solid body.

In **Chapter 2**, the entire development of the dissipation model based on the frictional microcracks is discussed. Use of such formula in finite element computation of modal damping of an arbitrarily shaped solid object using solid elements in ANSYS is also presented for completeness. In **Chapter 3**, dissipation within a single elasto-plastic flaws has been discussed using both finite element simulations and a semi-analytical approach. **Chapter 4** discusses the development of the other multiaxial dissipation formula considering the dissipation due to a multitude of elasto-plastic inclusions. In **Chapter 5**, we adopt a distortional energy based damping formula and discuss in details the finite element computation of the effective damping ratios. We discuss both solid and shell element formulation for this dissipation model and verify our computation with known analytical results. In **Chapter 6**, the summary and the major conclusions of the present thesis have been presented.

# Chapter 2

# Modal damping via dissipation from frictional microcracks

The work presented in this chapter has been published in Jana and Chatterjee (2013).

## 2.1 Introduction

As discussed in Chapter 1, Hooker (1969) combined several prior dissipation models based on biaxial damping measurements and proposed that the damping in multiaxial stresses should be computed as

$$D = \xi \sigma_{eq}^{m}, \tag{2.1}$$

where

$$\sigma_{eq}^{2} = (1-\lambda)(I_1^2 - 3I_2) + \lambda I_1^2. \tag{2.2}$$

Here, $D$ is specific material damping, $\sigma_{eq}$ is a suitable stress amplitude, and $\xi$ and $m$ are fitted constants, $I_1$ and $I_2$ are the first and second stress invariants respectively, and $\lambda$ is a fitted parameter between 0 to 1. In Eq. (2.2) the net dissipation is assumed to be a linear combination of distorsional and dilatational strain energies. However, no physical explanations for this split has been presented for this model.

In contrast to the above, there is in fact a micromechanical modeling approach that seems promising for our purposes. This approach considers randomly distributed frictional microcracks within an elastic material, as opposed to the *ad hoc* prescription of Eq. (2.2).

The literature on frictional microcracks in elastic materials is rich. Kachanov (1987) proposed an approximate analysis method based on a superposition principle for interactions of multiple cracks at moderate distances from each other. Aleshin and Abeele (2007) presented a tensorial stress-strain hysteresis model due to friction in unconforming grain contacts. Their model pays close attention to the variation of actual area of contact under normal stress, but has many parameters (seven for uniaxial compression alone). Deshpande and Evans (2008) studied frictional microcracks in the context of inelastic deformation and fracture of ceramics. Al-Rub and Palazotto (2010) computed energy dissipation in ceramic coatings and found that frictional dissipation in microcracks contributes significantly to overall dissipation. More recently, Barber and co-authors have presented several papers on mechanics with frictional microcracks. Jang and Barber (2011a) discussed the dissipation in interacting microcracks using Kachanov's (1987) approach. Barber *et al.* (2011) studied a single frictional elastic contact subjected to periodic loading. The contact has an extended area, part of which sticks while the remainder can slip; some basic results about energy dissipation under periodic loading are obtained. Jang and Barber (2011b) examined the substantial effect of the relative phase of harmonically varying tangential and normal loads on the dissipation in an uncoupled frictional system. Barber (2011) discussed discrete frictional systems under oscillating loads, and examined conditions under which the steady state solution retains a memory of the initial state. Individual cracks with surface roughness models for the contacting faces have been studied by Putignano *et al.* (2011), who observed that, with microslip in variable regions but no gross slip at the contact surfaces, energy dissipation varies as the cube of the stress amplitude for small amplitudes.

None of the above studies have considered the net dissipation in a body, with spatially variable stresses, from a multitude of randomly oriented frictional microcracks. Here, we seek a macroscopic constitutive relation for such dissipation.

To this end, for simplicity, we assume that the cracks are small and far apart (non-interacting); that initial super-small microslips on crack surface asperities can be neglected, and the crack faces modeled as non-adhering yet geometrically flat; that all crack face frictions can be modeled using a single Coulomb friction coefficient $\mu$; and that the material remains linearly elastic. We assume the normal and tangential loadings at each crack are in phase (as would occur for vibration of a body in a single mode). Although our initial formulation allows both nonzero mean stresses and nonuniform distributions of crack face orientations, our final formula assumes zero mean stress and uniformly distributed crack face orientations.

Under these assumptions, we develop an empirical formula with two fitted parameters for the dissipation per unit volume and per cycle of time-periodic triaxial stress, and use the solid object of Fig. 1.1 (a) shown in Chapter 1 in a computational example.

The contribution of this chapter may thus be viewed as the first assembly of the following tasks in one self-contained sequence: we use existing ideas about bodies with frictional microcracks, integrate their dissipation rate over all possible crack orientations, develop a constitutive model for the net specific dissipation per cycle, and demonstrate the use of the formula to compute the modal damping ratios of arbitrarily shaped objects.

## 2.2 Frictional dissipation in a single microcrack

The first step in our task is to compute the frictional dissipation in a single microcrack due to remote cyclic loading. For the two dimensional case, an analytical treatment is given in Jang and Barber (2011a), including an analytical formula based on a single degree of freedom spring-block model for when the entire crack face sticks or slips as one. We have studied the same using finite element calculations in both two and three dimensions. The formula based on the spring-block model, with one fitted constant, turns out to be highly accurate. These computations are outlined below (for details, see Appendix A).

See Fig. 2.1, where the crack is circular, planar and parallel to the horizontal faces of a cube shaped element. We have found in separate two dimensional computations that removing tiny regions around the crack tips does not influence the net dissipation, and so material or geometric nonlinearities are neglected[1].

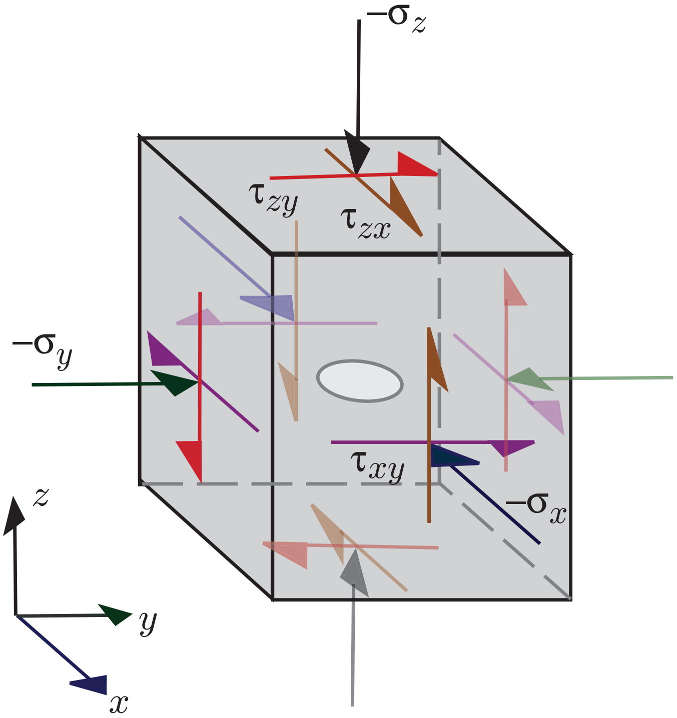

Figure 2.1: An element with a small embedded frictional crack.

We can simplify the three-dimensional picture. To any given state of stress and deformation, an additional $\sigma_x$ causes an additional uniform strain in the element but no added shearing at the crack face. Consequently, $\sigma_x$ causes no slip and does not contribute to the energy dissipated. Similar arguments apply for $\sigma_y$ and $\tau_{xy}$. Thus $\sigma_x$, $\sigma_y$ and $\tau_{xy}$ do not affect our results and are dropped. In contrast, $\sigma_z$ will affect the frictional forces, while $\tau_{zx}$ and $\tau_{zy}$ will cause frictional sliding. Finally, by rotating the coordinate system about the $z$-axis, $\tau_{zx}$ can be made zero. This leaves just the normal stress $\sigma_z = \sigma$ and the shear component $\tau_{zy} = \tau$ contributing to frictional dissipation. A two-dimensional representation is shown in Fig. 2.2.

Figure 2.3 depicts possible periodic normal and shear tractions, acting in phase,

---

[1] Specifically, we have done two simulations, one with the crack intact and another after removing a small circular region near the crack tip, and both resulted in same dissipation. So, it seems that the constitutive behavior of a small region near the crack tip does not affect the dissipation. And since that is where the material and geometric nonlinearities are large, they can be neglected.

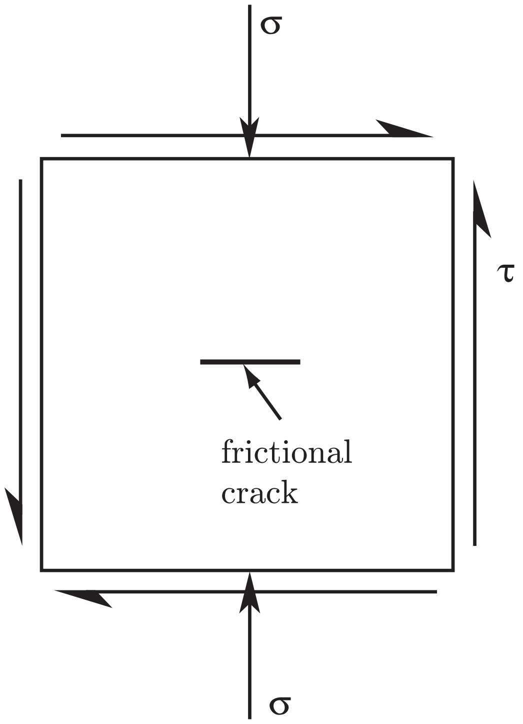

Figure 2.2: 2D representation of the frictional microcrack.

on the element of interest. Inertia is negligible (alternatively, frequencies are low), so the dissipation is frequency-independent. Our pseudostatic simulation results will actually apply to every periodic waveform where (i) the *changes* in far-field normal and shear stresses maintain a fixed proportion throughout the load cycle (i.e., the time-varying parts have similar waveforms), and (ii) there are only two points of stress reversal per cycle. See Appendix A.1 for some possible waveforms. For convenience, we used a triangular loading pattern in our computations described below. In the presence of multi-harmonic loading where there is more than two stress reversals per cycle, formulas presented in this thesis don't hold and the hysteritic nature of the macroscopic response would probably have to be explicitly incorporated. The simpler case of only two stress reversals per cycle is relevant to the case of a structure vibrating in one of its normal mode and therefore relevant to computing modal damping.

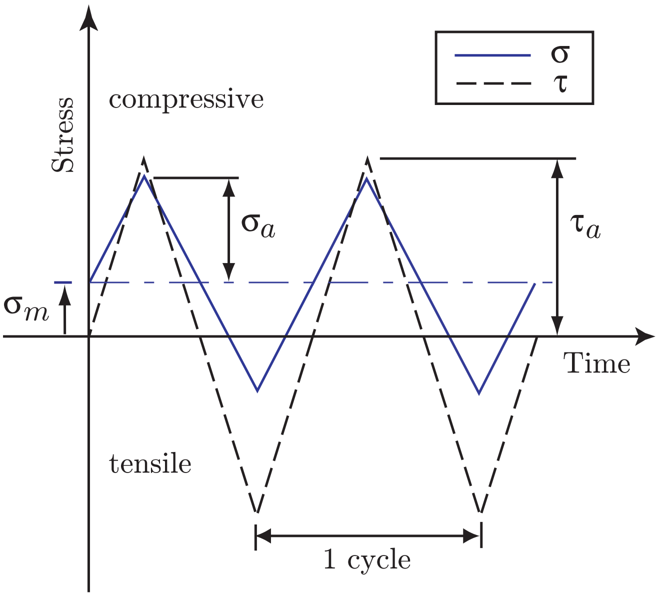

Figure 2.3: Applied normal and shear loads. Sign convention for mean normal stress: compression is positive.

### 2.2.1 Finite element simulations

Although we are interested in small flat cracks in three dimensions, we began with detailed two-dimensional (plane stress[2]) simulations in ABAQUS. Subsequently, we carried out three dimensional calculations with both a circular crack as well as a symmetrically loaded isosceles triangular crack. Details are presented in Appendix A. In particular, convergence was verified for both mesh size in space and load steps in time. Several load cases were run in each case with different values of stress amplitudes as well as the friction coefficient $\mu$. Results for five cases in the two dimensional simulation are given in Table 2.1 (many more such numerical results, for both two and three dimensional cases, are listed in Appendix A.2).

We acknowledge that ABAQUS gave us *one* solution in each case, without proving uniqueness. Jang and Barber (2011b) have discussed uniqueness in a more complicated, but two-dimensional, setting. Our three dimensional computations using ABAQUS had the specific goal of developing a physically defensible constitutive

---

[2] Plane stress versus plane strain are equivalent if we are willing to redefine the elastic constants (see Timoshenko and Goodier (1951)), and numerical values we use for these constants are notional in our case anyway.

| $\mu$ | $\tau_a$ (MPa) | $\sigma_a$(MPa) | $\beta = \left(\dfrac{\sigma_m}{\sigma_a}\right)$ | $\alpha = \left(\dfrac{\tau_m}{\tau_a}\right)$ | Dissipation (N-mm) |
|---|---|---|---|---|---|
| 0.3 | 70 | 30 | 0.4 | 0 | 0.0142 |
| 0.3 | 70 | 30 | 0.4 | 1.2 | 0.0142 |
| 0.4 | 100 | 50 | 0.6 | 0 | 0.0512 |
| 0.4 | 120 | 70 | $-0.4$ | 0 | 0.0112 |
| 0.5 | 80 | 60 | 2.57 | 0 | 0.0113 |

Table 2.1: Dissipation results for five typical cases in the two-dimensional finite element analysis (see Appendix A.2 for more simulation results with several other arbitrarily chosen $\mu$ and stress amplitude values).

relation for damping. We neither sought nor noticed evidence of dynamic waves near the sliding crack face[3].

### 2.2.2 Dissipation formula using a spring-block system

We now present an analytical formula that captures every result of the kind exemplified in Table 2.1. The formula is not new: it is given, in a different form, in Jang and Barber (2011a). However, we include it below because it plays a key role in this chapter. For details, see Appendix A.3.

We consider a spring and massless block system. The block slides on a frictional surface (coefficient $\mu$), and is attached to a rigid wall through the spring. Periodic normal ($\sigma$) and tangential loads ($\tau$) act on the block. When $\sigma < 0$, there is no friction. To the extent that the entire crack face slips or sticks as one, this single degree of freedom model should be accurate: we will find below that it is.

Define

$$\zeta = \frac{\tau_a}{\sigma_a} \quad \text{and} \quad \beta = \frac{\sigma_m}{\sigma_a}.$$

Note that $\tau_a$ and $\sigma_a$, being amplitudes, are positive by definition. The mean normal stress $\sigma_m$ is taken positive when compressive (see Fig. 2.3). The mean shear stress $\tau_m$ affects the mean position but not the steady state cyclic dissipation (see the first two rows of Table 2.1, as well as Appendix A.3). The dissipation per cycle in this system can be shown to be

---

[3] An anonymous reviewer of the published paper (Jana and Chatterjee, 2013) pointed us to Schallamach waves: see e.g., Barquins (1985). Such waves seem unlikely here.

$$D=[\beta<\frac{\zeta}{\mu}]\times[\zeta>\mu]\times[\beta>-1]\times C\,\sigma_a^2\mu\zeta\left\{(1+\beta)^2\frac{\zeta-\mu}{\zeta+\mu}-[\beta>1](\beta-1)^2\frac{\zeta+\mu}{\zeta-\mu}\right\},\quad(2.3)$$

which includes a single load- and friction-independent fitted constant $C$. The square brackets denote logical variables (equal to 1 if the inequality holds and 0 otherwise). All the results for a given crack should fit this formula (as they do, below).

We observe that $D$ in Eq. (2.3) depends on only two dimensional quantities: the fitted constant $C$ and the normal stress amplitude $\sigma_a$. Consequently, all other nondimensional ratios held constant, $D$ varies as the square of the stress.

Dissipation results from the two dimensional finite element simulations are plotted against the dissipation predicted by Eq. (2.3), with one fitted constant, in Fig. 2.4. The match is excellent. Similar matches, with a different $C$ in each case, were obtained for the circular and triangular cracks in three dimensions (see Appendix A.4). Thus, Eq. (2.3) is acceptable for our purposes.

We now turn to the use of Eq. (2.3) and a Monte Carlo method to compute the *average* dissipation from a multitude of randomly dispersed and oriented microcracks within the material, assuming their interactions may be neglected.

## 2.3 Dissipation due to multiple cracks: Monte Carlo method

We assume that the material is having a very large number of very small cracks which are to a first approximation non-interacting. Under this assumption, adding up the contributions from all the cracks is the same as averaging over all orientations of the cracks and then multiplying by the number of cracks which is just a scalar multiplier. So, effectively up to some scalar multiplier for which we have a fitted constant $C$ in any case, adding it up for all cracks for all possible orientations is the same as the averaging the formula for one crack over all possible orientations.

Similarly, the cracks can have different sizes and adding them all up or averaging is the same. Imagine a plane with certain orientation or a normal. Actually a large

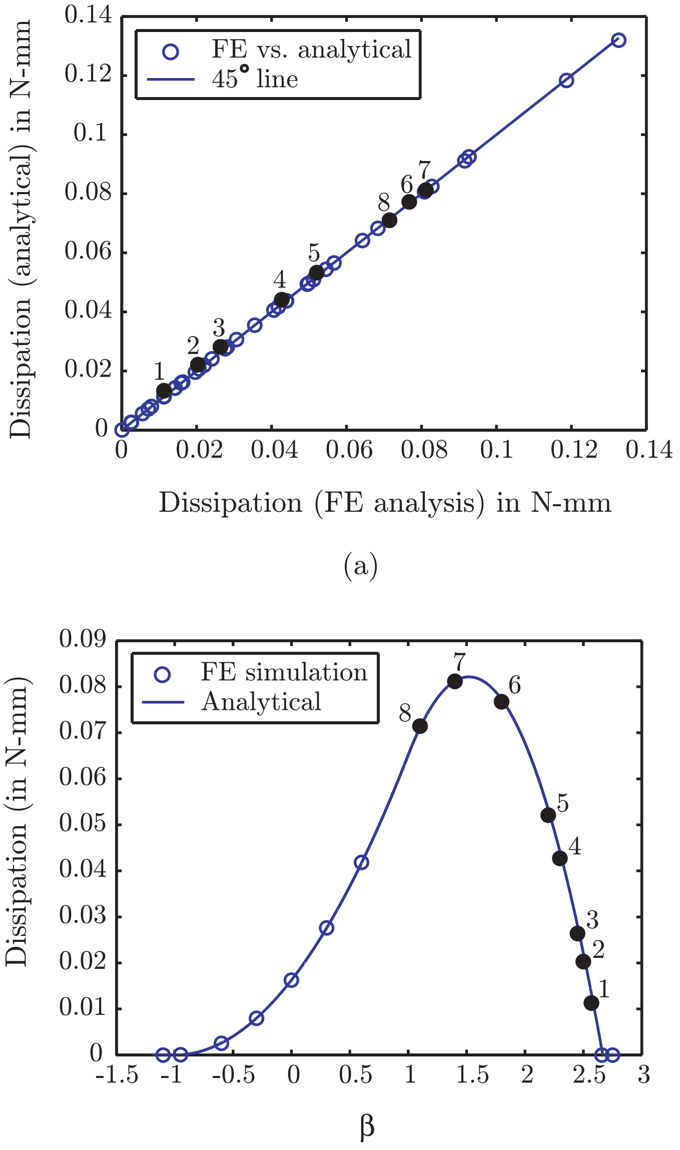

(a)

(b)

Figure 2.4: Analytical formula with a fitted constant $C$ vs. energy dissipation in two dimensional finite element (FE) analysis. Subplot (a) shows all our 2D finite element results. A few points (solid dark circles) show a slight mismatch. These are from a separate sub-calculation for studying never-opening solutions under large compressive mean normal stresses. Subplot (b) shows those results for varying $\beta$ with $\mu = 0.5$, $\sigma_a = 60$ MPa and $\tau_a = 80$ MPa. The mismatch is negligible for our purposes.

number of such planes all parallel to each other can be drawn and imagined passing through the body giving different slices of the body. See Fig. 2.5. Wherever there is a crack which is in the plane that crack is shown. Actually there won't be cracks which *exactly* match the orientation. But we will eventually be doing integration so what we mean is an orientation that almost matches. Now each of these cracks has a contribution to the damping and we will add up their dissipation orientation by orientation. So, for a particular orientation, we will consider all the cracks and calculate their dissipation individually and add them up. Each crack on that plane has a different $C$ and an effective $C$ can be obtained by adding all their dissipations. Because the body is assumed to be isotropic, this effective $C$ is independent of the orientation and assumed to be the same for every orientation. And we appeal to the idea that this effective $C$ can be obtained experimentally. Now, we will hold the $C$ constant over an orientation and find the average dissipation over all possible orientations.

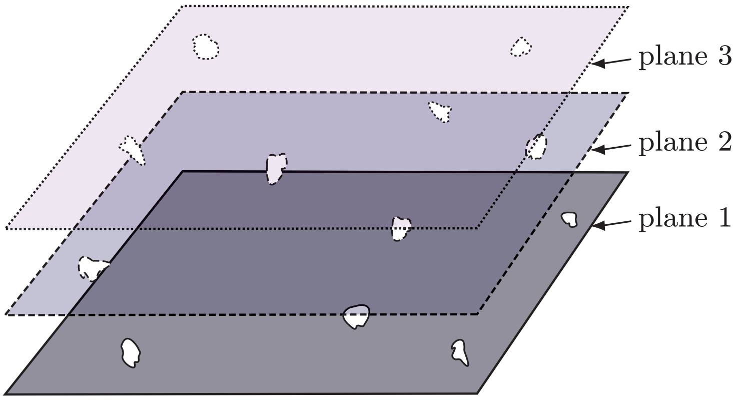

Figure 2.5: A schematic of the cracks at different planes are shown (each plane has four different cracks). Not all possible planes and cracks are shown here.

### 2.3.1 Random orientations

We now consider randomly oriented cracks, and for simplicity assume that all orientations are equally likely, i.e., the material is macroscopically isotropic. Geometrically, the normals ($\widehat{n}$) to the crack faces are uniformly distributed on the surface of the unit hemisphere: see Fig. 2.6. These points were generated by first generating points uniformly distributed within the upper half of a cube, then discarding points that lay outside an appropriate sphere, and finally by projecting the remaining points radially outward onto the surface of the sphere.

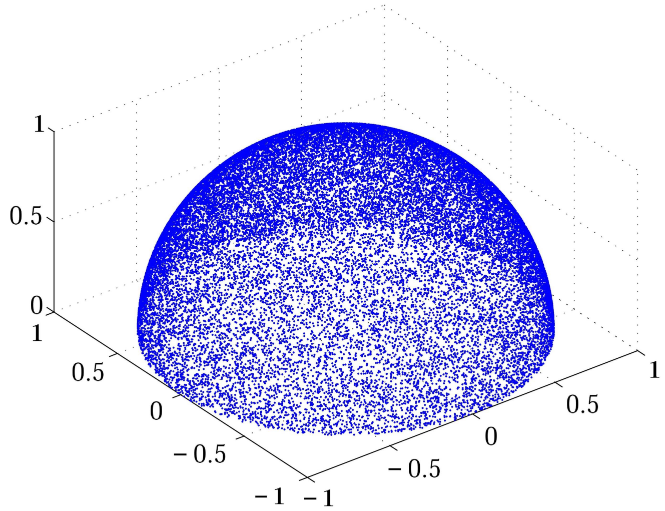

Figure 2.6: 50,000 uniformly distributed points on the unit hemisphere. The actual averaging was done with 4.5 million points and will be treated as accurate.

### 2.3.2 Nondimensionalization

Let the stress state of interest be $\mathbf{S}\sin\omega t$. All orientations of the crack faces being equally likely, the coordinate system is irrelevant. Crack size and shape affect constant $C$, but we assume $C$ is independent of $\widehat{n}$ and can be averaged separately. Here we take $C = 1$; we can multiply by a fitted constant later.

Since the coordinate system used to describe $\mathbf{S}$ is irrelevant, it is simplest to think in terms of principal stresses ($\sigma_1 \geq \sigma_2 \geq \sigma_3$). For $\sigma_1 = \sigma_2 = \sigma_3$ there is no shear stress, $\zeta = 0 < \mu$, and the dissipation is zero (see Eq. (2.3)). Accordingly, we assume $\sigma_1 > \sigma_3$ and first scale the stress so that $\sigma_1 - \sigma_3 = 1$. Later, we will multiply back by the square of the scaling factor (recall the discussion following Eq. (2.3)).

We can visualize the time-harmonic part of the stress state (i.e., matrix $\mathbf{S}$) and associated dissipation possibilities using Mohr's circles for three dimensional stresses. See Fig. 2.7 (a). For any given normal $\widehat{n}$, the resultant shear ($\tau$, assumed positive) and normal stress ($\sigma$), represented as a point $(\sigma, \tau)$ on the Mohr diagram, will lie in a region bounded by three circles (see Malvern (1969)). The dissipation corresponding to any such point will be zero unless the point lies outside the friction wedge, corresponding to $\zeta > \mu$ in Eq. (2.3), as indicated in Fig. 2.7 (a).

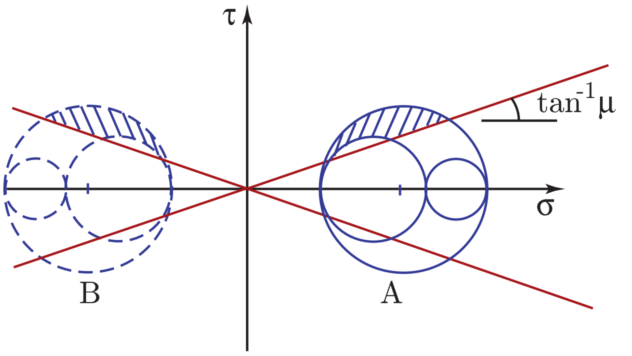

(a)

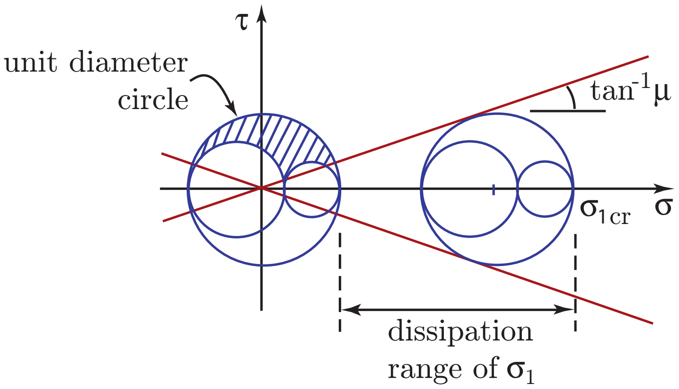

(b)

Figure 2.7: (a) Mohr's circles and dissipation possibilities (shown hatched). (b) Range of scaled $\sigma_1$ for nonzero dissipation.

As indicated in Fig. 2.7 (a), stress state B can be reflected to stress state A, because **S** is multiplied by $\sin \omega t$ in any case. Accordingly, we can assume that the center of the largest Mohr circle is on the nonnegative real axis ($\sigma_1 + \sigma_3 \geq 0$).

Figure 2.7 also shows that, for any $\mu > 0$ and $\sigma_1 - \sigma_3 = 1$, for $\sigma_1$ sufficiently large, there is no dissipation. Conversely, for a state of pure shear, with $\sigma_1 = 0.5$, $\sigma_2 = 0$ and $\sigma_3 = -0.5$, there is nonzero dissipation for any $\mu > 0$. In other words (see Fig. 2.7 (b)), the hydrostatic part of **S** affects the dissipation per cycle.

For clarity, we write down the sign change and scaling described above using a single formula. If the actual time-harmonic state of stress is $\widetilde{\mathbf{S}}\,\sin\omega t$ with eigenvalues $\tilde{\sigma}_1 \geq \tilde{\sigma}_2 \geq \tilde{\sigma}_3$, then we use the scaled stress

$$\mathbf{S} = \{2[\tilde{\sigma}_1 + \tilde{\sigma}_3 \geq 0] - 1\}\,\frac{\widetilde{\mathbf{S}}}{\tilde{\sigma}_1 - \tilde{\sigma}_3}, \tag{2.4}$$

where the square brackets denote a logical variable as before. The principal stresses corresponding to $\mathbf{S}$ are denoted by $\sigma_1 \geq \sigma_2 \geq \sigma_3$. It is now assured that $\sigma_1 + \sigma_3 \geq 0$ and that $\sigma_1 - \sigma_3 = 1$. The scaling factor is

$$k_f = (\tilde{\sigma}_1 - \tilde{\sigma}_3)^{-1}\,, \tag{2.5}$$

and the dissipation obtained using $\mathbf{S}$ will be divided by $k_f^2$ to obtain the dissipation due to $\widetilde{\mathbf{S}}$. Later, for spatially varying stresses in a body vibrating in a given mode, we will use Eq. (2.4) repeatedly using a computer program.

At this point, we have nondimensionalized the stress amplitude $\mathbf{S}$ by taking $C = 1$ and using $k_f$ as above. The nondimensional $\mathbf{S}$ can now be specified by $\sigma_1 \geq 0.5$ along with $\sigma_2 \geq \sigma_1 - 1$. These two nondimensional principal stresses, along with $\mu > 0$, are inputs to the dissipation calculation.

### 2.3.3 Building block: a single average dissipation calculation

We have so far taken three steps towards our goal: (i) we have verified for three dimensions a formula for the dissipation at a single frictional microcrack due to arbitrary oscillating imposed far-field stresses, (ii) we have generated a large number of random normal directions $\widehat{n}$, and (iii) we have nondimensionalized and scaled the stress "amplitude" matrix $\widetilde{\mathbf{S}}$.

Now, for our fourth step, we find the average dissipation for a given scaled stress matrix $\mathbf{S}$, mean stress $\mathbf{S}_0$ (non-time-varying, and identically scaled), and friction $\mu$, by sequentially considering the full random set of normal directions. For the results below, we have used 4.5 million such directions.

For each normal direction $\widehat{n}$, we find the time-varying part of the traction vector

$\mathbf{t} = \mathbf{S} \cdot \widehat{n}$. The normal stress amplitude $\sigma_a$ then is

$$\sigma_a = |\mathbf{t} \cdot \widehat{n}| \, .$$

If a mean stress matrix $\mathbf{S}_0$ is given, the corresponding mean normal stress $\sigma_m$ is similarly calculated using the same $\widehat{n}$. Subtracting $(\mathbf{t} \cdot \widehat{n}) \, \widehat{n}$ from $\mathbf{t}$ gives the shear component of the traction; and its magnitude is $\tau_a$. The shear component is not computed from the mean stress $\mathbf{S}_0$ because it plays no role in cyclic dissipation, as mentioned above (section 2.2.2). Now, for the given $\widehat{n}$, the dissipation is computed using the formula of Eq. (2.3) with the fitted constant $C$ set equal to unity as explained earlier. The above dissipation is finally averaged over all the $\widehat{n}$ to account for the random orientation of the crack.

For simplicity, the nonzero mean stress $\mathbf{S}_0$ is not retained in what follows. $\mathbf{S}_0$ is assumed zero.

For initial demonstration, we consider uniaxial tension and pure shear. The principal stresses for tension are $\sigma_1 = 1$, $\sigma_2 = 0$ and $\sigma_3 = 0$. For shear, they are $\sigma_1 = 0.5$, $\sigma_2 = 0$ and $\sigma_3 = -0.5$. These stresses are already normalized: $\sigma_1 - \sigma_3 = 1$ in both the cases. Dissipations for these cases are calculated for various $\mu$ values (0.01 to 1.2) and shown in Fig. 2.8. The ratio of the two varies significantly with $\mu$. Note that we view $\mu$ as a fitted parameter in our two-parameter constitutive model (the other parameter is the overall multiplicative factor of $C$).

As an example of how $\mu$ might be fitted, consider Robertson and Yorgiadis (1946), who sought the same specific dissipation per cycle in two different loading conditions. For such equal dissipation to occur under both pure (simple) shear and pure extension, the ratio of the shear stress amplitude during torsional vibration to the normal stress amplitude during longitudinal vibration was found to be between 0.48 and 0.60 (for several materials). This statement of equivalence translates, for our model, into roughly $0.6 < \mu < 1.1$ by the following reasoning. Fix the longitudinal stress state at $\sigma_1 = 1$, $\sigma_2 = 0$ and $\sigma_3 = 0$, as above. Let the shearing stress state be $\sigma_1 = 0.5$, $\sigma_2 = 0$ and $\sigma_3 = -0.5$ but only after normalization by some factor $k$; in other words, the applied shear stress would be of amplitude $k/2$. Since

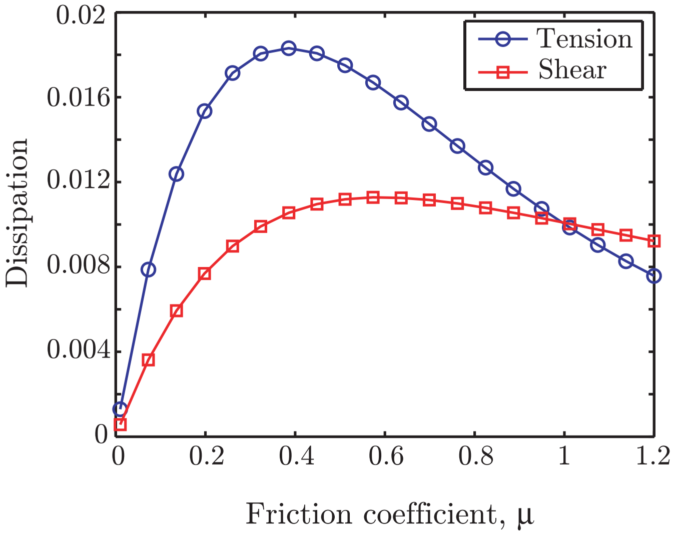

(a)

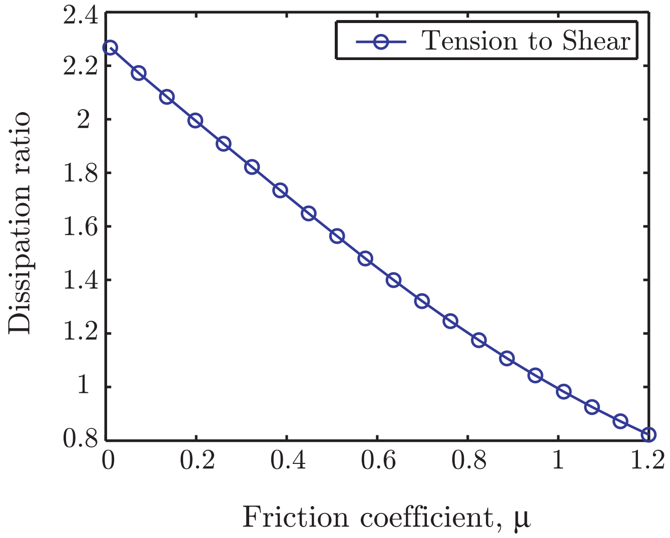

(b)

Figure 2.8: (a) Computed average (Monte Carlo) dissipation with $C = 1$ for tension and pure shear. Here $\mu$ is viewed as a fitted parameter. The stress states remain unchanged for each of the two curves. (b) The ratio of the dissipation for the two stress states against $\mu$, which might in principle be used to estimate $\mu$ (see main text).

the shear stress amplitudes found by Robertson and Yorgiadis (1946) are between 0.48 to 0.6, $k$ lies between 0.96 and 1.2. If $k = 0.96$, the dissipation in shear will be $0.96^2 \approx 0.92$ times the value in Fig. 2.8 (a). Alternatively, the ratio plotted in Fig.

2.8 (b), upon division by 0.92, should give 1, implying $\mu \approx 1.1$. Similarly, if $k = 1.2$, we find $\mu \approx 0.6$.

## 2.4 Fitted formula

So far, the dissipation has been computed as a function of $\mathbf{S}$, possibly a nonzero $\mathbf{S}_0$, and $\mu$, using a time consuming Monte Carlo simulation.

However, we eventually want to compute the modal damping of a given object of arbitrary shape. For each mode, the stress state varies spatially. We cannot do Monte Carlo simulations for every point on the body. So our fifth step is to summarize the dissipation values obtained from Monte Carlo simulations, for the special case of $\mathbf{S}_0 = \mathbf{0}$, using a quick multivariate polynomial fit.

### 2.4.1 A comment on prior efforts

To motivate our multivariate fitted formula, we first note some prior attempts at *ad hoc* modeling of material dissipation under multiaxial stress states. Recall Eq. (2.1), wherein a suitable equivalent stress amplitude needs to be defined. Damping under biaxial stresses has been studied by several authors, including Robertson and Yorgiadis (1946), Whittier (1962), Torvik *et al.* (1963) and Mentel and Chi (1964). All these authors considered at least one *ad hoc* definition equivalent to Eq. (2.2), possibly rearranged or differently normalized. But if Eq. (2.2) had general validity it would apply to our dissipation results as well, since these are derived from legitimate (though approximated) physics. To check the same, we can rewrite Eq. (2.2) as

$$D \approx \lambda_1 \left\{ (\sigma_1 - \sigma_2)^2 + (\sigma_2 - \sigma_3)^2 + (\sigma_3 - \sigma_1)^2 \right\} + \lambda_2 (\sigma_1 + \sigma_2 + \sigma_3)^2, \tag{2.6}$$

where the $\lambda$'s are fitted coefficients, and the assumed roles of the distortional and dilatational strain energies are clearly visible. In checking Eq. (2.6) against our dissipation results, we note that different $\mu$ represent different material behaviors, and so we should work with one $\mu$ at a time. Figures 2.9 (a) and (b) show least squares fitted comparisons for two $\mu$ values. Each data point in these figures corresponds to a normalized ($\sigma_1 - \sigma_3 = 1$) state of stress. For both $\sigma_1 \geq 0.5$ and $\sigma_2 \geq \sigma_1 - 1$, several equally spaced grid points are taken. The poor match in Figures 2.9 (a) and (b) indicates the inapplicability of Eq. (2.6) in general cases; it also motivates our multivariate polynomial fit below.

### 2.4.2 Inputs to the fitted multivariate polynomial formula

The scaled stress $\mathbf{S}$ and $\mu$ are inputs for our dissipation calculation. We will later divide the computed dissipation by $k_f^2$ (see Eqs. (2.4) and (2.5)) to obtain the dissipation for the actual stress $\widetilde{\mathbf{S}}$. We now introduce two new scaled variables.

First, define $\chi = \sigma_1 - \sigma_2$. The inequality $\sigma_1 - 1 \leq \sigma_2 \leq \sigma_1$ becomes $0 \leq \chi \leq 1$. Figure 2.7 (b) shows the nonzero-dissipation range of $\sigma_1$ as $0.5 \leq \sigma_1 \leq \sigma_{1cr}$, where

$$\sigma_{1cr} = \frac{1}{2} + \frac{\sqrt{1+\mu^2}}{2\mu}. \tag{2.7}$$

For $\sigma_1 \geq 0.5$ and $0 \leq \chi \leq 1$, with $\mu$ as a parameter, we now generate surface plots of the dissipation as computed from Monte Carlo simulations. We compute 11 such surface plots, for equally spaced $\mu$ values from 0.2 to 1.2. Two representative plots are shown in Fig. 2.10; another nine are shown in Fig. 2.11.

The figures confirm that the dissipation does become zero for each $\mu$ when $\sigma_1$ crosses $\sigma_{1cr}$ (Eq. (2.7)).

We now introduce a final scaled variable

$$s = 1 - \frac{(\sigma_1 - 0.5)}{(\sigma_{1cr} - 0.5)}, \tag{2.8}$$

such that there is nonzero dissipation only for $s > 0$. We will now seek a single fitted formula for all these dissipation surfaces, given $s$, $\chi$, and $\mu$.

### 2.4.3 Multivariate polynomial fit

Recall Eq. (2.3). Now setting $C = 1$ (different $C$ will be incorporated later), and for $\beta = 0$ (zero mean stress), we write

$$D_f = \text{average of}\left\{[\zeta > \mu] \times \sigma_a^2 \mu \zeta \frac{\zeta - \mu}{\zeta + \mu}\right\}, \tag{2.9}$$

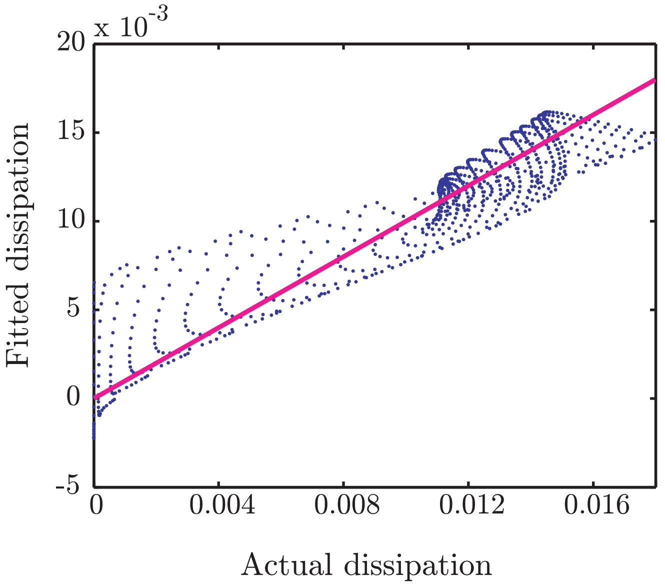

(a) μ=0.5

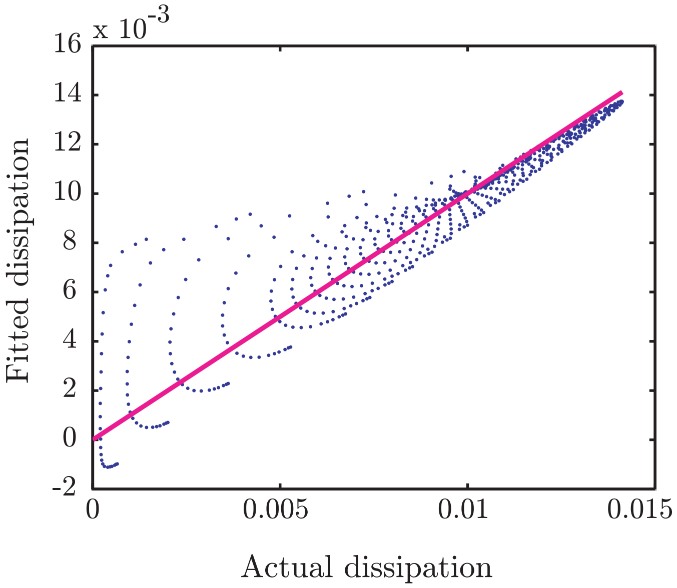

(b) μ=0.9

Figure 2.9: Comparison of Eq. (2.6) against our dissipation model for two $\mu$ values (different least squares fits used in each subplot, for $\lambda_1$ and $\lambda_2$). The plotted straight lines are at 45 degrees, for reference. These plots may be compared against Fig. 2.12 (b) below.

where the average is over all possible orientations of the crack face. We propose, for simplicity, a polynomial form for the fit:

$$D_f = \sum_{m_0,m_1,m_2} \overline{B}_{m_0 m_1 m_2}\, s^{m_0} \chi^{m_1} \mu^{m_2}, \quad 1 \le m_0 \le 5,\ 0 \le m_1 \le 4,\ 0 \le m_2 \le 3, \tag{2.10}$$

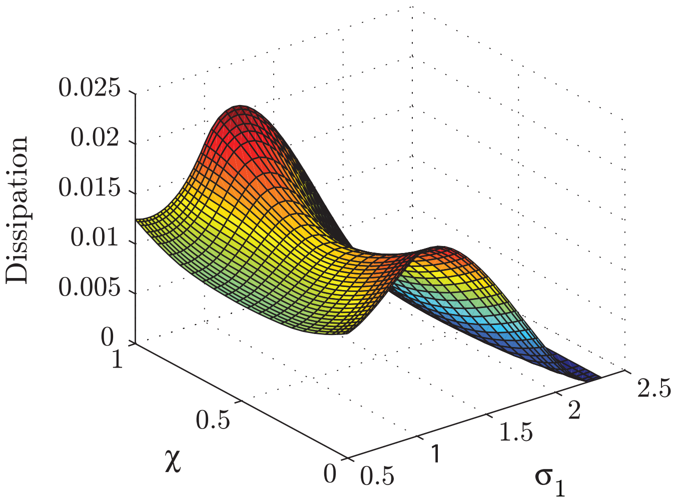

(a) μ=0.3

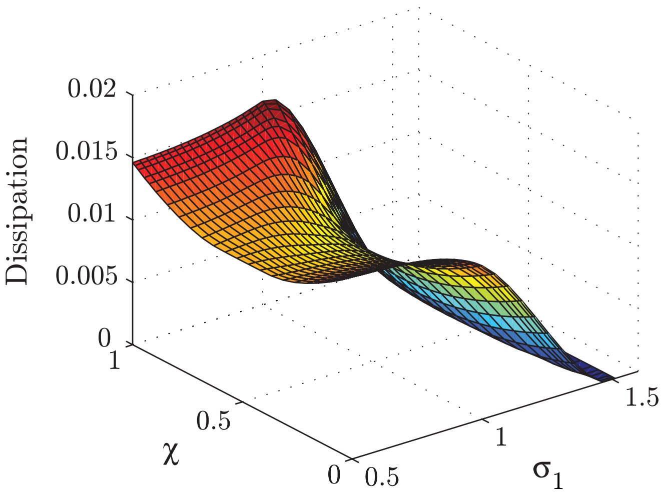

(b) μ=0.6

Figure 2.10: Dissipation surface plots for two $\mu$ values.

where the $\overline{B}_{m_0m_1m_2}$'s collectively denote 100 fitted coefficients. Our numerical fit will be much faster than Monte Carlo simulation, and given below in an easily portable form. In particular, $D_f$ will be written as a product of three matrices, **ABM**, and the constitutive relation for damping will be

$$D = C \times [s > 0] \times \mathbf{ABM}. \tag{2.11}$$

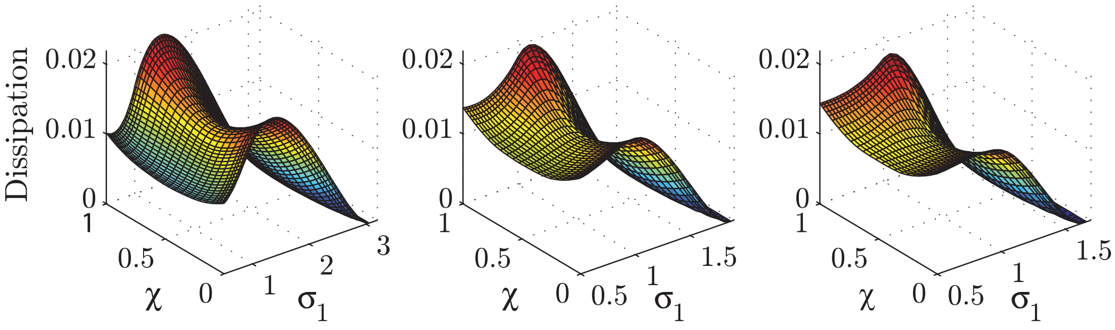

(a) μ = 0.2 (b) μ = 0.4 (c) μ = 0.5

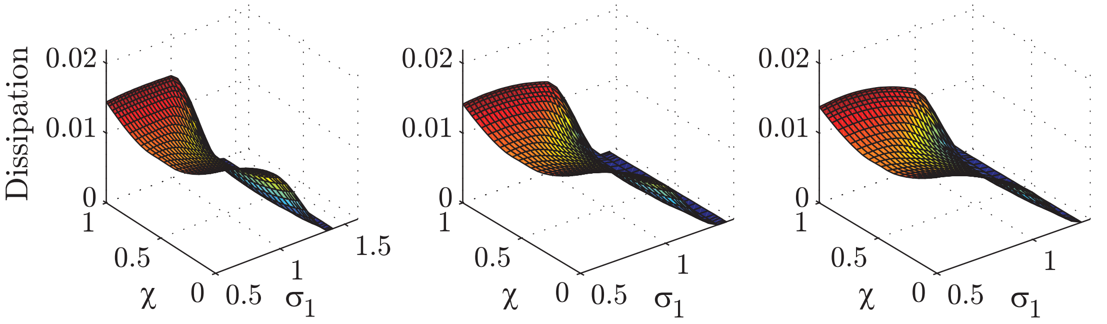

(d) μ = 0.7 (e) μ = 0.8 (f) μ = 0.9

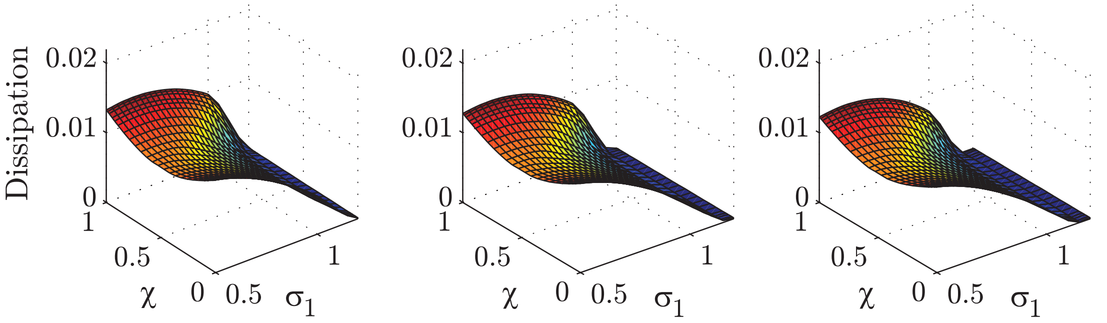

(g) μ = 1.0 (h) μ = 1.1 (i) μ = 1.2

Figure 2.11: Dissipation plot for other $\mu$ values.

Here $D$ (as before) is the dissipation per unit volume and per stress cycle due to scaled stress $\mathbf{S}$, $C$ is a fitted scalar coefficient, $[s > 0]$ is a logical variable that ensures zero dissipation for $s \leq 0$ (see Eq. (2.8)), $\mathbf{M}$ is a column vector containing powers of $\chi$ as described below, $\mathbf{A}$ is a row vector containing products of powers of $s$ and $\mu$ as described below, and the matrix $\mathbf{B}$ contains fitted numerical coefficients.

We write **M** and **A** as follows:

$$\mathbf{M} = \left[ \begin{array}{ccccc} 1 & \chi & \chi^2 & \chi^3 & \chi^4 \end{array} \right]^T \quad \text{and} \quad \mathbf{A} = \left[ \begin{array}{cccc} \mathbf{A_0} & \mathbf{A}_1 & \mathbf{A}_2 & \mathbf{A}_3 \end{array} \right], \tag{2.12}$$

with $\mathbf{A}_0 = \left[ \begin{array}{ccccc} s & s^2 & s^3 & s^4 & s^5 \end{array} \right]$ and $\mathbf{A}_m = \mu^m \mathbf{A}_0$.

The fitted $20 \times 5$ matrix **B**, determined from a least squares calculation, is given in Appendix A.5. In the fit, the maximum absolute error as a percentage of the maximum for each corresponding $\mu$ is within 5.2%, with typical errors being substantially smaller.

Figure 2.12 shows the quality of the fit for $\mu = 0.4$. Figure 2.12 (a) shows two surface plots. One surface is from Monte Carlo simulation (accurate) and the other is from the fitted polynomial. The match is good. Another comparison is shown in Fig. 2.13, where all the data points used in the fit are plotted, fitted value against original Monte Carlo value, along with a 45° line. Within this plot are represented 11 equally spaced $\mu$ values from 0.2 to 1.2. The match is reasonably good, and can be improved if desired by using higher order polynomials or other fitting methods. But dissipation, like other nonideal material behaviors involving friction, fracture and plasticity, is difficult to model accurately in any case; so we arbitrarily chose to limit the number of fitting coefficients to 100, arranged in a matrix that is easy to cut and paste.

An illustration of our dissipation calculation is now given for completeness. Let the state of stress be

$$\widetilde{\mathbf{S}} = \left[ \begin{array}{ccc} 1 & 2 & 3 \\ 2 & 5 & 4 \\ 3 & 4 & 6 \end{array} \right],$$

an arbitrary choice. The principal stresses are $\tilde{\sigma}_1 = 10.833, \tilde{\sigma}_2 = 1.577, \tilde{\sigma}_3 = -0.410$. The scaling factor $k_f = 0.089$, and the normalized eigenvalues work out to $\sigma_1 = 0.964, \sigma_2 = 0.140, \sigma_3 = -0.036$, giving $\chi = 0.824$. We take $\mu = 0.5$. Then $\sigma_{1cr} = 1.618$, giving $s = 0.585$. Now using Eq. (2.11) with $C = 1$ we find $D = 0.014$. Finally, the dissipation is $D/(k_f)^2 = 1.818$ in appropriate units.

Two further aspects of the fit are mentioned here.

First, the polynomial fit occasionally predicts some small negative values, as

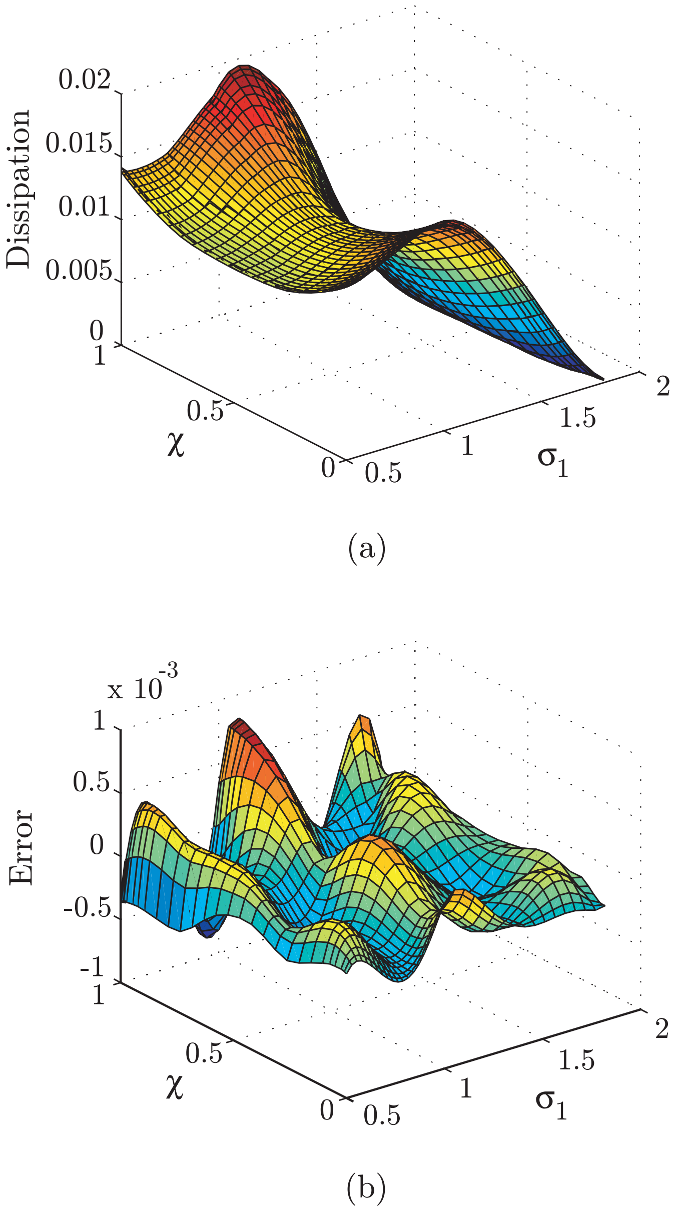

Figure 2.12: Dissipation comparison for $\mu = 0.4$ with $C = 1$: (a) superimposed dissipation plots, (b) error plot (Monte carlo − fitted formula).

suggested by the bottom left portion of Fig. 2.13. We simply replace those negative predictions with zero, with negligible consequence because such values are both infrequently encountered and small.

Secondly, the dissipation computation using our fitted formula is very fast compared to the Monte Carlo Method. 10,000 evaluations of the formula, with randomly chosen stress states and $\mu$, took about 0.2 seconds on an unremarkable desktop

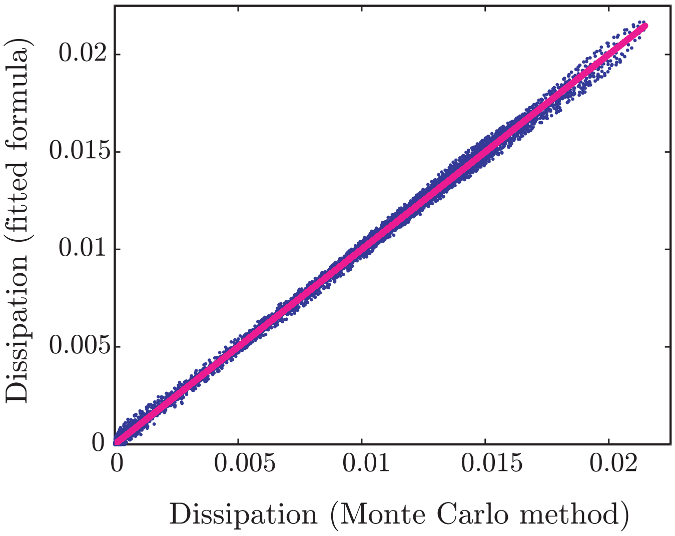

Figure 2.13: Dissipation comparison for all $\mu$ values with $C = 1$ (a 45° line is also shown in this plot).

computer, where a single Monte Carlo evaluation with 4.5 million points (found separately to be large enough for the accuracy needed) took about 3 minutes.

## 2.5 Finite element computation of modal damping

We have now completed all the steps needed to consider the effective modal damping of any given mode of an arbitrarily shaped object. We will illustrate our calculations using the solid body shown in Fig. 1.1 (a).

For completeness, we have included a brief introduction to relevant aspects of vibration theory in Appendix A.6. The key ideas are summarized as follows. The damping mechanism we have considered is nonlinear, but the damping is assumed to be small. For small damping, the damping plays no significant role except near resonance. Near each distinct resonant frequency (or natural frequency) of an arbitrary body, an effective damping ratio for the corresponding mode can be defined. This section is concerned with the computation of such effective *modal* damping values.

### 2.5.1 Effective damping ratio ($\zeta_{\mathit{eff}}$)

We begin with an elementary formula. A lightly damped harmonic oscillator of the form

$$\ddot{x} + 2\zeta\omega_n\dot{x} + \omega_n^2 x = 0 \tag{2.13}$$

has damping ratio $\zeta$ which, to first order, is equivalent to

$$\zeta_{\mathit{eff}} = \frac{1}{4\pi} \times \left(\frac{-\Delta\overline{E}}{\overline{E}}\right) \tag{2.14}$$

where $-\Delta\overline{E}$ is the energy dissipated per oscillation, $\overline{E}$ is the total energy of the system averaged over one cycle, and the bar is to distinguish the energy from the Young's modulus which will be discussed later. Equation (2.14) works only for lightly damped systems because $-\Delta\overline{E}$ is computed over a cycle by assuming a harmonic solution. However, it is general: it does not need a linear viscous model. The general unforced solution is then approximated as

$$x \approx e^{-\zeta\omega_n t} A \cos\left(\sqrt{1-\zeta^2}\,\omega_n t + \phi\right).$$

For small $\zeta$, we may often just write

$$x \approx e^{-\zeta\omega_n t} A \cos\left(\omega_n t + \phi\right).$$

For a simple analytical example, consider

$$\ddot{x} + c|x|\mathrm{sign}(\dot{x}) + x = 0. \tag{2.15}$$

Assume first an approximate solution (neglecting the damping over one cycle) of

$$x \approx A\sin t \quad \text{and} \quad \overline{E} = \frac{A^2}{2}$$

from the maximum potential or kinetic energy. The energy dissipation per cycle is, by this approximation,

$$-\Delta\overline{E} = \int_0^{2\pi} c|x|\mathrm{sign}(\dot{x})\dot{x}\,dt = cA^2\int_0^{2\pi} |\sin(t)\cos(t)|\,dt = 2\,cA^2, \tag{2.16}$$

whence by Eq. (2.14) we have

$$\zeta_{eff} = \frac{c}{\pi}.$$

A numerical solution of the nonlinear Eq. (2.15) with $c = 0.1$ and initial conditions $x(0) = 1$ and $\dot{x}(0) = 0$ is shown in Fig. 2.14. A plot of $e^{-ct/\pi}$ is also given for comparison, and is seen to match the oscillation envelope very well.

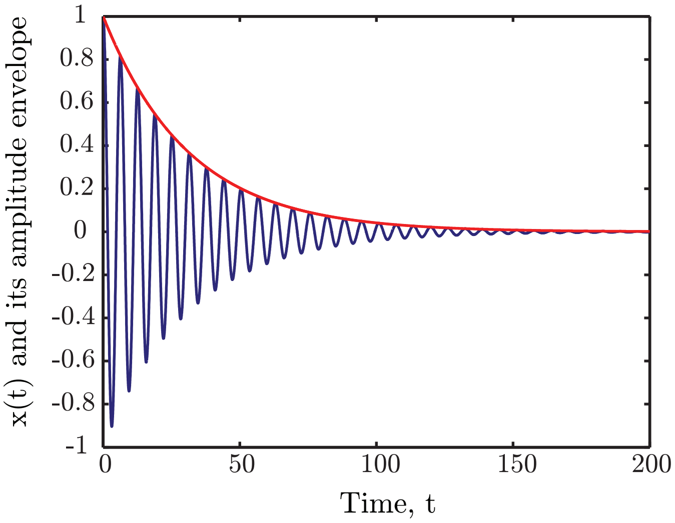

Figure 2.14: Numerical solution of Eq. (2.15) using Matlab's "ode15s." The initial condition was changed from $\dot{x}(0) = 0$ to $\dot{x}(0) = 10^{-10}$ to avoid the immediate discontinuity at zero. The amplitude envelope approximation of $e^{-ct/\pi}$ matches near-perfectly.

The above example shows the utility of Eq. (2.14), which we will use below. The energy dissipation calculation below will use our fit of Eq. (2.11), suitably integrated over the entire vibrating object.

### 2.5.2 Finite element prediction of effective damping ratio

Our finite element computation of mode shapes and modal damping proceeds as follows. We have used the finite element package ANSYS for modal analysis and related computations in this thesis. Elementwise integrals below will use Gaussian quadrature (see Bathe (1996)).

The vibrating object of interest is first meshed using 10 noded tetrahedral elements (SOLID187) using automatic meshing within ANSYS. Modal analysis in

ANSYS yields natural frequencies and mass-normalized mode shapes. Nodal displacements for each mode of interest are extracted using a small external program.

Using the element shape functions and the nodal displacements, the displacement field is computed and then differentiated to obtain strains, and thence stresses, at 4 Gauss points per element. At each Gauss point, the stress is used in conjunction with Eq. (2.11) to compute the dissipation per unit volume and per cycle. The dissipation in the element is then obtained by the usual weighted sum of its values at the Gauss points; and the same is added up for all the elements to obtain the total energy dissipated per cycle in the vibrating object. This dissipation is $-\Delta\overline{E}$.

$\overline{E}$ is simply $\omega^2/2$ because the mode shape is mass normalized.

Now, the effective damping ratio is obtained using Eq. (2.14). Details of these calculation are provided below.

### 2.5.3 Details of $\zeta_{\mathit{eff}}$ computation using ANSYS

Here, we give the details of our finite element based calculation of $\zeta_{\mathit{eff}}$ using ANSYS. A 10 noded tetrahedral element (SOLID187), shown in Fig. 2.15, is used to model the geometry of the structure.

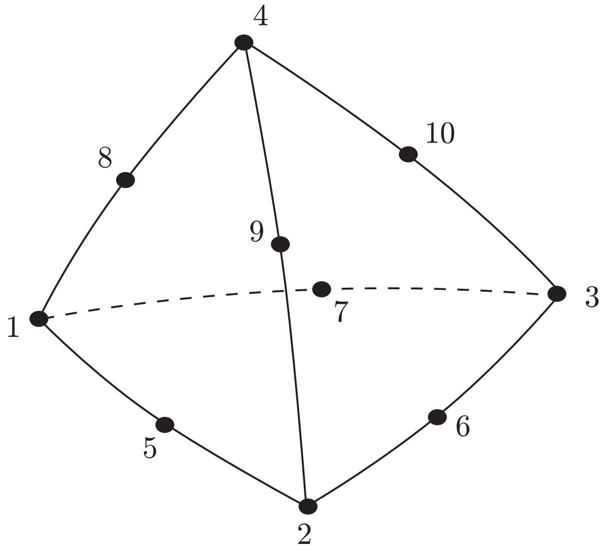

Figure 2.15: 10 noded tetrahedral element

| | 1 | 2 | 3 | 4 | 5 | 6 | 7 | 8 | 9 | 10 |
|---|---|---|---|---|---|---|---|---|---|---|
| $\zeta_1$ | 1 | 0 | 0 | 0 | 0.5 | 0 | 0.5 | 0.5 | 0 | 0 |
| $\zeta_2$ | 0 | 1 | 0 | 0 | 0.5 | 0.5 | 0 | 0 | 0.5 | 0 |
| $\zeta_3$ | 0 | 0 | 1 | 0 | 0 | 0.5 | 0.5 | 0 | 0 | 0.5 |
| $\zeta_4$ | 0 | 0 | 0 | 1 | 0 | 0 | 0 | 0.5 | 0.5 | 0.5 |

Table 2.2: Volumetric coordinates and their nodal values for the SOLID187 element (see ANSYS manual, 2009).

The shape functions for the element are given by,

$$\begin{aligned} N_i &= \zeta_i(2\zeta_i - 1) \text{ for } \ i = 1,2,3,4 \\ N_5 = 4\zeta_1\zeta_2; \quad N_6 &= 4\zeta_2\zeta_3; \quad N_7 = 4\zeta_1\zeta_3 \\ N_8 = 4\zeta_1\zeta_4; \quad N_9 &= 4\zeta_2\zeta_4; \quad N_{10} = 4\zeta_3\zeta_4. \end{aligned} \tag{2.17}$$

Here $\zeta_1$, $\zeta_2$, $\zeta_3$ and $\zeta_4$ are local volumetric coordinates and their nodal values are given in Table 2.2.

Modal analysis of the finite element model is carried out in ANSYS and nodal displacements for each mass-normalized mode ($\boldsymbol{\phi}$) are extracted. For each mode,

$$\int_V \rho \boldsymbol{\phi}^{\mathsf{T}} \boldsymbol{\phi} \, dV = 1, \tag{2.18}$$

where $\rho$ is the mass density.

The strain components for this element can be written as

$$\boldsymbol{\epsilon} = \mathbf{F}\mathbf{u} \tag{2.19}$$

where $\boldsymbol{\epsilon}$ and $\mathbf{u}$ are the strain and displacement column matrices ("vectors") respectively and the matrix $\mathbf{F} = \nabla \mathbf{N}$ where $\mathbf{N}$ denotes the column matrix ("vector") of shape functions. Note that $\boldsymbol{\epsilon}$ is $6 \times 1$ (for the six independent elements of the infinitesimal strain tensor), and $\mathbf{u}$ is $30 \times 1$ (three displacement components each, for ten nodes). Now the stress components are computed using

$$\boldsymbol{\sigma} = \mathbf{E_s}\boldsymbol{\epsilon} \tag{2.20}$$

where $\boldsymbol{\sigma}$ is the $6 \times 1$ vector of the independent stress components and $\mathbf{E_s}$ is the $6 \times 6$

| GP | $\zeta_1$ | $\zeta_2$ | $\zeta_3$ | $\zeta_4$ | $w$ |
|---|---|---|---|---|---|
| 1 | .585410196625 | .138196601125 | .138196601125 | .138196601125 | .25 |
| 2 | .138196601125 | .585410196625 | .138196601125 | .138196601125 | .25 |
| 3 | .138196601125 | .138196601125 | .585410196625 | .138196601125 | .25 |
| 4 | .138196601125 | .138196601125 | .138196601125 | .585410196625 | .25 |

Table 2.3: Gauss points and weights for four point Gauss quadrature scheme (see ANSYS manual, 2005).

matrix

$$\mathbf{E_s} = \frac{E}{(1+\nu)(1-2\nu)}\begin{bmatrix} 1-\nu & \nu & \nu & 0 & 0 & 0 \\ \nu & 1-\nu & \nu & 0 & 0 & 0 \\ \nu & \nu & 1-\nu & 0 & 0 & 0 \\ 0 & 0 & 0 & \frac{1}{2}-\nu & 0 & 0 \\ 0 & 0 & 0 & 0 & \frac{1}{2}-\nu & 0 \\ 0 & 0 & 0 & 0 & 0 & \frac{1}{2}-\nu \end{bmatrix}, \qquad (2.21)$$

where in turn $E$ is Young's modulus and $\nu$ is Poisson's ratio. The procedures involved are routine in finite element based stress analysis.

We have used a four point Gauss quadrature scheme to compute the dissipation over each element volume. At each Gauss point (see Table 2.3), the strain components are computed from the nodal displacements extracted from the modal analysis (using Eq. (2.19)). Then the stress components are computed using Eq. (2.20). The stress components are then expressed in a symmetric $3 \times 3$ matrix and scaled according to Eq. (2.4). Then the dissipation is calculated for the scaled stress for a given $\mu$ value using Eq. (2.11). For each Gauss point the dissipation is then divided by the appropriate $k_f^2$ (see Eq. (2.5)).

Now, the dissipation over each element is integrated using

$$(D)^e = \sum_{k=1}^{4} w_k D_{g(\underline{\zeta},_k)} \left|\mathbf{J}_{(\underline{\zeta},_k)}\right|. \qquad (2.22)$$

Here, $(\underline{\zeta},_k)$ denotes the coordinate quartet $(\zeta_1, \zeta_2, \zeta_3, \zeta_4)$ at the $k^{\text{th}}$ Gauss point, $w_k$ are the weights of the Gauss quadrature scheme, $\left|\mathbf{J}_{(\underline{\zeta},_k)}\right|$ is the determinant of the corresponding Jacobian matrix, and $D_{g(\underline{\zeta},_k)}$ is the dissipation calculated at the $k^{\text{th}}$ Gauss point.

The total dissipation per cycle in the entire object is the sum of all the elemental integrals. That is,

$$-\Delta\overline{E} = \sum_{\text{all elements}} (D)^e. \tag{2.23}$$

The total kinetic energy of the model in this vibration mode is

$$\overline{E} = \frac{1}{2}\omega^2 \int_V \rho \boldsymbol{\phi}^{\mathsf{T}} \boldsymbol{\phi}\, dV = \frac{\omega^2}{2} \tag{2.24}$$

where $\omega$ is the natural frequency (known, along with $\boldsymbol{\phi}$, from modal analysis). Using Eq. (2.23) and Eq. (2.24) we now obtain the effective damping ratio ($\zeta_{\mathit{eff}}$) as

$$\zeta_{\mathit{eff}} = \frac{1}{4\pi} \times \left( \frac{-\Delta\overline{E}}{\overline{E}} \right) = \frac{1}{4\pi} \times \frac{\sum (D)^e}{\frac{1}{2}\omega^2}. \tag{2.25}$$

### 2.5.4 Results for an arbitrary solid object

We finally consider the solid object shown in Fig. 1.1 (a) in Chapter 1. It is not special, and merely represents an object that is difficult or impractical to treat analytically. The object is an unconstrained thick circular plate of radius 1 m and thickness 0.1 m, with a square hole. The edges of the hole are 0.4 m, and its center is 0.5 m from the center of the circle. The Young's modulus ($E$), Poisson's ratio ($\nu$), and density ($\rho$) of the material are arbitrarily taken as 100 GPa, 0.28, and 4000 Kg/m$^3$ respectively.

32,418 elements were used for meshing the object. The effective damping was computed for the first three vibration modes. The first mode was shown in Fig. 1.1 (b). The second and third modes are shown in Fig. 2.16.

Noting that $C$ has units of Pa$^{-1}$, we have arbitrarily chosen $C = 2\pi/E$, where the dependence on $E$ is motivated by the units and the $2\pi$ ensures that, for axial vibrations of a uniform rod, the effective damping is exactly equal to $D_f$ in Eq. (2.10). In real applications, where $C$ would be fitted from test data, the $2\pi$ would be replaced with a fitted constant.

We pause for a moment to take stock. Recall that our dissipation model has two fitted parameters, namely $C$ and $\mu$. $C$ is an overall measure of dissipation, and has been arbitrarily assumed to be $C = 2\pi/E$ above. The parameter $\mu$ governs the

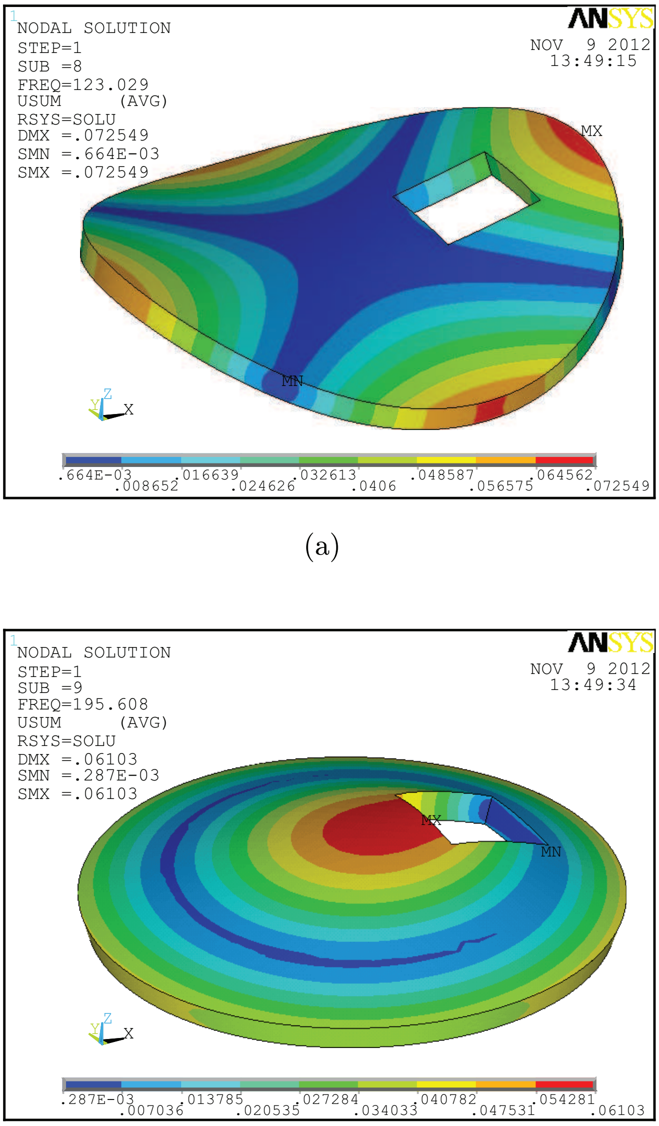
NODAL SOLUTION
STEP=1
SUB =8
FREQ=123.029
USUM (AVG)
RSYS=SOLU
DMX =.072549
SMN =.664E-03
SMX =.072549
ANSYS
NOV 9 2012
13:49:15
MX
MN
Y
Z
X
.664E-03
.008652
.016639
.024626
.032613
.0406
.048587
.056575
.064562
.072549
NODAL SOLUTION
STEP=1
SUB =9
FREQ=195.608
USUM (AVG)
RSYS=SOLU
DMX =.06103
SMN =.287E-03
SMX =.06103
ANSYS
NOV 9 2012
13:49:34
MX
MN
Y
Z
X
.287E-03
.007036
.013785
.020535
.027284
.034033
.040782
.047531
.054281
.06103

(a)

(b)

Figure 2.16: Vibration modes of the solid body: (a) second mode, (b) third mode. The first mode was shown in Fig. 1.1 (b).

relative importance of different components of the stress in the material, as discussed earlier (recall Fig. 2.8). Here, we present simulation results for a range of $\mu$ values. Note that the absolute magnitude of the damping ratio for any mode depends on both $C$ and $\mu$, but the *relative* magnitudes (or ratios) of two modal damping ratios is a function of $\mu$ alone.

We now present our illustrative finite element results. Values of $\zeta_{\mathit{eff}}$ against $\mu$ are shown for the first three vibration modes in Fig. 2.17. For the first two modes, the

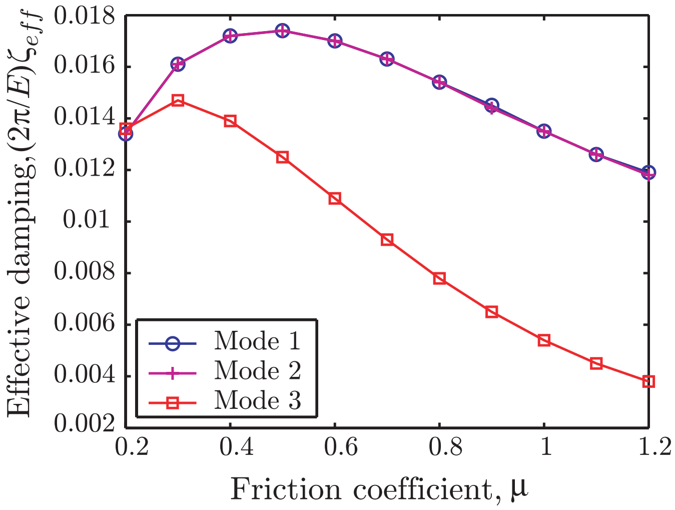

(a)

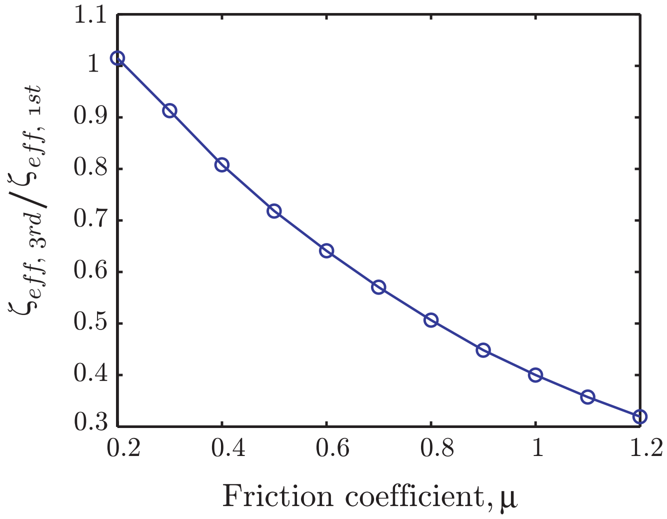

(b)

Figure 2.17: (a) Damping ratios for the first three modes. (b) The ratio of the effective damping ratio of the third mode to that of the first mode.

dependence on $\mu$ is near identical. However, for the third mode, it differs significantly (see the differences in deformation patterns[4] in Figs. 1.1 and 2.16). Such differences might be used to estimate $\mu$ (recall the discussion following Fig. 2.8).

---

[4] The first two modes are the bending modes whereas the third mode is a kind of breathing mode. It is observed that the stress pattern (for example, the von-Mises stresses) in the first two modes are similar whereas it is different in the third mode. That is why we see similar damping values for the first two modes and a significantly different value in the third mode.

## 2.6 Summary

In this chapter, we have traced out a possible route for computing the modal damping ratios of arbitrarily shaped objects. We have first adopted a dispersed frictional microcrack based model of dissipation in an otherwise elastic body. We have verified a single simple formula based on a sliding spring-block analogy that accurately describes the energy dissipation per cycle as obtained from both two and three dimensional computations. To account for the random orientations of the cracks, we have used Monte Carlo averaging for any given state of (time-periodic) stress. We have summarized the Monte Carlo simulation results for a range of the friction parameter $\mu$ and for arbitrary triaxial stresses using a multivariate polynomial fit. The polynomial, with three independent variables and 100 fitted coefficients, is fairly accurate and arranged for easy portability.

Finally, we have chosen for demonstration a body of somewhat complex shape. Using commercial finite element code, we have found its first few natural frequencies and mode shapes. For each mode, we have extracted the nodal displacements, computed stresses at Gauss points, used the fitted formula to estimate dissipation rates, integrated over the body to find the net dissipation, and thereby computed the modal damping up to a fitted constant $C$ and for a range of $\mu$.

We anticipate that this line of work may have useful applications and extensions in future work. Clearly, such modeling provides a route to optimizing engineering component designs for damping. Additionally, such work may lead to new academic research towards incorporating residual stresses, other dissipation mechanisms, anisotropy in material properties or flaw distributions, interactions between flaws, etc.

In the next two chapters, we will study the other rate-independent dissipation phenomena: ambient-temperature plasticity. Specifically, we will consider dissipation due to dispersed microscopic elastic perfectly-plastic flaws. Assuming that these flaws are randomly dispersed, and have a random distribution of strengths, we will find the average dissipation from these flaws under arbitrary triaxial periodic stress.

# Chapter 3

# Dissipation due to individual microscopic elasto-plastic flaws

## 3.1 Introduction

In this thesis, we are considering internal dissipation formulas of the form

$$D = \xi \sigma_{eq}^{m}. \tag{3.1}$$

As stated earlier the definition of $\sigma_{eq}$ in the multiaxial case is of primary interest. To define such a $\sigma_{eq}$, we are considering underlying micromechanical models of dissipation. Guided by empirical evidence of rate-independence, we are considering Coulomb friction and ambient-temperature rate-independent plasticity. Of these two, Coulomb friction was discussed in the previous chapter and this chapter is devoted to the study of plastic dissipation due to microscopic flaws.

We first discuss dissipation in a simple unidimensional model to demonstrate the kind of formula we seek. Subsequently, we discuss dissipation in a three dimensional plastic flaw. Results of this chapter will be implemented in the next chapter where we will discuss macroscopic dissipation due to a randomly distributed multitude of such microscopic plastic flaws.

## 3.2 Unidimensional dissipation model

The aim of this section is to motivate the specific approach we adopt for three dimensional flaws in subsequent sections.

See the schematic in Fig. 3.1. The friction element sustains a maximum force $f$, and then slides. When there is no sliding, the net stiffness is $k_0$. When there is sliding, the stiffness for incremental motions is $k_0 - k_1$. The model represents a small volume of otherwise-elastic material with a single dissipative yielding location.

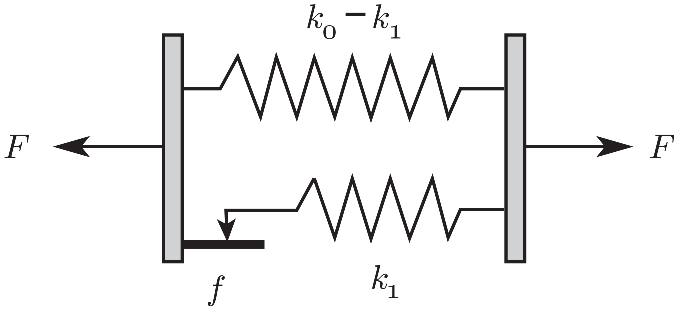

Figure 3.1: One-dimensional dissipation model.

The force-displacement (representing stress-strain) diagram of the model of Fig. 3.1 is shown in Fig. 3.2 (a). Beginning from zero compression in both the springs, if we increase $F$, both springs stretch up to a point. Subsequently, the frictional contact slides while maintaining a constant frictional force. When we decrease $F$, both springs begin to unload elastically. Eventually the frictional contact slides again, this time in the opposite direction. Since we are interested in periodic motions, we assume that the mean position of the frictional slider is at zero. Oscillation amplitudes greater than $\frac{f}{k_1}$ are accompanied by dissipation, while those with smaller amplitudes involve no dissipation. In the figure, an oscillation of amplitude $A > \frac{f}{k_1}$ is indicated. The dissipated energy is equal to the shaded area, which is

$$E_d = 4f(A - \frac{f}{k_1}). \tag{3.2}$$

In this case the dissipation is a bi-linear function of $A$. See Fig. 3.2 (b). For $A < \frac{f}{k_1}$ the dissipation is zero and for $A > \frac{f}{k_1}$, it varies linearly with $A$.

By analogy, the per-cycle dissipation in any equivalent dissipative element can be written as

$$E_d = ks\,(A - s) \quad \text{if } A > s, \quad \text{and 0 otherwise.} \tag{3.3}$$

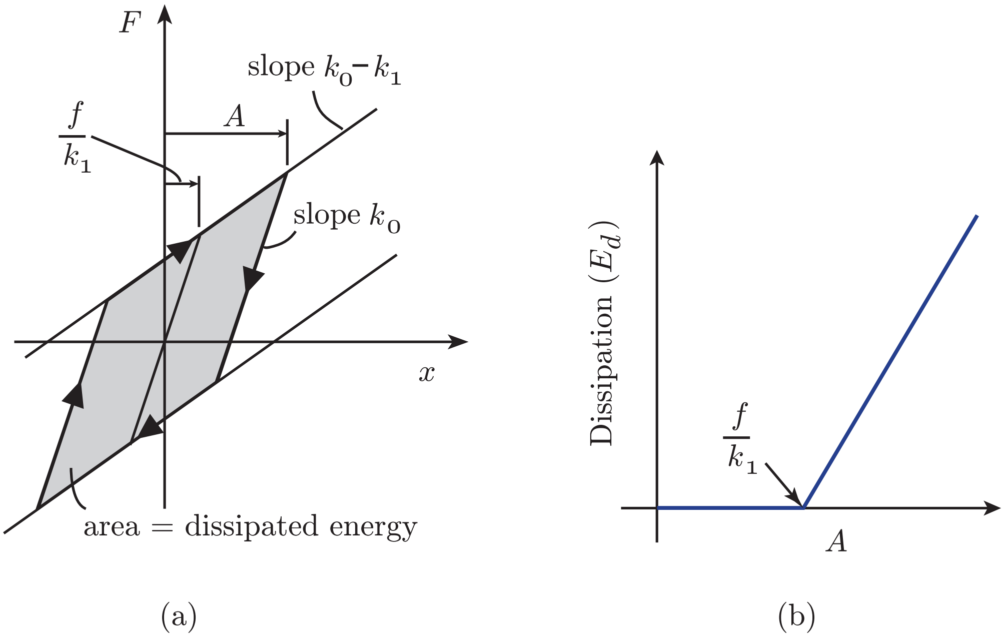

(a) (b)

Figure 3.2: Dissipation in the one-dimensional model. (a) Shaded area shows the energy dissipated in one cycle of amplitude $A > \frac{f}{k_1}$. (b) Dissipation against amplitude $A$.

Here, $A$ is the amplitude of a suitable quantity related to stress, $s$ is some threshold strength, and $k$ corresponds to the stiffness and size of the flaw. Therefore, Eq. (3.3) gives the per cycle dissipation within a single dissipation site inside a bulk solid in terms of a suitable quantity $A$. In the following sections, we will develop a definition of $A$ from the analysis of elasto-plastic inclusions under far-field time-periodic triaxial loads. We close this section with a brief preview of the statistical averaging over $s$ that we will use in Chapter 4.

In Eq. (3.3), if the strength $s$ is a random variable with probability density function $p(s)$, then the average dissipation can be computed as

$$\int_0^\infty E_d\, p(s)\, ds = \int_0^A E_d\, p(s)\, ds,$$

because for values of $s$ greater than $A$, yielding has not occurred and $E_d = 0$.

## 3.3 Elasto-plastic inclusion under far-field stresses

We consider elastic perfectly-plastic flaws embedded inside an elastic body under remotely applied stresses. We first study them using the finite element package ABAQUS, and then develop a semi-analytical method for the computation.

### 3.3.1 Finite element calculation

We consider ellipsoidal flaws embedded in an elastic material. Figure 3.3 shows a schematic of a flaw, the coordinate system used, and the remotely applied stresses. The elastic block is large, and the flaw behaves as if it is in an infinite solid.

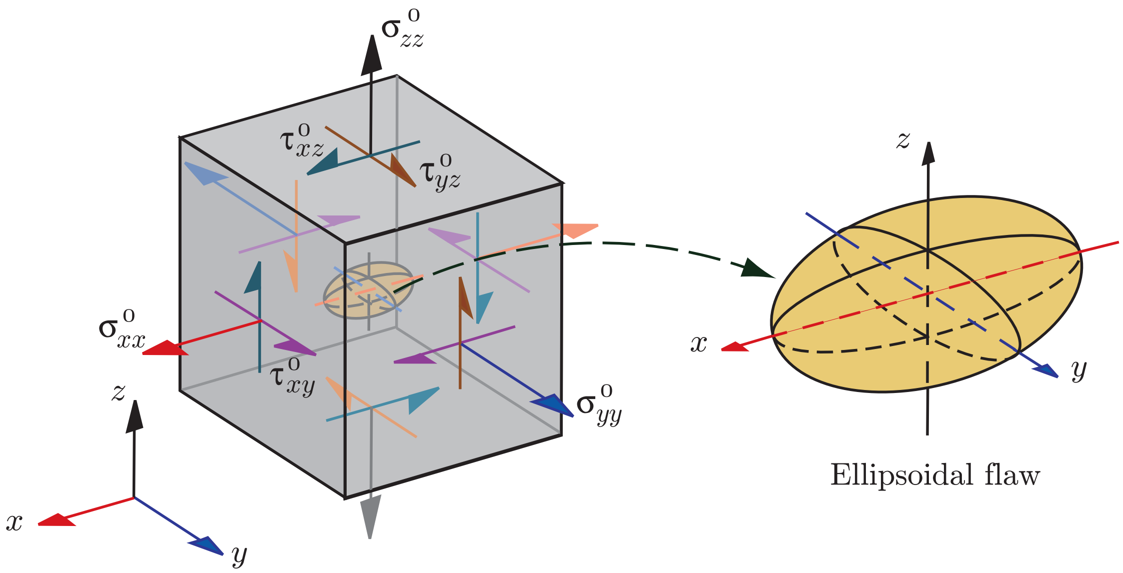

Figure 3.3: Ellipsoidal elasto-plastic flaw embedded in an elastic material with far-field stresses $\sigma_{ij}^{0}$. The ellipsoid is given by $\dfrac{x^2}{a_1^2} + \dfrac{y^2}{a_2^2} + \dfrac{z^2}{a_3^2} \leq 1$.

In our finite element simulations, we consider several flaw geometries and loading conditions. In each case, we carry out pseudostatic analysis in ABAQUS with incremental changes in the far-field loads as follows. We fix in advance a far-field triaxial stress state (say $\boldsymbol{\sigma}_0$) and the load is increased slowly up to that stress, in small increments from zero, using proportional loading. For example, suppose that 200 increments are used in the simulation. Then the load steps going from 1 to 200 are denoted using an artificial time that goes from 0 to 1, called the *normalized load step*. A normalized load step of 0.3 then corresponds to the 60th step, at which point the far-field load is $0.3 \times \boldsymbol{\sigma}_0$. This terminology will be used in presenting our results below.

#### 3.3.1.1 Modeling details for a typical ellipsoidal flaw

Details of one of our ABAQUS models are presented here. We have used 8-node linear brick elements (C3D8RH) to discretize the volume. This element uses reduced integration with hybrid, constant pressure, and hourglass control options (see ABAQUS analysis user manual (ABAQUS manual, 2009) for details). A cube of 20 mm edge length is considered with a central ellipsoidal flaw. A quarter of the mesh for an ellipsoidal flaw ($a_1 = 1\,\text{mm}$, $a_2 = 0.75\,\text{mm}$, and $a_3 = 0.5\,\text{mm}$) is shown in Fig. 3.4. A total of 82440 elements were used, with high refinement near the inclusion for better accuracy. Table 3.1 shows the material properties used for the parent and flaw materials in both this simulation and subsequent ones reported below. The flaw material is considered as elastic perfectly-plastic, and it fails when the von Mises stress within the material reaches a specified limit, $\sigma_{yp}$.

| Elastic parent material | |
|---|---|
| Young's modulus | 100 GPa |
| Poisson's ratio | 0.3 |
| **Elastic perfectly-plastic flaw material** | |
| Young's modulus | 50 GPa |
| Poisson's ratio | 0.28 |
| Yield strength ($\sigma_{yp}$) | 25 MPa |

Table 3.1: Material properties (chosen arbitrarily) used in all the analyses in this chapter.

#### 3.3.1.2 Finite element results

We have studied several cases, with different ellipsoid geometries as well as far-field loads. A typical example is for $a_1 = 1\,\text{mm}$, $a_2 = 0.75\,\text{mm}$, and $a_3 = 0.5\,\text{mm}$ under load case 1 of Table 3.2.

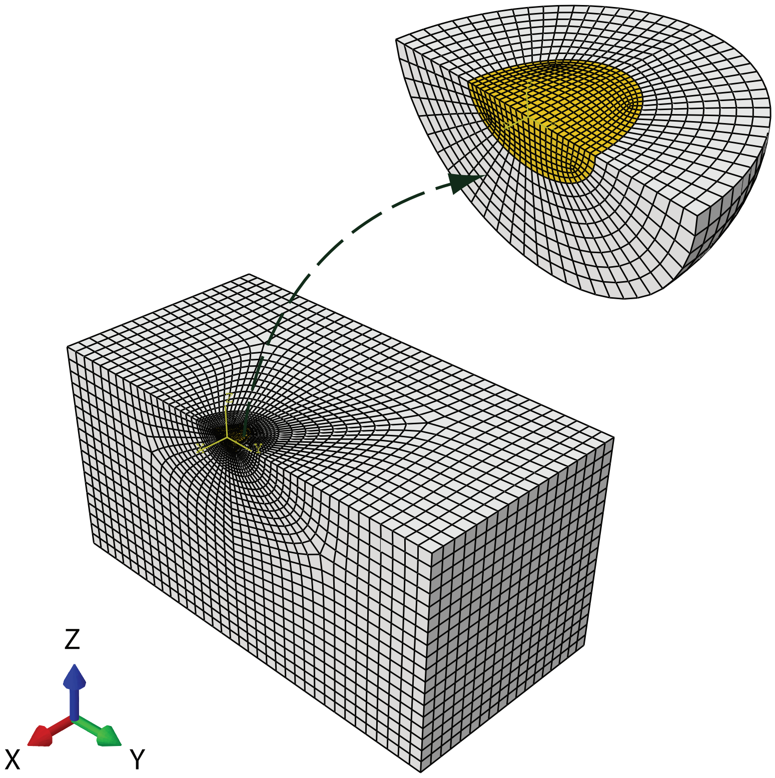

Figure 3.4: Finite element mesh of the 3D model (quarter portion). A small region around the ellipsoidal flaw ($a_1 = 1\,\text{mm}$, $a_2 = 0.75\,\text{mm}$, and $a_3 = 0.5\,\text{mm}$) is shown enlarged.

| | $\sigma^0_{xx}$ | $\sigma^0_{yy}$ | $\sigma^0_{zz}$ | $\tau^0_{yz}$ | $\tau^0_{zx}$ | $\tau^0_{xy}$ |
|---|---|---|---|---|---|---|
| load case 1 | 75 | −50 | 40 | 30 | −25 | 65 |
| load case 2 | −50 | −35 | 60 | −40 | 25 | 35 |
| load case 3 | −70 | 30 | −35 | −25 | 30 | 40 |

Table 3.2: Different far-field stresses (MPa) considered in various examples within this chapter.

The results show that the stress state within the ellipsoidal inclusion, both before and after yielding, remains essentially uniform. For example, the contour for von Mises stress and $\sigma_x$ at a normalized load step of 0.3 are shown in Figs. 3.5 and 3.6 respectively. The slight non-uniformity (less than 1.5%) seen in the $\sigma_x$ plot, predominantly near the edges of the inclusion, is an artifact of discretization: we will develop a semi-analytical formulation below based on exact uniformity within ellipsoidal flaws. Such uniformity was observed in several other simulations, including ellipsoids of varying aspect ratios.

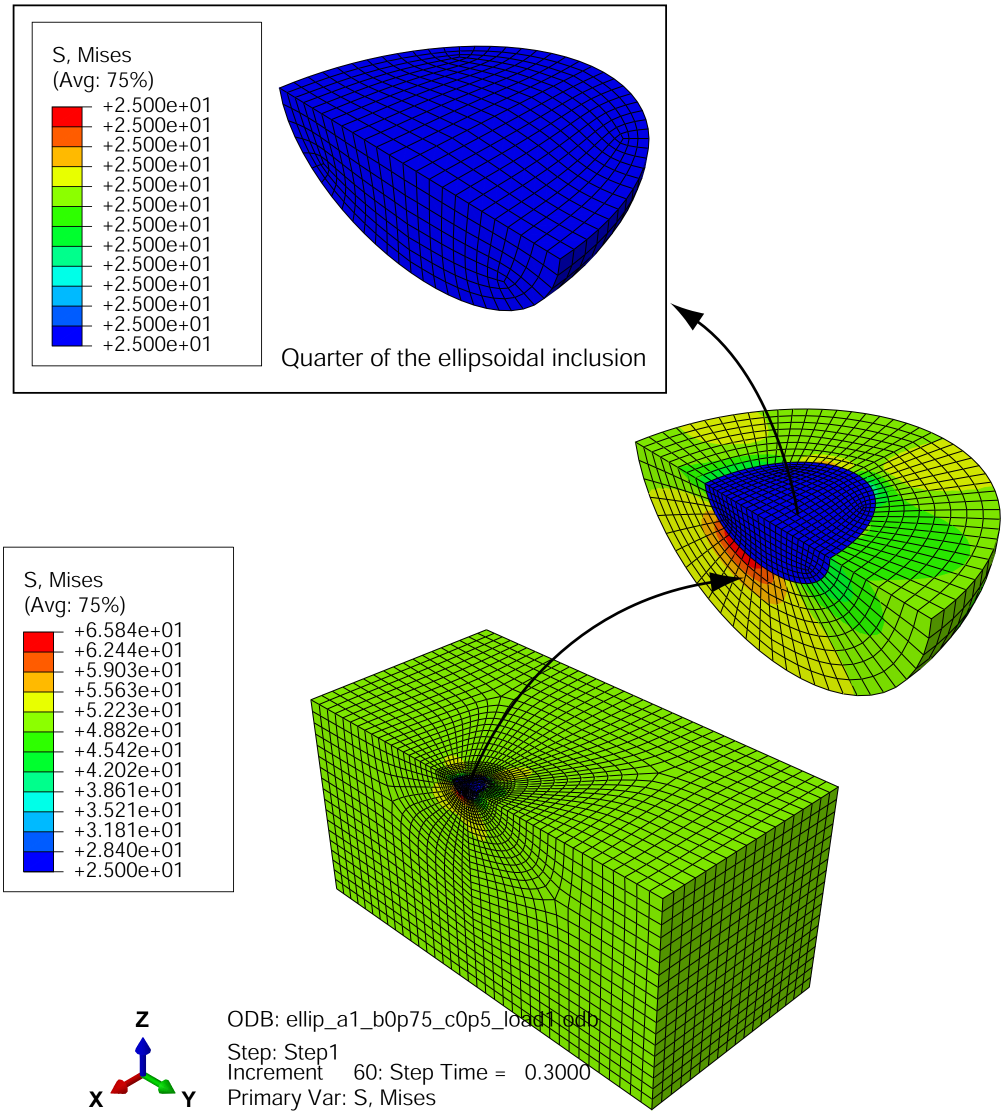
S, Mises
(Avg: 75%)
+2.500e+01
+2.500e+01
+2.500e+01
+2.500e+01
+2.500e+01
+2.500e+01
+2.500e+01
+2.500e+01
+2.500e+01
+2.500e+01
+2.500e+01
+2.500e+01
+2.500e+01
Quarter of the ellipsoidal inclusion
S, Mises
(Avg: 75%)
+6.584e+01
+6.244e+01
+5.903e+01
+5.563e+01
+5.223e+01
+4.882e+01
+4.542e+01
+4.202e+01
+3.861e+01
+3.521e+01
+3.181e+01
+2.840e+01
+2.500e+01
Z
X
Y
ODB: ellip_a1_b0p75_c0p5_load1.odb
Step: Step1
Increment 60: Step Time = 0.3000
Primary Var: S, Mises

Figure 3.5: Plot of von Mises stress in one quarter of the model at a normalized load step of 0.3. The stress plot within the inclusion is uniform. The geometry of the ellipsoid is $a_1 = 1$ mm, $a_2 = 0.75$ mm, and $a_3 = 0.5$ mm; and the far-field loads are of load case 1 of Table 3.2.

However, we also note that such uniformity of stresses within the flaw is not observed, when we consider non-ellipsoidal flaws. As an example, we have carried out similar analysis for a cylindrical flaw. The cylindrical flaw, modeled at the center of the 20 mm cube, is of radius 0.5 mm and length 1 mm. The far-field loads are of load case 1 of Table 3.2. A total of 68100 brick elements are used in the mesh. The inclusion is modeled with finer mesh density and tied (using tie constraints within

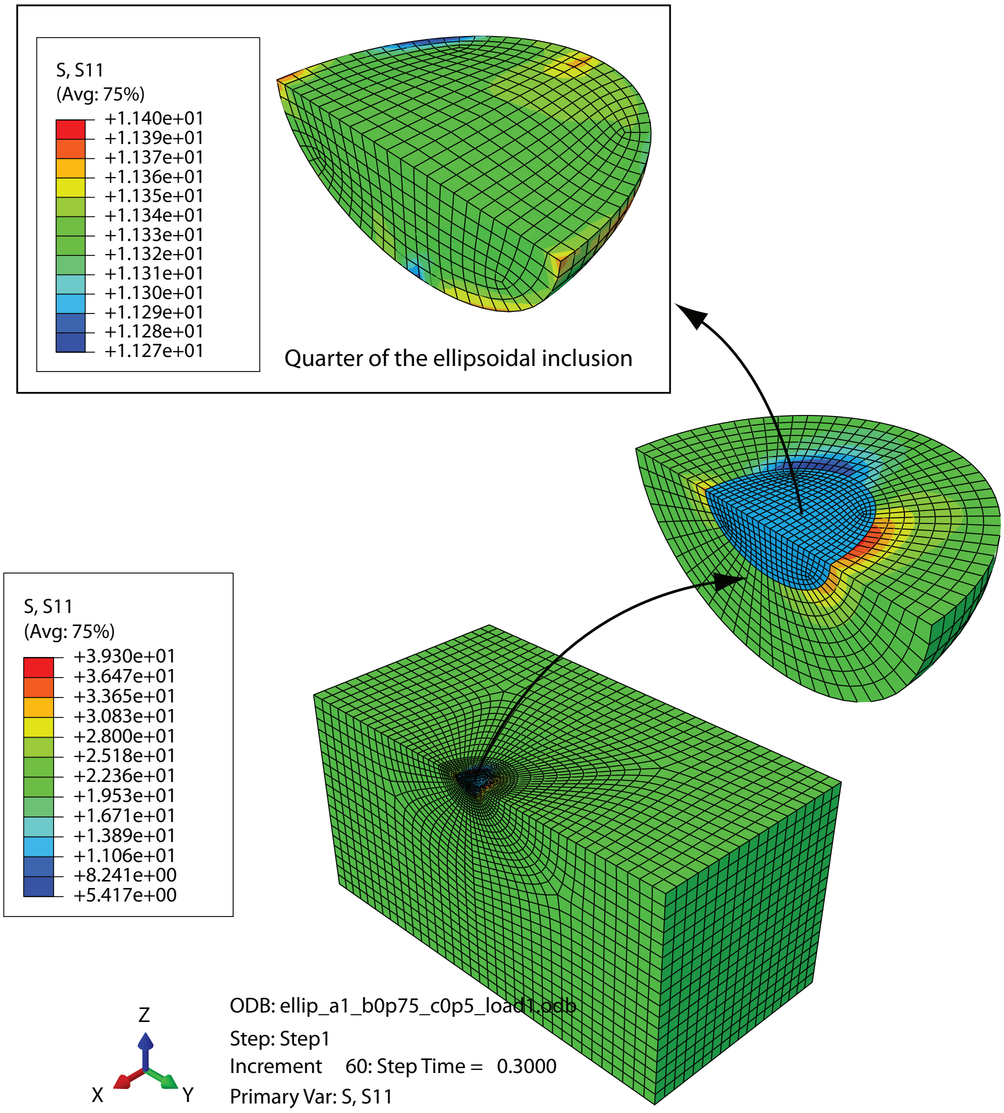
S, S11
(Avg: 75%)
+1.140e+01
+1.139e+01
+1.137e+01
+1.136e+01
+1.135e+01
+1.134e+01
+1.133e+01
+1.132e+01
+1.131e+01
+1.130e+01
+1.129e+01
+1.128e+01
+1.127e+01
Quarter of the ellipsoidal inclusion
S, S11
(Avg: 75%)
+3.930e+01
+3.647e+01
+3.365e+01
+3.083e+01
+2.800e+01
+2.518e+01
+2.236e+01
+1.953e+01
+1.671e+01
+1.389e+01
+1.106e+01
+8.241e+00
+5.417e+00
Z
X
Y
ODB: ellip_a1_b0p75_c0p5_load1.odb
Step: Step1
Increment 60: Step Time = 0.3000
Primary Var: S, S11

Figure 3.6: Plot of $\sigma_x$ in one quarter of the model at a normalized load step of 0.3. The variation of $\sigma_x$ within the inclusion is small. The geometry of the ellipsoid is $a_1 = 1\,\text{mm}$, $a_2 = 0.75\,\text{mm}$, and $a_3 = 0.5\,\text{mm}$; and the far-field loads are of load case 1 of Table 3.2.

ABAQUS) with the host part. The tie constraint option available in ABAQUS allows us to fuse together two regions even though the meshes created on the surfaces of the regions may be dissimilar (for details, see ABAQUS analysis user manual (ABAQUS manual, 2009)). The pseudostatic analysis for this model has been carried in 200 equal incremental steps. Figure 3.7 shows the $\sigma_x$ stresses at a normalized load step of 0.3. We see that the variation of $\sigma_x$ within the inclusion is non-uniform (variation over an order of magnitude). And this non-uniformity is seen for other stress components also.

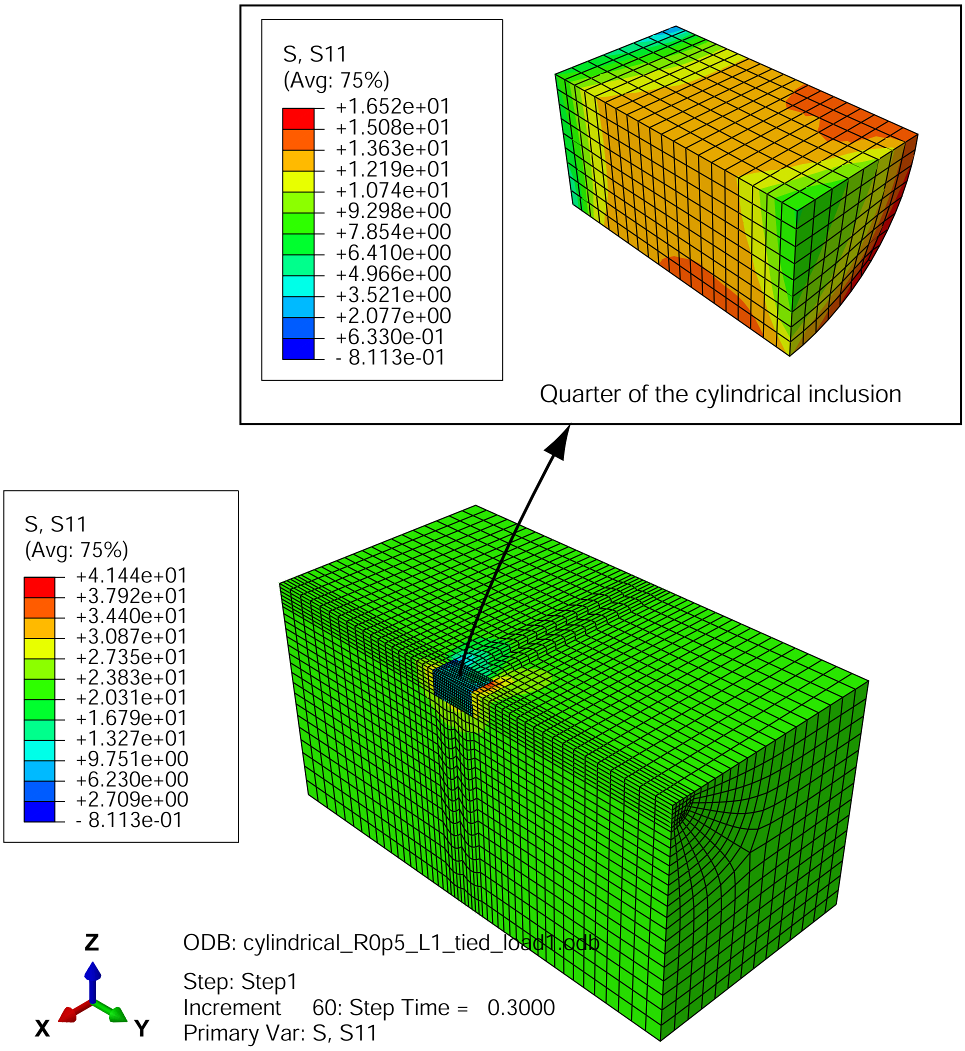
S, S11
(Avg: 75%)
+1.652e+01
+1.508e+01
+1.363e+01
+1.219e+01
+1.074e+01
+9.298e+00
+7.854e+00
+6.410e+00
+4.966e+00
+3.521e+00
+2.077e+00
+6.330e-01
- 8.113e-01
Quarter of the cylindrical inclusion
S, S11
(Avg: 75%)
+4.144e+01
+3.792e+01
+3.440e+01
+3.087e+01
+2.735e+01
+2.383e+01
+2.031e+01
+1.679e+01
+1.327e+01
+9.751e+00
+6.230e+00
+2.709e+00
- 8.113e-01
Z
X
Y
ODB: cylindrical_R0p5_L1_tied_load1.odb
Step: Step1
Increment 60: Step Time = 0.3000
Primary Var: S, S11

Figure 3.7: Plot of $\sigma_x$ at the normalized load step of 0.3 in the quarter portion of the model with a cylindrical flaw. The variation of $\sigma_x$ within the inclusion is seen non-uniform. The cylindrical flaw is of 0.5 mm radius and 1 mm length. The far-field load considered is load case 1 of Table 3.2.

We now go back to our original simulation of the ellipsoidal flaw. We choose an arbitrary element near the centroid of the flaw, and plot all six stress components against normalized load step in Fig. 3.8. It is seen that the stress state varies linearly until yield. Subsequently, there is a transition region beyond which the stresses approach a limiting state wherein the shear stresses remain constant while normal stresses vary linearly with far-field stress (i.e., the hydrostatic stress increases linearly). Such limiting behavior is seen in ellipsoids of other shapes as well (see Fig. 3.9).

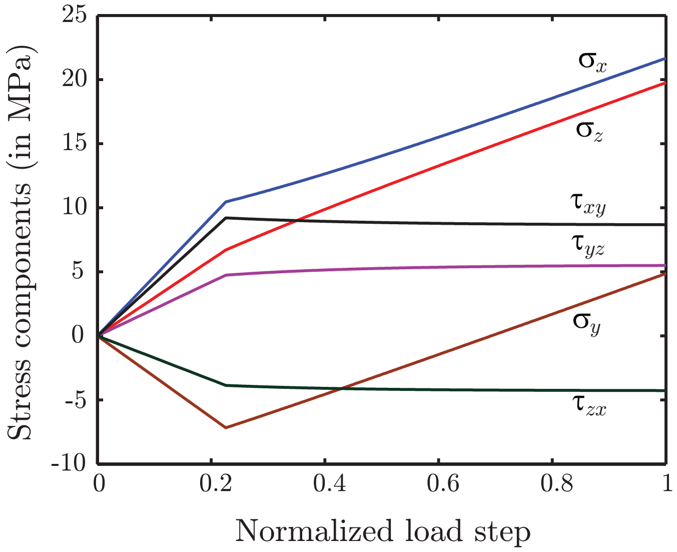

Figure 3.8: Stress components inside ellipsoidal elasto-plastic flaw. Here, $a_1 = 1\,\text{mm}$, $a_2 = 0.75\,\text{mm}$, and $a_3 = 0.5\,\text{mm}$ and the far-field stresses are of load case 1 in Table 3.2.

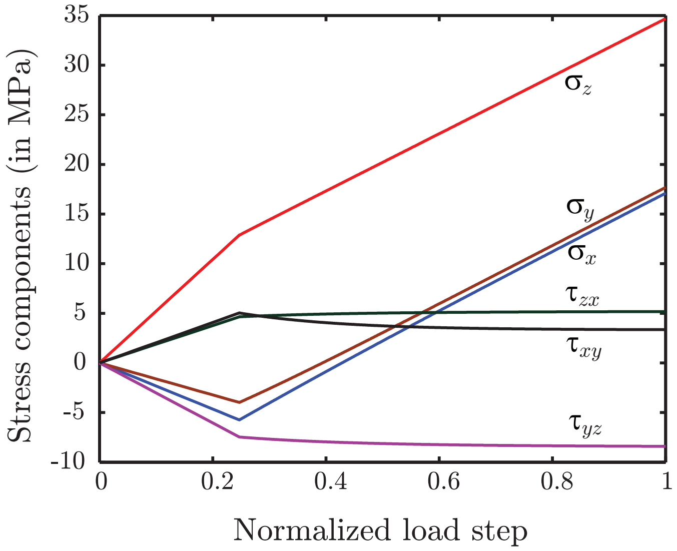

Figure 3.9: Stress components inside an ellipsoidal elasto-plastic flaw where $a_1 = 1\,\text{mm}$, $a_2 = 0.75\,\text{mm}$, and $a_3 = 0.25\,\text{mm}$ and the far-field stresses are of load case 2 in Table 3.2.

## 3.3.2 Semi-analytical approach

We now seek a semi-analytical formulation of the same problems based on classic formulas due to Eshelby (see Eshelby (1957) and Mura (1987)). A concise introduction to topics essential for us is now presented, based on the same sources.

### 3.3.2.1 Eshelby's formulas for an ellipsoidal inhomogeneous inclusion

We consider a homogeneous isotropic linearly elastic solid subjected to far-field stresses, and containing a small subdomain with 'eigenstrain.' The subdomain is called an *inclusion*, and eigenstrain here means 'stress-free strain' which the inclusion would exhibit if not constrained by the surrounding material. Non-elastic strains such as due to thermal expansion, phase transformation, plastic deformation, and misfits, can serve as eigenstrains. If the subdomain has different elastic moduli than the sourrounding material, then it is called an *inhomogeneous inclusion* (see Fig. 3.10).

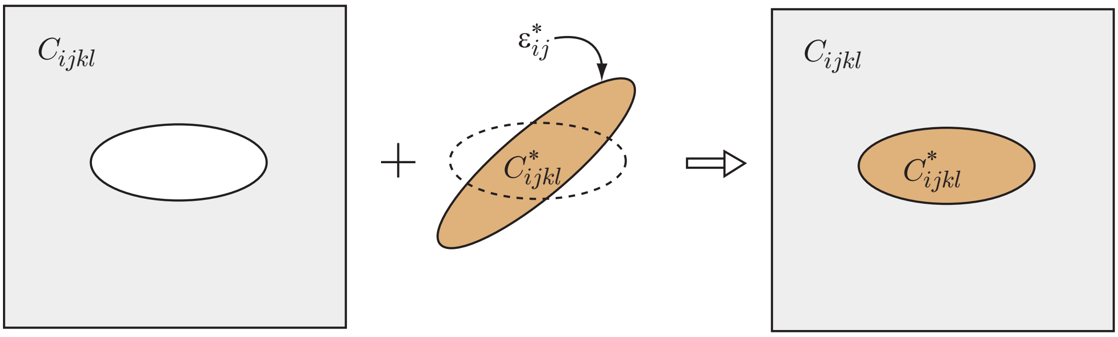

Figure 3.10: Inhomogeneous inclusion. The subdomain has different elastic moduli than the outer material and contains eigenstrain ($\varepsilon^*_{ij}$). The inclined shaded ellipse in the middle is intended to indicate that the inclusion cannot be fitted inside the cavity without causing additional strain in both the inclusion as well as the outer material. When the eigenstrain is zero the subdomain is called an *inhomogeneity*. When the subdomain has the same elastic moduli as the outer material it is called a *homogeneous inclusion* (or simply an *inclusion*).

Let the far-field stress be $\sigma^0_{ij}$, and let the eigenstrain be $\varepsilon^*_{ij}$. The far-field strain is $\varepsilon^0_{kl}$, satisfying $\sigma^0_{ij} = C_{ijkl}\varepsilon^0_{kl}$, where $C_{ijkl}$ is the elasticity tensor of the outer material; note that we are using the usual summation convention for repeated indices in this and the following several formulas.

The uniform stress state within the ellipsoidal inhomogeneous inclusion is then given by

$$\sigma_{ij} = C^*_{ijkl}(\varepsilon^0_{kl} + \varepsilon_{kl} - \varepsilon^*_{kl}), \tag{3.4}$$

where $C^*_{ijkl}$ is the elasticity tensor of the inclusion material, and the newly introduced strain $\varepsilon_{ij}$ is related to another (as yet undetermined) eigenstrain by

$$\varepsilon_{ij} = S_{ijkl}\varepsilon^{**}_{kl}. \tag{3.5}$$

Here, $S_{ijkl}$ is called the Eshelby tensor (see Appendix B.1 for relevant formulas), which depends only on the Poisson's ratio ($\nu$) of the outer material and on the shape of the ellipsoid ($a_1, a_2$, and $a_3$). The undetermined $\varepsilon^{**}_{kl}$ is obtained from the equivalence equation

$$C^*_{ijkl}(\varepsilon^0_{kl} + S_{klmn}\varepsilon^{**}_{mn} - \varepsilon^*_{kl}) = C_{ijkl}(\varepsilon^0_{kl} + S_{klmn}\varepsilon^{**}_{mn} - \varepsilon^{**}_{kl}). \tag{3.6}$$

The above three formulas can be directly obtained from Mura (1987) (with slight notational changes adopted for continuity and clarity). Note that Eq. (3.6) is linear in the unknown eigenstrain $\varepsilon^{**}_{kl}$, with everything else known. Substituting the result back into Eq. (3.5) and thence into Eq. (3.4), the stress state in the inclusion can be found.

#### 3.3.2.2 Approach for ellipsoidal elasto-plastic flaw

In our problem, the plastic strain in the ellipsoidal flaw is the eigenstrain; and it is not known in advance but must be found as a part of the solution. Since we will work with rate-independent incremental plasticity, we will use the rate form of Eqs. (3.4) and (3.6).

Adopting the well known Voigt notation, the stress rate is written as

$$\dot{\boldsymbol{\sigma}} = \mathbf{C}^*(\dot{\boldsymbol{\varepsilon}}^0 + \mathbf{S}\dot{\boldsymbol{\varepsilon}}^{**} - \dot{\boldsymbol{\varepsilon}}^p). \tag{3.7}$$

The Voigt notation is routinely used in solid mechanics computations (see Khan and

Huang (1995)). In the above equation $\dot{\boldsymbol{\sigma}}$, $\dot{\boldsymbol{\varepsilon}}^0$, $\dot{\boldsymbol{\varepsilon}}^p$, and $\dot{\boldsymbol{\varepsilon}}^{**}$ are $6 \times 1$ column matrices[1], while $\mathbf{C}^*$ and $\mathbf{S}$ are $6 \times 6$ matrices. The corresponding rate form of the equivalence equation is

$$\mathbf{C}^*(\dot{\boldsymbol{\varepsilon}}^0 + \mathbf{S}\dot{\boldsymbol{\varepsilon}}^{**} - \dot{\boldsymbol{\varepsilon}}^p) = \mathbf{C}(\dot{\boldsymbol{\varepsilon}}^0 + \mathbf{S}\dot{\boldsymbol{\varepsilon}}^{**} - \dot{\boldsymbol{\varepsilon}}^{**}). \tag{3.8}$$

Note in Eqs. (3.7) and (3.8) that we have used a different symbol ($\dot{\boldsymbol{\varepsilon}}^p$) for the eigenstrain rate as it corresponds to the plastic strain in our case.

Solving Eq. (3.8) for $\dot{\boldsymbol{\varepsilon}}^{**}$ and substituting in Eq. (3.7), we obtain

$$\dot{\boldsymbol{\sigma}} = \mathbf{G}\dot{\boldsymbol{\varepsilon}}^0 + \mathbf{H}\dot{\boldsymbol{\varepsilon}}^p, \tag{3.9}$$

where $\mathbf{G}$ and $\mathbf{H}$ are $6 \times 6$ matrices given in Appendix B.2.

Equation (3.9) can be used during both purely elastic and elasto-plastic deformations. When the material behaves elastically (initial loading, during unloading, etc.) the plastic strain rate $\dot{\boldsymbol{\varepsilon}}^p$ is zero. In this elastic state, the stress state inside the ellipsoidal region varies linearly with the far-field stress until the inclusion stress reaches its yield envelope. The yield envelope in the present case is based on the von Mises yield criterion,

$$f = \frac{1}{2}\boldsymbol{\sigma}_d^{\intercal}\mathbf{Q}\boldsymbol{\sigma}_d - \frac{1}{3}\sigma_{yp}^2 = 0, \tag{3.10}$$

where $\boldsymbol{\sigma}_d$ is the deviatoric stress tensor written in a $6 \times 1$ column matrix, $\mathbf{Q}$ is the $6 \times 6$ diagonal matrix with diagonal elements $\{1, 1, 1, 2, 2, 2\}$, and $\sigma_{yp}$ is the specified yield strength. Further loading after reaching the yield envelope will generate plastic strains. The rate of these plastic strain components is normal to the yield envelope. Therefore, we write

$$\dot{\boldsymbol{\varepsilon}}^p = \lambda \frac{\partial f}{\partial \boldsymbol{\sigma}_d} \tag{3.11}$$

for some $\lambda$, and note that

$$\frac{\partial f}{\partial \boldsymbol{\sigma}_d} = \mathbf{Q}\boldsymbol{\sigma}_d.$$

Since the stress state remains on the yield surface, the normality condition also implies

---

[1] The components are arranged in the sequence $\{(\ )_{11}, (\ )_{22}, (\ )_{33}, (\ )_{23}, (\ )_{13}, (\ )_{12}\}$.

$$\dot{\boldsymbol{\sigma}}^{\mathsf{T}} \dot{\boldsymbol{\varepsilon}}^{p} = 0. \tag{3.12}$$

With the above equations, we start an analysis of monotonic loading. In the beginning the material is elastic. The stresses within the inclusion increase linearly as per Eq. (3.9) with $\dot{\boldsymbol{\varepsilon}}^{p} = 0$, and we keep checking for yielding using Eq. (3.10). Once yielding occurs, i.e., in the plastic domain, we use Eqs. (3.9), (3.11) and (3.12) simultaneously to solve for $\dot{\boldsymbol{\sigma}}$, $\dot{\boldsymbol{\varepsilon}}^{p}$ and $\lambda$ (note that the equations are linear in these unknowns). We then have 13 equations (six from Eq. (3.9), six from Eq. (3.11) and one from Eq. (3.12)) and 13 unknowns (six in $\dot{\boldsymbol{\sigma}}$, six in $\dot{\boldsymbol{\varepsilon}}^{p}$ and one in $\lambda$). Dropping the $\lambda$ and using the rate variables, we integrate a system of ordinary differential equations using Matlab's "`ode45`".

#### 3.3.2.3 Comparison with finite element results

Stresses computed using the above semi-analytical method match finite element results very well. The stress plots shown earlier in both Figs. 3.8 and 3.9, actually contain two sets of visually indistinguishable superposed graphs, one from ABAQUS and another from the semi-analytical calculation. Referring to the earlier numerical observation of constancy of stress within the ellipsoidal inclusion (section 3.3.1.2), it is satisfactory that the semi-analytical treatment explicitly obtains a solution based on the same constancy of stress. The match between the two sets of solutions (ABAQUS and semi-analytical) validates both of them. Subsequently, when we consider some extremely thin ellipsoids, the semi-analytical approach will remain viable while ABAQUS would require unfeasibly high mesh refinement.

#### 3.3.2.4 Extension to cyclic loading

The triangular wave form shown in Fig. 3.11 corresponds to a cyclic loading case (three load cycles are shown). The vertical axis shown in the figure represents a multiplying factor $k$. If $\boldsymbol{\sigma}^0$ is the maximum stress then $k\boldsymbol{\sigma}^0$ will be the pseudostatically applied stress, as shown in the figure. For illustration, see Fig. 3.12, which depicts $k\sigma^0_{xx}$ with $\sigma^0_{xx} = 75$ MPa in $\boldsymbol{\sigma}^0$. In these figures the horizontal axis, called 'normalized time steps of loading', go from 0 to 1 and actually represent 1200 incremental steps in ABAQUS.

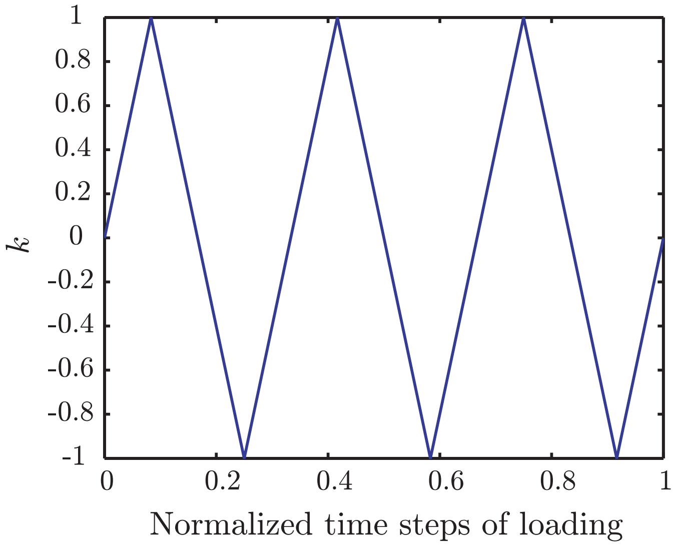

Figure 3.11: Triangular wave form used for the far-field stresses in the cyclic loading case (three load cycles)

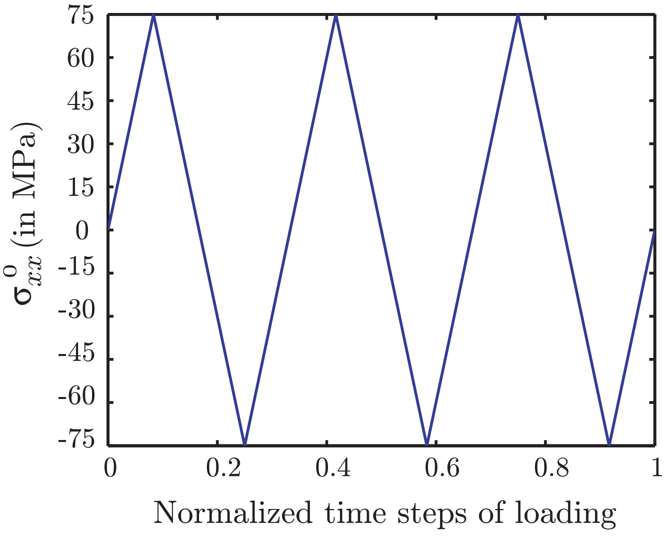

Figure 3.12: Variation of $\sigma^0_{xx}$ component in load case 1 of Table 3.2.

When we solve the ODEs within Eqs. (3.9), (3.11) and (3.12) in our semi-analytical approach, we use these same normalized time steps of loading as an artificial time governing a series of pseudostatic increments. For the cyclic loading case, we know that the start of unloading or reloading (i.e., the point of load direction reversal) begins a phase of purely elastic deformation. Subsequently, yield is detected by an in-built event detection feature of `ode45` in MATLAB (the “event” is satisfaction of Eq. (3.10)). Once yield is detected, the starting elastic and plastic state are known, and Eqs. (3.9), (3.11) and (3.12) (see section 3.3.2.2 above) are used to compute the evolution of the stress and strain state.

Figure 3.13 (a) compares the stress components obtained from ABAQUS and the semi-analytical method, for an ellipsoid of $a_1 = 1\,\mathrm{mm}$, $a_2 = 0.75\,\mathrm{mm}$, and $a_3 = 0.5\,\mathrm{mm}$, and $\boldsymbol{\sigma}^0$ as in load case 1 of Table 3.2. Each curve seen actually consists of two visually indistinguishable curves as above, and there is almost perfect agreement between the ABAQUS and semi-analytical results.

Figure 3.13 (b) compares the computed plastic energy dissipation ($W_d$), computed using

$$\dot{W}_d = \boldsymbol{\sigma}^\intercal \dot{\boldsymbol{\varepsilon}}^p V, \tag{3.13}$$

where $V$ is the volume of the ellipsoid. Agreement is excellent. Henceforth in this chapter, we will only use our semi-analytical method for analyses of elasto-plastic flaws: these calculations are much quicker, demonstrated to be correct, and less troubled by extreme shapes like very thin and flat ellipsoids.

## 3.4 Two special cases

### 3.4.1 Spherical inclusions

See the stress plot in Fig. 3.9 for an arbitrarily chosen ellipsoid under monotonic loading. At a normalized load step of approximately 0.24, yielding begins. The asymptotic behavior is approximately established by a normalized load step of about 0.6. In other words, there is a nonzero period of transition from initial yield to limiting state.

In contrast, for a spherical flaw[2], the establishment of the asymptotic behavior

---

[2] We note that Mura (1987) gives other formulas for the Eshelby tensor with $a_1 = a_2 = a_3$, but we use the formula for $a_1 > a_2 > a_3$ (Appendix B.1) after numerically perturbing the three values very slightly, e.g. 1.0001, 1.0, and 0.9999.

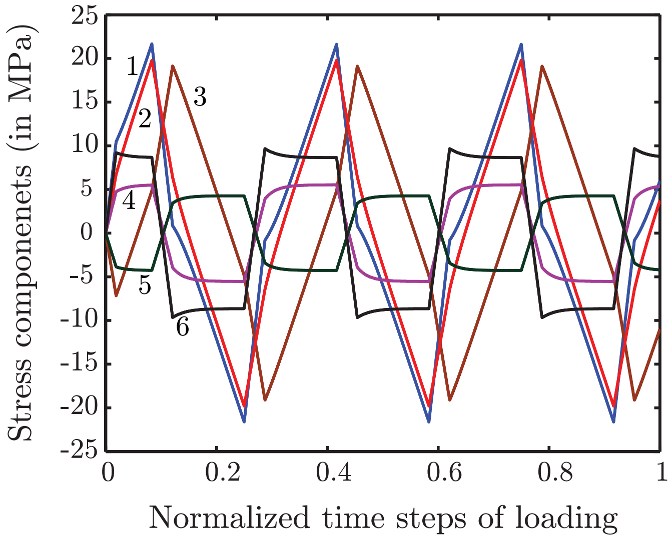

(a)

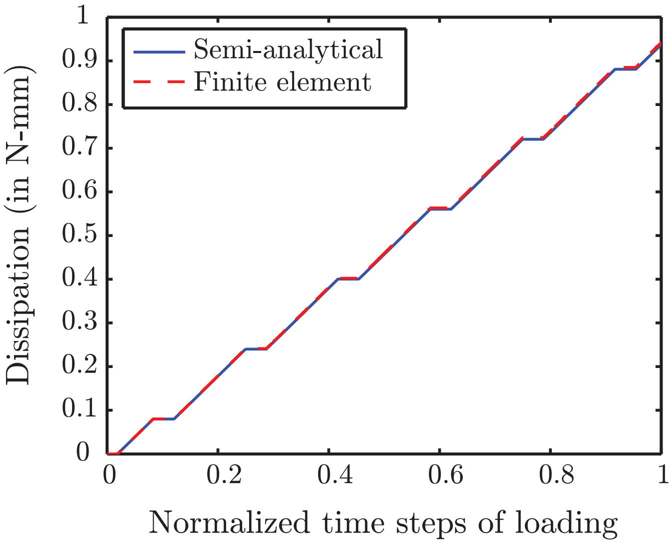

(b)

Figure 3.13: Results for cyclic loading. (a) Stress components inside the ellipsoidal region for ellipsoid of $a_1 = 1\,\text{mm}$, $a_2 = 0.75\,\text{mm}$, and $a_3 = 0.5\,\text{mm}$ under maximum far-field load of load case 1 of Table 3.2. The numbers correspond to: 1-$\sigma_x$, 2-$\sigma_z$, 3-$\sigma_y$, 4-$\tau_{xy}$, 5-$\tau_{yz}$ and 6-$\tau_{zx}$. (b) Comparison of the plastic dissipation in this loading case.

is instantaneous: see the stress plots in Fig. 3.14 for a spherical flaw of 1 mm radius. Additionally, in this case, the plastic dissipation can be determined by $J_2$ (the second invariant of the deviatoric stress) alone. This dependence purely on $J_2$ can be confirmed using a series of simulations as follows.

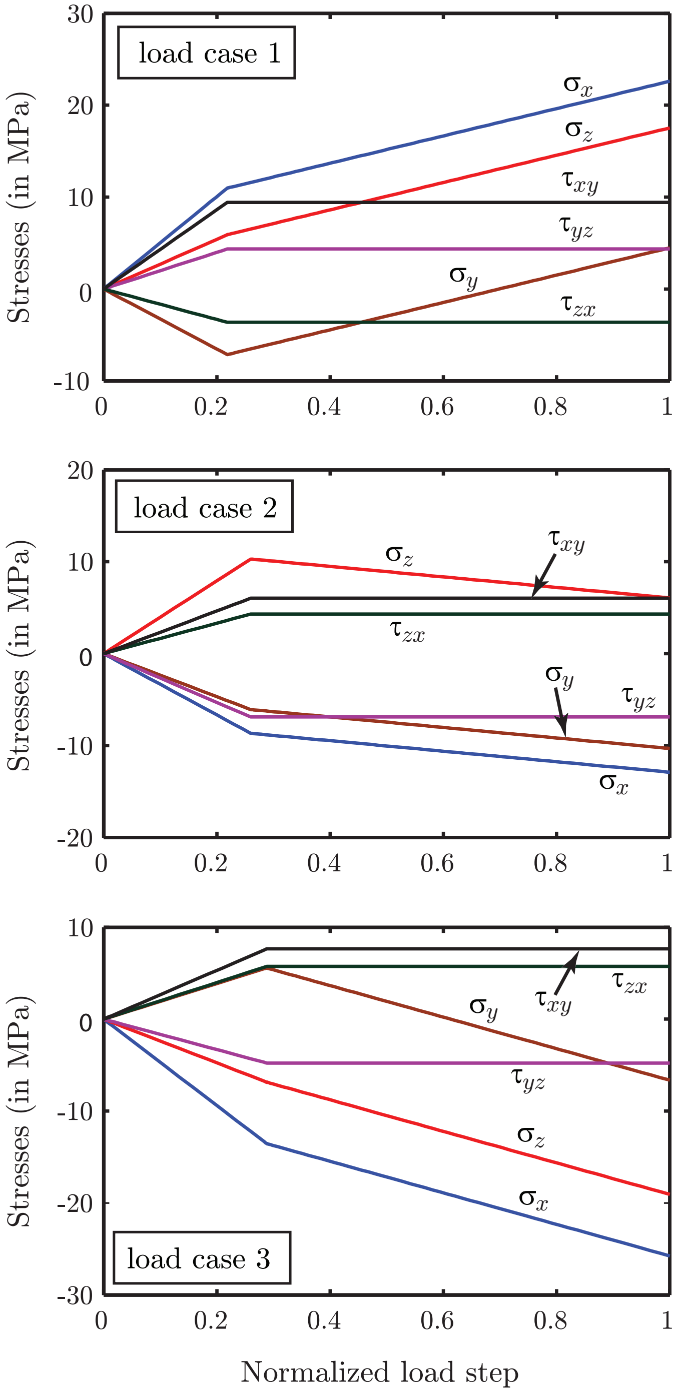

Figure 3.14: Stress state in a spherical ($r = 1\,\text{mm}$) inclusion, for the three load cases of Table 3.2.

Consider the same spherical flaw and the three loading cases of Table 3.2. For each of these loading cases, the following simulations are done. Cyclic loading is applied with a far-field stress of $k_c\boldsymbol{\sigma}^0$, where $\boldsymbol{\sigma}^0$ represents the loading case and $k_c$ goes from 0.01 to 1 in 50 steps (i.e., there are 50 different simulations of cyclic loading). For each such simulation of cyclic loading, the per-cycle dissipation is computed (actually, steady state is reached after the first cycle, and so the dissipation can be computed over any subsequent cycle). For each such simulation there is a $J_2$ corresponding to the maximum load applied: call it $J_{2,m}$. Subsequently, the dissipation per cycle is plotted against that $J_{2,m}$. Since, there are three load cases, there are three such curves. The key point here is that these three curves coincide perfectly (see Fig. 3.15). Hence, if we have an elastic perfectly-plastic *spherical* flaw under time-harmonic, far field, arbitrary stresses, then the dissipation per cycle is purely a function of $J_{2,m}$, i.e., $J_2$ at the maximum stress amplitude. In terms of section 3.2, $A = \sqrt{J_2}$ is an acceptable choice if the inclusion is spherical.

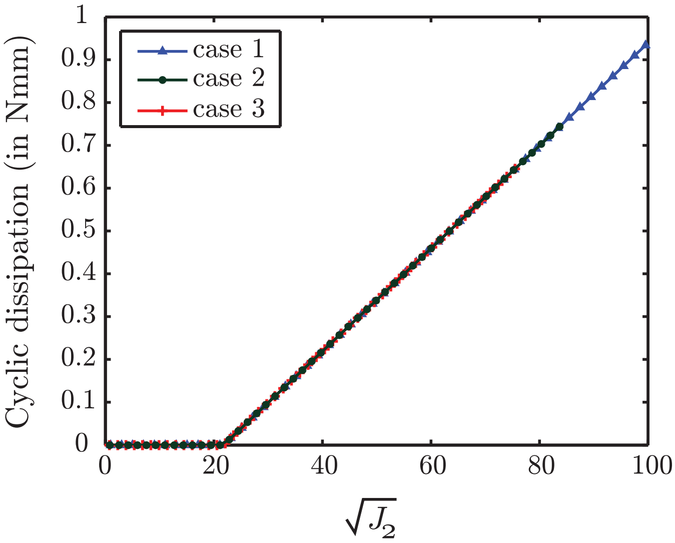

Figure 3.15: Cyclic dissipation against $\sqrt{J_2}$ for three different load cases of Table 3.2 for a spherical inclusion ($r = 1\,\text{mm}$).

The same (i.e., $A = \sqrt{J_2}$) cannot be used for a general ellipsoid, however. For example, with $a_1 = 1\,\text{mm}$, $a_2 = 0.75\,\text{mm}$, and $a_3 = 0.25\,\text{mm}$ and the same load cases, and the same set of simulations as described above for spherical flaws, the three dissipation curves obtained are given in Fig. 3.16.

The search for a suitable definition of $A$, for general ellipsoidal flaws, seems

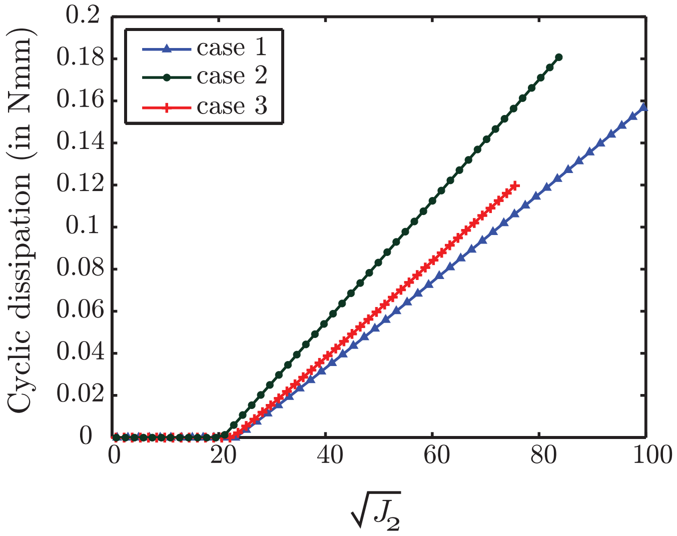

Figure 3.16: Cyclic dissipation against $\sqrt{J_2}$ for three different load cases of Table 3.2 for an ellipsoidal inclusion ($a_1 = 1\,\mathrm{mm}$, $a_2 = 0.75\,\mathrm{mm}$, and $a_3 = 0.25\,\mathrm{mm}$).

difficult. We now turn to another simple special case, namely thin and flat flaws.

### 3.4.2 Flat and thin ellipsoidal flaws

Consider a flat and thin ellipsoid ($a_1 = 1\,\mathrm{mm}$, $a_2 = 0.75\,\mathrm{mm}$, and $a_3 = 0.001\,\mathrm{mm}$) and the same three load cases of Table 3.2. Since the ellipsoid is thin, with its small-thickness direction aligned with the $z$-axis, we will think of the $x$-$y$ plane as being parallel to the flat face of the ellipsoid (although in reality the corresponding surface of the ellipsoid is very slightly curved). For this ellipsoid, the stresses for monotonic loading up to the maximum load in each case are plotted in Fig. 3.17. We see a distinct region of transient behavior before the stresses reach their limiting behaviors. Interestingly, the shear component $\tau_{xy}$ asymptotically goes to zero and the normal stresses collapse onto a single line (in fact, the limiting normal stress is the same as the far field value of $\sigma_z$). It follows that the limiting state is one of simple shear on the flat face, superimposed on a linearly increasing hydrostatic stress. The shear on the flat face must therefore equal the yield stress in simple shear. This last point is interesting because *initial* yield generally occurs when $\tau_{xy}$ is not zero, and the shear on the flat face has not reached its maximal value. Nevertheless, after a transient, the limiting behavior shows that *all* the shearing is effectively on the flat face.

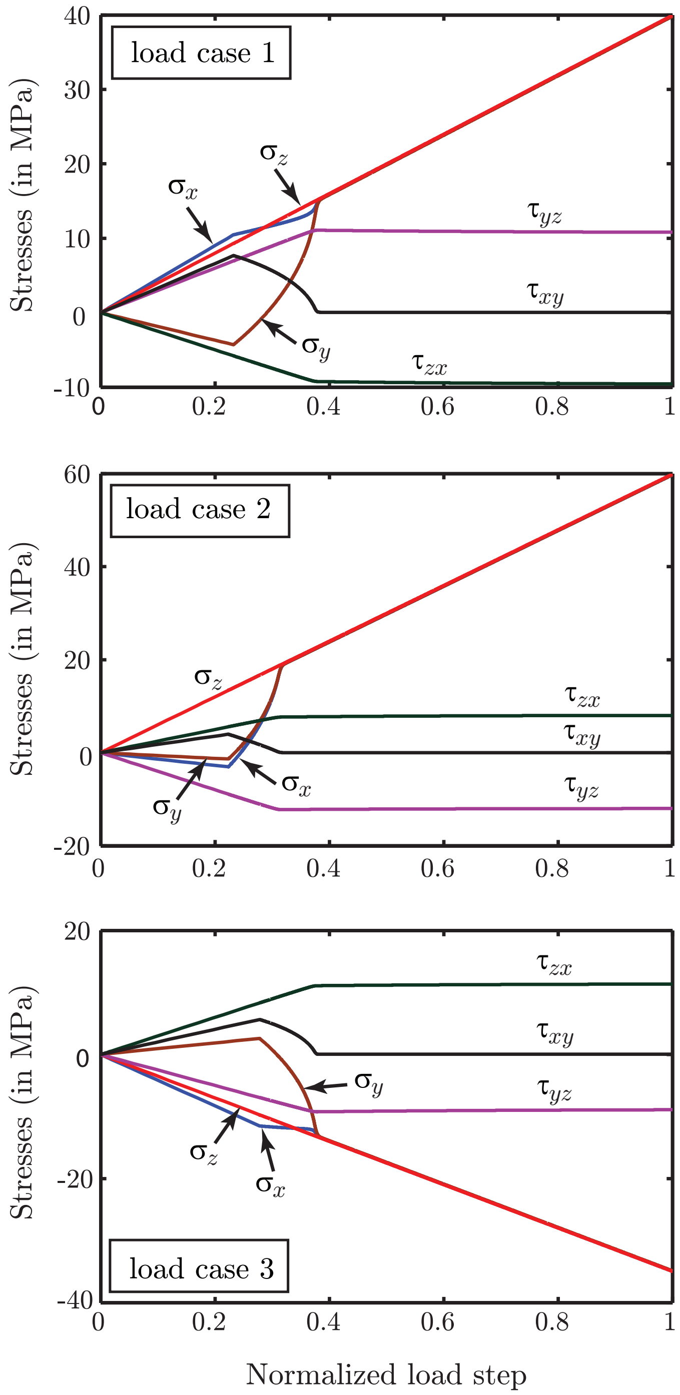

Figure 3.17: Stress state for a flat and thin ellipsoidal flaw ($a_1 = 1\,\text{mm}$, $a_2 = 0.75\,\text{mm}$, and $a_3 = 0.001\,\text{mm}$) in three load cases of Table 3.2.

We now conduct the same set of cyclic energy dissipation calculations for various amplitudes of loading, as done above for the spherical inclusion with three load cases, and generate three corresponding dissipation curves for the thin and flat ellipsoid. Results are given in Fig. 3.18. Figure 3.18 (a) shows that, similar to the case of a general ellipsoid, $\sqrt{J_2}$ is not an appropriate choice for $A$, in that the cyclic energy dissipation for arbitrary triaxial far-field time-harmonic loading is *not* simply a function of the maximal value of $J_2$ achieved in the loading cycle (the three curves do not collapse into one).

However, somewhat remarkably, Fig. 3.18 (b) shows that for thin and flat flaws, $A$ can be taken as the maximal value of the far-field "resolved" shear stress on a plane parallel to the flat face of the ellipsoid, which is

$$\tau = \sqrt{(\tau^0_{yz})^2 + (\tau^0_{zx})^2}. \tag{3.14}$$

The emergence of a clear and simple equivalent loading parameter $A$ for thin and flat elasto-plastic flaws is, in our opinion, noteworthy. There are two things to consider.

First, that the limiting state is simple shear on the flat face, superposed on a hydrostatic stress, is in retrospect not surprising. This is because, if the flaw is flat and thin, then even moderate separation between the near parallel faces causes a very large volumetric strain. Since such a strain is ruled out, the relative motion between the near-parallel faces must be near-parallel also. As a result, the dominant deformation is in simple shear. The plasticity constitutive relation then forces the shear traction to align with this deformation. Finally, again to avoid a large volumetric strain, the normal traction on the flat face of the ellipsoid (think of it as a crack face) must equal the far field $\sigma_z$, which is as observed above.

The second and more surprising thing, at least to us, is that the long and significant transient plays essentially no role in Fig. 3.18 (b), which shows a fairly sharp corner. We could not rationalize this with our intuition, even in hindsight; and it is this sharp corner that allows the thin and flat flaw to be counted within the same framework as introduced with a unidimensional model in section 3.2.

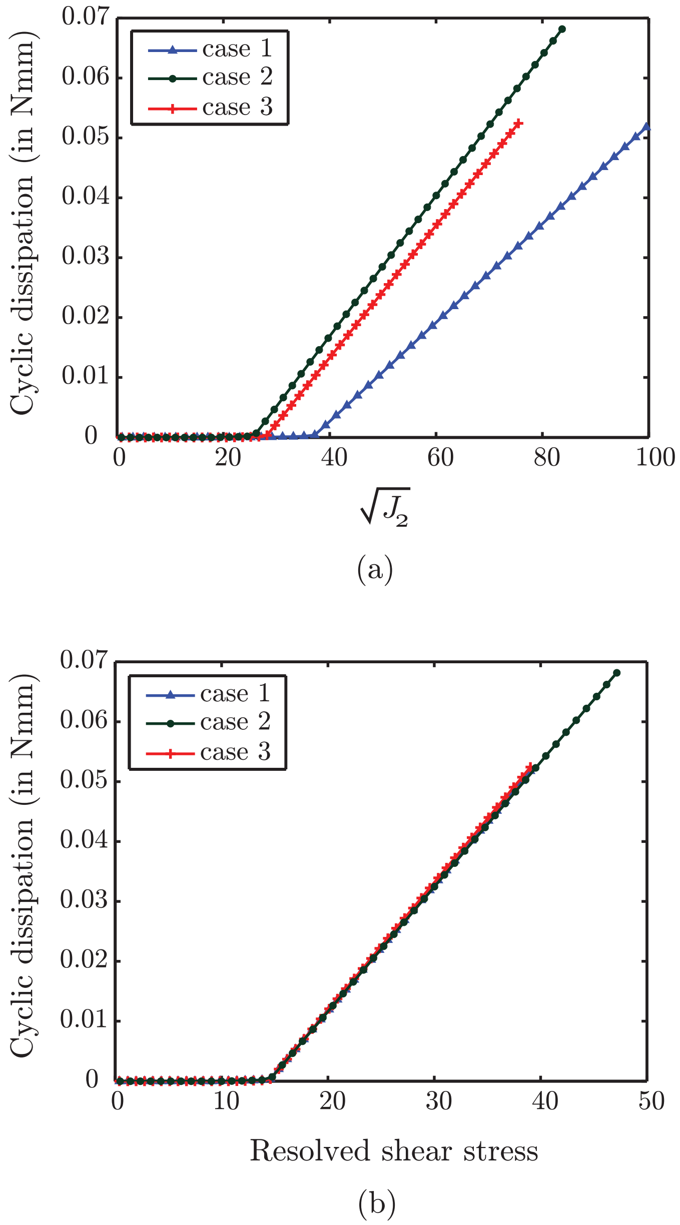

Figure 3.18: Variation of cyclic dissipation with respect to (a) $\sqrt{J_2}$ and (b) the resolved shear stress ($\tau$ of Eq. (3.14)), for three different load cases of Table 3.2 for a flat and thin ellipsoidal flaw ($a_1 = 1\,\text{mm}$, $a_2 = 0.75\,\text{mm}$, and $a_3 = 0.001\,\text{mm}$).

## 3.5 Summary

In this chapter, we have considered energy dissipation within elastic perfectly-plastic flaws. Specifically, we have considered flaws of ellipsoidal shape. Finite element simulation in ABAQUS showed that the stress state within an ellipsoidal flaw remains uniform under remotely applied loads, and past yield it approaches a limiting state.

The finite element results have been verified with a semi-analytical calculation based on Eshelby's (1957) formulas. The semi-analytical method has been extended to cyclic loading. We showed that both stresses within the inclusion and the cyclic energy dissipation computed using our semi-analytical method matches to an excellent accuracy, the finite element simulation results.

Finally, we have identified two simple limiting special cases where a plot of energy dissipated per cycle against some suitable scalar amplitude $A$ resembles Fig. 3.2(c). We have found that for spherical flaws, $A$ can be taken as $\sqrt{J_2}$. Additionally, for thin and flat flaws, it has been found that $A$ can be taken as the resolved shear stress

$$\tau = \sqrt{(\tau^0_{yz})^2 + (\tau^0_{zx})^2}.$$

In the next chapter, we will consider these two limiting cases for developing macroscopic dissipation models.

# Chapter 4

# Macroscopic dissipation due to dispersed elasto-plastic flaws

## 4.1 Introduction

In the last chapter, we have discussed dissipation due to a single microscopic plastic flaw. In this chapter, we will average over a multitude of randomly dispersed flaws of randomly distributed strengths, to obtain overall macroscopic dissipation formulas.

We assume that the dissipation from a single flaw is represented by an equivalent unidimensional model as in Eq. (3.3). As seen in section 3.4, the definition of $A$ depends on the flaw geometry. So we will continue with the same two limiting special cases here: spherical flaws, and flat and thin flaws.

For spherical flaws, $A$ is $\sqrt{J_2}$. For flat and thin flaws, $A$ is the resolved shear stress on the flat surface of the flaw (the flaw surface is *nearly* flat because it is thin, but we say just "flat" for brevity).

The averaging approaches for these two cases are different. For example, the orientation of the flaw plays a role for flat flaws, but for spherical flaws it does not. We treat these cases separately, first considering the simpler case of spherical flaws. For both cases, we assume that the flaws are small and far apart, so that their interaction can be neglected.

## 4.2 Spherical flaws

By Eq. (3.3), the energy dissipation due to a single spherical flaw is taken as

$$E_d = ks\left(\sqrt{J_2} - s\right) \quad \text{if } \sqrt{J_2} > s, \quad \text{and 0 otherwise,}$$

where $J_2$ is the second invariant of the deviatoric stress at the maximum loading point within the load cycle; and where $s > 0$ is the strength of the flaw and $k$ depends on the size of the flaw. For simplicity, we assume that $k$ and $s$ are independent, and we can independently average over these variables.

For $s$, we consider the Weibull distribution (see Soong (2004) and Johnson *et. al.* (1994)), which finds application in modeling random strengths of specimens, as well as other quantities. The probability density function (pdf) for the Weibull distribution is

$$p(s) = \frac{c}{a}\left(\frac{s}{a}\right)^{c-1} e^{-(s/a)^c}, \qquad \text{with } c > 0, a > 0, s > 0,$$

and is shown in Fig. 4.1 for a few pairs of parameter values. If $s$ is small (in the

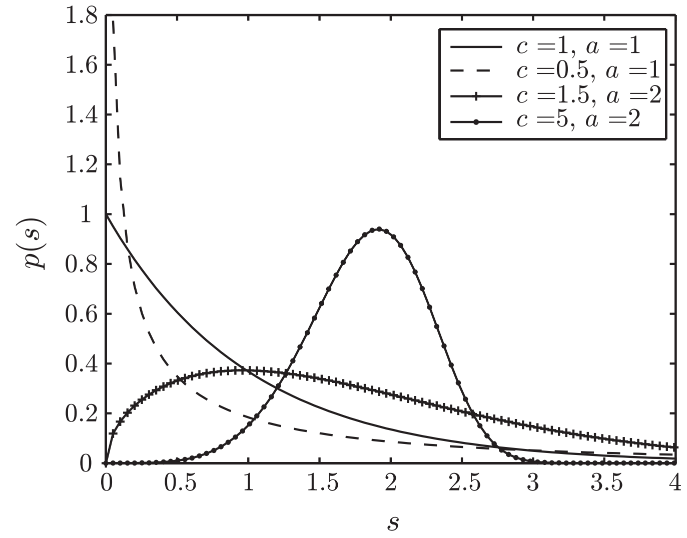

Figure 4.1: The Weibull distribution plotted for some choices of parameter values.

small amplitude regime) the exponential term $e^{-(s/a)^c}$ is close to 1 and we use

$$p(s) \approx Hs^q \quad \text{with } q > -1,\ H > 0. \tag{4.1}$$

Similar power law behavior for small $s$ is also observed in the Gamma and Beta distributions (see Soong (2004)), and any such distribution would serve our purposes: our appeal to the Weibull is, to this extent, notional. The special case of $c = 1$ above would give the commonly used exponential distribution.

Averaging the individual dissipation values over all strengths $s$ gives

$$D_{\mathrm{sf}} = \int_0^{\sqrt{J_2}} E_d p(s)\,\mathrm{d}s = Hk \int_0^{\sqrt{J_2}} s(\sqrt{J_2} - s)s^q\,\mathrm{d}s, \tag{4.2}$$

where the subscript "sf" denotes spherical flaws, and where the upper limit of the integration is $\sqrt{J_2}$, where $J_2$ is the second invariant of the deviatoric stress at the maximum loading point within the load cycle. The upper limit is $\sqrt{J_2}$ because flaws with greater strength have not yielded (recall the closing comment of section 3.2).

The integral of Eq. (4.2) works out to

$$D_{\mathrm{sf}} = \left(\frac{Hk}{q^2 + 5q + 6}\right)(\sqrt{J_2})^{3+q} = \bar{\xi} J_2^{m/2}, \tag{4.3}$$

where $\bar{\xi}$ contains $k$ and can be independently averaged over $k$, yielding some constant (to be fitted experimentally); and where $q > -1$ implies $m > 2$. In experimental settings, $m$ close to 2 might be indistinguishable from 2. Moreover, $m$ could also appear to be 2 due to minute nonideal behaviors in the slip or plasticity models.

We conclude that, for dissipation from such dispersed spherical elasto-plastic flaws, $\sigma_{\mathrm{eq}}$ of Eq. (1.1) can be taken as $\sqrt{J_2}$, matching Eq. (1.2) with $\lambda = 0$.

We now turn to flat and thin elasto-plastic flaws.

## 4.3 Flat and thin flaws

For flat and thin flaws, the equivalent load parameter $A$ is the resolved shear stress on the plane of the flaw. Assuming the flaws are oriented randomly, we will have to average over orientations as well.

### 4.3.1 Averaging over a single plane orientation

Every flat and thin flaw is associated with a plane with a certain orientation (i.e., a certain unit normal vector $\hat{n}$). All such plane orientations are assumed equally likely, for simplicity. Consider one such randomly chosen plane orientation (as defined by its normal $\hat{n}$), and consider all the flaws whose flat portion has that same orientation. We will find the average dissipation from this subset of flaws, and then average over all plane orientations.

The energy dissipation due to a single flaw in a particular plane is taken as

$$E_d = ks\,(\tau - s) \quad \text{if } \tau > s, \quad \text{and 0 otherwise.}$$

Here, $\tau$ is the resolved shear stress in that plane (see Eq. (3.14)), $k$ depends on the size of the flaw and $s$ is the threshold strength. We treat the random variables $k$, $s$, and the plane orientation as all independent.

Assuming that the flaw strengths are power law distributed for small $s$, we find the average dissipation over all possible $s$ (similar to Eq. (4.2) above) as

$$D_{\text{plane}} = \int_0^\tau E_d p(s)\,\mathrm{d}s = Hk \int_0^\tau s(\tau - s)s^q\,\mathrm{d}s.$$

Thus, we find

$$D_{\text{plane}} = \left(\frac{Hk}{q^2 + 5q + 6}\right)\tau^{3+q} = \bar{\xi}\tau^m. \tag{4.4}$$

Here $\bar{\xi}$ is some constant (after averaging over the random variable $k$ if needed, as mentioned for the case of spherical flaws), and $m > 2$.

It remains to average over plane orientations.

### 4.3.2 Averaging over plane orientations

Consider a single plane with unit normal (see Fig. 4.2) given by

$$\widehat{n} = \sin\theta\cos\phi\;\widehat{i} + \sin\theta\sin\phi\;\widehat{j} + \cos\theta\;\widehat{k}. \tag{4.5}$$

For a given stress state $\mathbf{S}$, the traction vector is given by $\mathbf{t} = \mathbf{S}\cdot\widehat{n}$. The shear

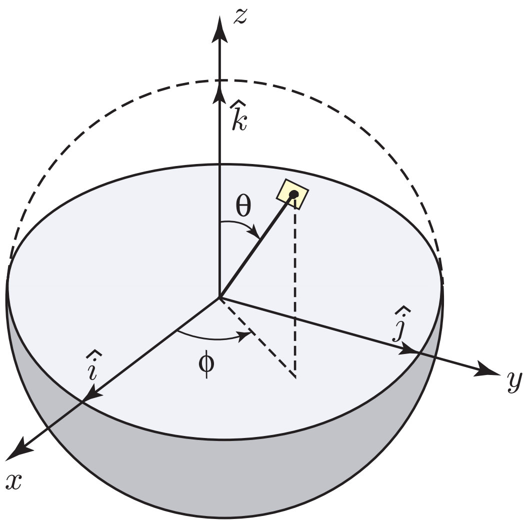

Figure 4.2: A typical plane with unit normal $\widehat{n}$ on the surface of a unit sphere.

component of the traction vector is $\boldsymbol{\tau} = (\mathbf{I} - \widehat{n}\widehat{n}) \cdot \mathbf{t}$. In matrix form we write

$$\boldsymbol{\tau} = (\mathbf{I} - \mathbf{n}\mathbf{n}^\intercal)\mathbf{S}\mathbf{n}.$$

The square of the shear stress magnitude is

$$|\tau|^2 = \mathbf{n}^\intercal\mathbf{S}(\mathbf{I} - \mathbf{n}\mathbf{n}^\intercal)(\mathbf{I} - \mathbf{n}\mathbf{n}^\intercal)\mathbf{S}\mathbf{n} = \mathbf{n}^\intercal\mathbf{S}(\mathbf{I} - \mathbf{n}\mathbf{n}^\intercal)\mathbf{S}\mathbf{n}. \tag{4.6}$$

We now proceed to choose a coordinate system, scale the stress for convenience, introduce an intermediate variable that simplifies expressions, and write the average as an integral as follows.

It is convenient to think in terms of principal stresses ($\sigma_1 \geq \sigma_2 \geq \sigma_3$), i.e., we work in a coordinate system in which the stress tensor is diagonal. We also scale the stress to ensure $\sigma_1 - \sigma_3 = 1$; later, the dissipation will be multiplied back by an appropriate scaling factor. Third, using the scaled stress, we define a new variable

$$\chi = \frac{\sigma_1 - \sigma_2}{\sigma_1 - \sigma_3}. \tag{4.7}$$

At this point, the scaled stress is

$$\overline{\mathbf{S}} = \begin{bmatrix} \sigma_1 & 0 & 0 \\ 0 & \sigma_1 - \chi & 0 \\ 0 & 0 & \sigma_1 - 1 \end{bmatrix}. \tag{4.8}$$

From Eqs. (4.5), (4.6) and (4.8) we get the square of the *scaled* shear stress magnitude as

$$\begin{aligned} \overline{\tau}^2 &= \frac{1-\cos 4\theta}{8}\left(1-\chi+\left(\chi-\frac{\chi^2}{2}\right)\cos 2\phi\right) \\ &\quad -\frac{\chi^2}{64}\left(3\cos 4\theta+(3+\cos 4\theta)\cos 4\phi+4(1-\cos 4\phi)\cos 2\theta-7\right). \end{aligned} \tag{4.9}$$

We note that the above does not depend on $\sigma_1$, and so is independent of the mean stress (because the plastic deformation is independent of mean hydrostatic stress).

We now average over all slip planes to obtain the average dissipation from a random dissipation site. From Eq. (4.4), we write

$$D_{\mathrm{ff}} = \bar{\xi} \times (\sigma_1 - \sigma_3)^m \times \frac{1}{2\pi}\int_0^{2\pi}\int_0^{\frac{\pi}{2}} (\overline{\tau}^2)^{\frac{m}{2}} \sin\theta \, \mathrm{d}\theta \mathrm{d}\phi, \tag{4.10}$$

where the subscript "ff" denotes flat flaws; the premultiplier $(\sigma_1 - \sigma_3)^m$ compensates for the earlier scaling whereby we took $\sigma_1 - \sigma_3 = 1$; and the averaging is over the upper hemisphere in Fig. 4.2.

Thus, Eqs. (4.9) and (4.10) together give the macroscopic dissipation. In principle $D_{\mathrm{ff}}$ has to be multiplied by the density of the flaws to obtain the specific dissipation (i.e., the dissipation per cycle and per unit volume). More practically, we note that $\bar{\xi}$ is to be considered a fitted material constant in any case.

Note that the double integral above still depends on the nondimensional stress parameter $\chi$, whose role is studied below. For that study, we set $\bar{\xi} = 1$ in our formulas below, with the understanding that the actual dissipation rate would have to be multiplied by a final single fitted material constant.

### 4.3.3 Dissipation: Special cases and symmetries

We first consider analytical evaluation of the integral of Eq. (4.10). $D_{\mathrm{ff}}$ can be found analytically if $m$ is an even integer. For $m = 2$ we find

$$D_{\mathrm{ff}} = \frac{2(\sigma_1 - \sigma_3)^2}{15}(\chi^2 - \chi + 1), \tag{4.11}$$

which is equivalent to

$$D_{\mathrm{ff}} = \frac{2}{15}\left\{(\sigma_1 - \sigma_2)^2 + (\sigma_2 - \sigma_3)^2 + (\sigma_3 - \sigma_1)^2\right\}, \tag{4.12}$$

which in turn is directly proportional to the distortional strain energy, as also the second invariant of the deviatoric stress ($D_{\mathrm{ff}} = \frac{4}{5}J_2$). For $m = 4$, $D_{\mathrm{ff}}$ turns out to be proportional to $J_2^2$ ($D_{\mathrm{ff}} = \frac{32}{35}J_2^2$). For other integer values of $m$ (see also Appendix C.1), there is no simple relation involving only $J_2$. Interestingly, when $m$ is an even integer, $D_{\mathrm{ff}}$ can be apparently be expressed using $J_2$ and $J_3$ together (where $J_3$ is the determinant of the deviatoric stress) at least up to $m = 12$: see Appendix C.1. When $m$ is not an even integer, we are unable to evaluate the integral of Eq. (4.10) in closed form, and have found no simple relations involving $J_2$ and $J_3$.

We now turn to numerical evaluation in Eq. (4.10), for arbitrary $m \geq 2$. For numerical integration we have used MATLAB's built-in routine "`dblquad`". We present some comparisons with analytical results for positive even integer $m$ in Table 4.1, where the accuracy is seen to be enough for our purposes. All subsequent numerical dissipation results in this thesis are obtained using such numerical integration.

| $m$ | Numerical integration | Analytical formula |
|---|---|---|
| 2 | 0.27841333333 | 0.27841333333 |
| 4 | 0.11073426306 | 0.11073426311 |
| 6 | 0.05033102734 | 0.05033102737 |
| 8 | 0.02463198442 | 0.02463198439 |
| 10 | 0.01266381088 | 0.01266381070 |

Table 4.1: $D_{\mathrm{ff}}$ from Eq. (4.10) with $\bar{\xi} = 1$, for the arbitrarily chosen stress state of $\sigma_1 = 1.26$, $\sigma_2 = 0.87$ and $\sigma_3 = -0.34$. The numerical integration is accurate to several significant digits.

Figure 4.3 shows plots for four $m$ values, with each curve scaled to make $D_{\mathrm{ff}} = 1$

at $\chi = 0.5$; the curves are symmetric about $\chi = 0.5$ in each case.

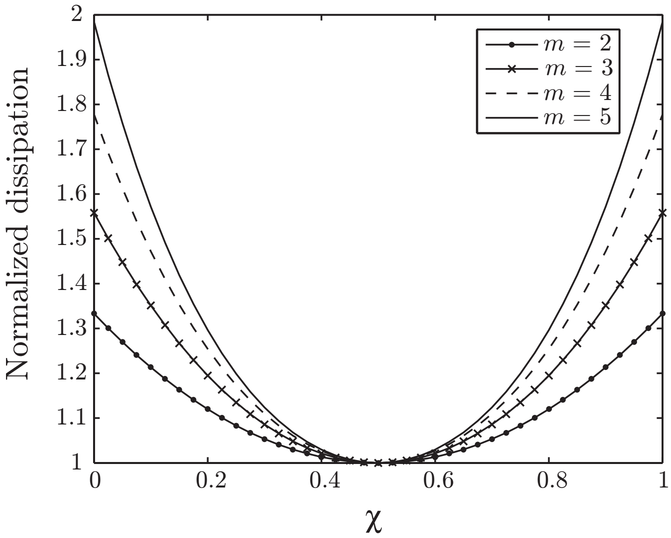

Figure 4.3: Dissipation plots for four $m$ values, normalized in each case so that $D_{\text{ff}} = 1$ at $\chi = 0.5$.

The symmetry about $\chi = 0.5$ can be explained using Mohr's circle diagram. For any given normal $\widehat{n}$, the resultant shear ($\tau$, assumed positive) and normal stress ($\sigma$), represented as a point $(\sigma, \tau)$ on the Mohr diagram, will lie in a region bounded by three circles (see Malvern (1969)).

Now see Fig. 4.4. In the figure, we see that the dissipation is the same for (a) and (b) because changing the sign of $\mathbf{S}$ has no effect on the dissipation since $\mathbf{S}$ is multiplied by $\sin \omega t$ in any case. Moreover, we have already seen above that the mean stress has no effect on the dissipation, whence (b) and (c) will be the same. Thus, replacing $\chi$ with $1 - \chi$ will not change the dissipation, and $D_{\text{ff}}$ is symmetric about $\chi = 0.5$.

### 4.3.4 Relation to distortional strain energy

We note that the second invariant of the deviatoric stress differs from the distortional strain energy by just a multiplicative constant (dependent on Young's modulus and Poisson's ratio), and we treat them as equivalent for our purposes. We have seen above that (e.g., for $m$ an even integer greater than 4), $D_{\text{ff}}$ is not a function of $J_2$

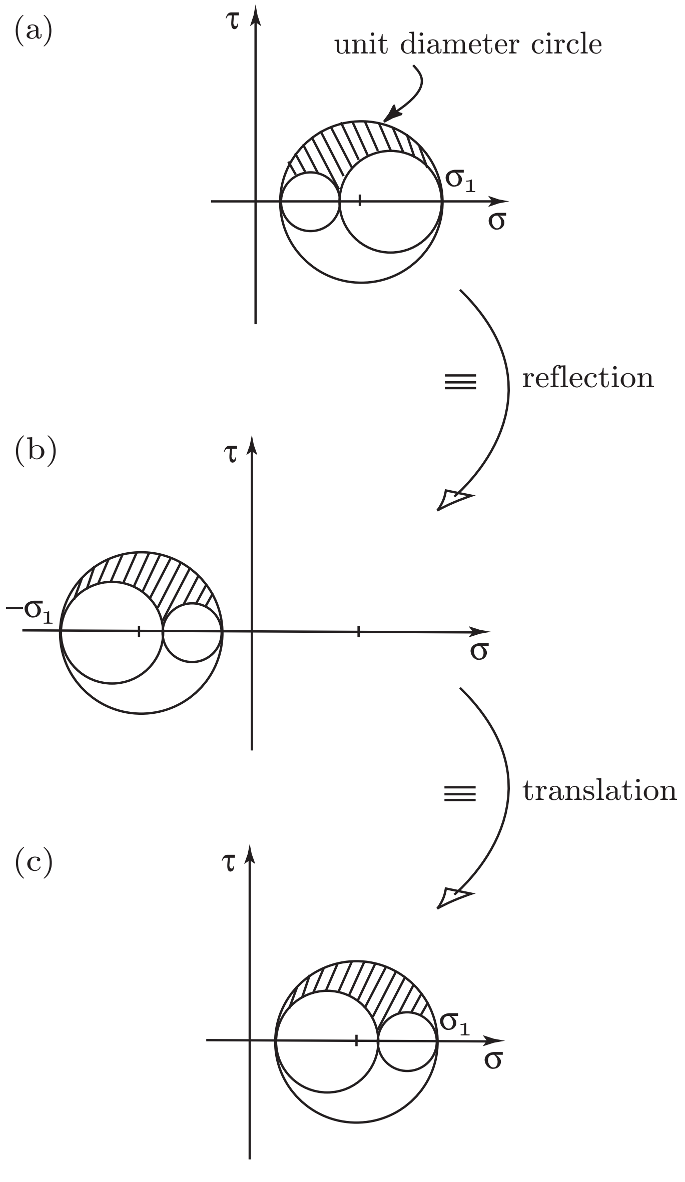
(a)
τ
unit diameter circle
σ₁
σ
≡
reflection
(b)
τ
−σ₁
σ
≡
translation
(c)
τ
σ₁
σ

Figure 4.4: Mohr's circle diagrams to show that $D_{\mathrm{ff}}$ is symmetric about $\chi = 0.5$.

alone. We now check the extent to which it can be *approximated* purely as a function of $J_2$.

For any arbitrary $m \geq 2$, expecting a contradiction, we nevertheless tentatively write

$$D_{\mathrm{ff}} = f(J_2),$$

whence (to incorporate a convenient scaling) we may just as well write

$$\frac{D_{\mathrm{ff}}}{J_2^{m/2}} = g(J_2), \tag{4.13}$$

where $f$ and $g$ are hypothesized (and as yet undetermined) functions.

For a simple numerical check of Eq. (4.13), we begin with 500 random stress states ($\sigma_1 \geq \sigma_2 \geq \sigma_3$) obtained as triples from a random number generator that gives standard normal variables (mean zero, variance unity). For each of these hypothetical stress states, we compute both $D_{\mathrm{ff}}$ and $J_2$. Figure 4.5 shows scatter plots of $D_{\mathrm{ff}} \times J_2^{-m/2}$ against $J_2$ for $m = 3$ and 6. If Eq. (4.13) were true, these scatter plots would collapse to single curves. But, they do not. Interestingly, they do each lie within horizontal bands, which is a consequence of the denominator in the left hand side of Eq. (4.13) being the correct power law. However, the nonzero widths of these bands show that, in general, $D_{\mathrm{ff}}$ is not a function of $J_2$ alone.

Next, we generated similar scatter data for several different $m$, using the same 500 random stress states for uniformity. The coefficient of variation (ratio of the standard deviation to the mean) was computed for each $m$. Figure 4.6 shows the results obtained. It is now clear that, except for $m = 2$ and 4, $D_{\mathrm{ff}}$ is not a function of $J_2$ alone. The deviation from a simple power law based on $J_2$ increases with $m$ for $m > 4$. For engineering modeling purposes, for moderate $m$, and keeping in mind that we have not in any case accounted for microscopic anisotropy as commented on by Whittier (1962), it appears that a simple power law based on $J_2$ might be sufficient (i.e., $D_{\mathrm{ff}} = \bar{\xi} J_2^{m/2}$ for, say, $2 \leq m \leq 6$).

In case $m$ is large (as it is for some materials (see Lazan (1968)), and also for academic interest, we briefly studied the large-$m$ asymptotic behavior of $D_{\mathrm{ff}}$. Details of this asymptotic analysis is given below. The asymptotic analysis shows analytically that, at least for large $m$, the dissipation is not a function of $J_2$ alone, consistent with our numerical observations here.

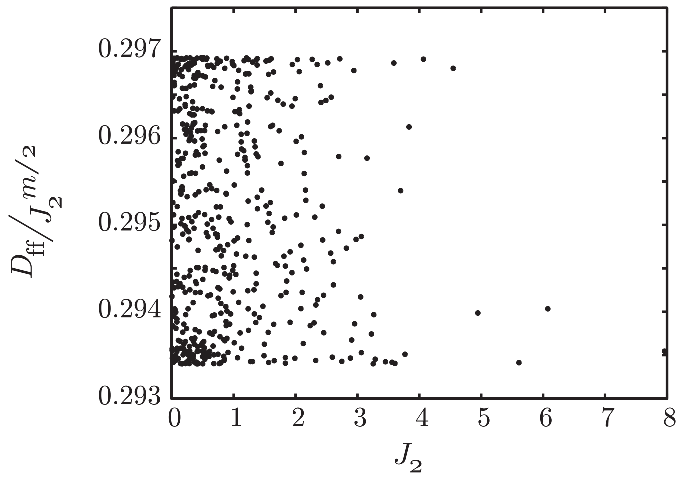

(a) $m = 3$

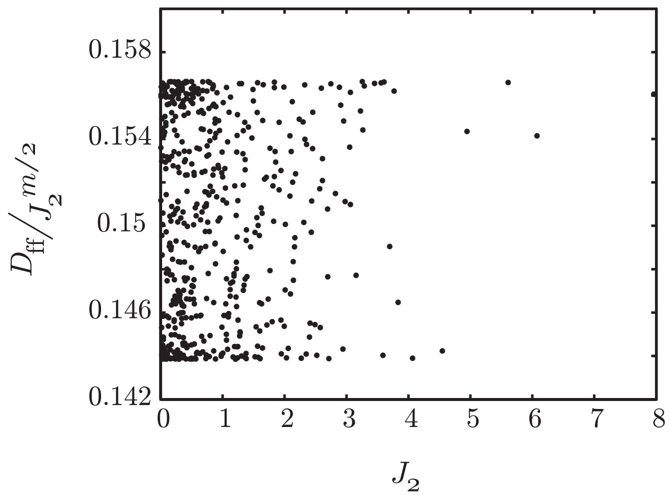

(b) $m = 6$

Figure 4.5: Comparison of $D_{\mathrm{ff}} \times J_2^{-m/2}$ against $J_2$ for $m = 3$ and 6.

### 4.3.5 Approximation for large $m$

The integral in Eq. (4.10) can be found exactly for $\chi(1-\chi) = 0$ (or equivalently, $\chi = 0$ or 1):

$$D_{\mathrm{ff}}|_{\chi(1-\chi)=0} = \frac{(\sigma_1 - \sigma_3)^m}{2^{m+1}} \frac{\sqrt{\pi}\,\Gamma(m+1)}{\Gamma(m+\frac{3}{2})}, \tag{4.14}$$

which for large $m$ can be approximated *via* Stirling's formula as

$$D_{\mathrm{ff}}|_{\chi(1-\chi)=0} \sim \frac{(\sigma_1 - \sigma_3)^m}{2^{m+1}} \frac{\sqrt{\pi}}{\sqrt{m}}. \tag{4.15}$$

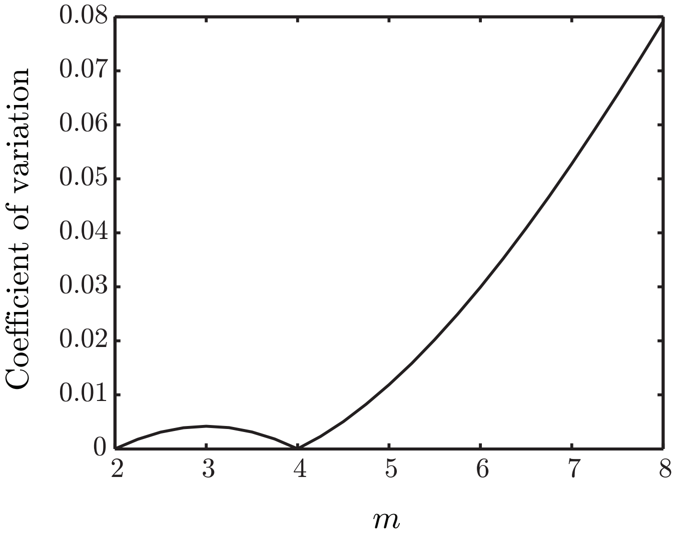

Figure 4.6: Coefficient of variation of $\dfrac{D_{\rm ff}}{J_2^{m/2}}$.

When $\chi(1-\chi)$ is not close to zero, the leading order behavior for large $m$ can be found by adapting Laplace's method (see Holmes (1995)) as

$$D_{\rm ff}|_{\chi(1-\chi)\neq 0} \sim \frac{(\sigma_1-\sigma_3)^m}{2^{m+1}} \frac{1}{m\sqrt{\chi(1-\chi)}}. \tag{4.16}$$

Details including higher order correction terms are given in Appendix C.2.

Figure 4.7 shows the utility of these large-$m$ asymptotics. For $\chi = 0$, we compare with the analytical results of Eq. (4.14), and for $\chi = 0.5$ we compare against results from numerical integration. For better scaling, the plotted quantity has been multiplied by $2^{m+1}$ in each case.

It is interesting to note that for large $m$, the dissipation for $\chi(1-\chi) \neq 0$ is smaller than for $\chi(1-\chi) = 0$ by a factor of $\mathcal{O}\left(m^{-1/2}\right)$. Incidentally, Eq. (4.16) shows that the dissipation for arbitrary $m$ is not a function of $J_2$ alone. To see this by contradiction, let

$$\zeta = \chi(1-\chi),$$

and assume that

$$F(\sigma_1, \sigma_3, \zeta) = H(J_2), \tag{4.17}$$

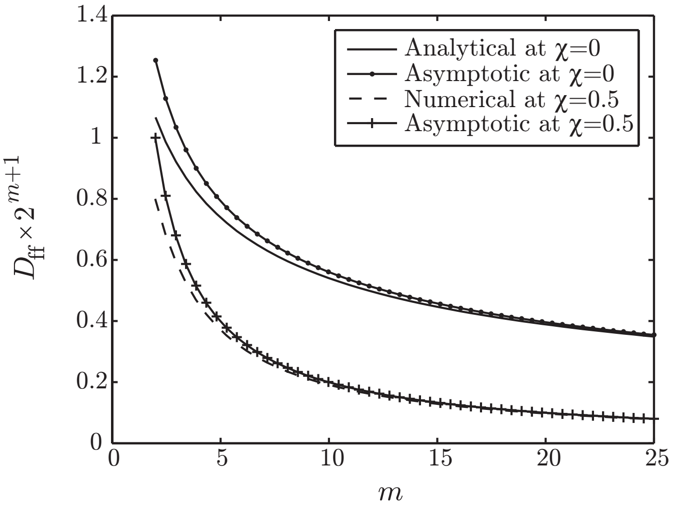

Figure 4.7: The leading-order approximations of Eq. (4.15) (i.e. for $\chi = 0$), and Eq. (4.16) with $\chi = 0.5$, against their corresponding correct values. In each case, $\sigma_1 - \sigma_3 = 1$ and only $m$ is varied.

where $F$ and $H$ are any two functions, and where in turn we know that

$$J_2 = J_2(\sigma_1, \sigma_3, \zeta) = \frac{1}{3}(1-\zeta)(\sigma_1 - \sigma_3)^2.$$

From Eq. (4.17),

$$\frac{\partial F}{\partial \sigma_1} = \frac{dH}{dJ_2}\frac{\partial J_2}{\partial \sigma_1} \quad \text{and} \quad \frac{\partial F}{\partial \zeta} = \frac{dH}{dJ_2}\frac{\partial J_2}{\partial \zeta},$$

which leads to

$$\frac{\partial F}{\partial \sigma_1} \div \frac{\partial F}{\partial \zeta} = \frac{\partial J_2}{\partial \sigma_1} \div \frac{\partial J_2}{\partial \zeta}, \tag{4.18}$$

independent of $H$. Choosing $F(\sigma_1, \sigma_3, \zeta)$ to be the right hand side of Eq. (4.16) with $\chi(1-\chi)$ set equal to $\zeta$, Eq. (4.18) reduces to

$$-\frac{2\zeta m}{\sigma_1 - \sigma_3} = -\frac{2(1-\zeta)}{\sigma_1 - \sigma_3},$$

or

$$m = \frac{1-\zeta}{\zeta},$$

which is a contradiction since $m$ and $\zeta$ can be varied independently. Therefore, at least for large $m$, the dissipation is not a function of $J_2$ alone (consistent with the numerical observations of Fig. 4.6).

## 4.4 Summary

In this chapter, we have considered a large number of uniformly dispersed microscopic elasto-plastic flaws and found their averaged macroscopic dissipation.

We have studied two special cases. In the first case, the flaws are spherical. In this case the net dissipation averaged over all flaws, assuming the flaw strengths are Weibull-distributed, give a purely $J_2$ based power law damping formula for the small-deformation regime.

In the second case, the flaws are flat and thin. In this case, the plastic dissipation can be described using a unidimensional model based on the resolved shear stress on the plane of the flaw. The macroscopic dissipation averaged over all flaws is obtained assuming a uniform distribution of flaw strengths and orientations. The resulting power law damping formula shows near-exact dependence on the distortional strain energy for moderate $m$ (say, $2 \leq m \leq 6$), but a different asymptotic behavior for larger $m$.

Academically, the main contribution of the present chapter is that it incorporates the triaxiality of the stress states starting from some reasonable underlying micromechanics as opposed to the *ad hoc* proposal of Eq. (1.2).

We note that Whittier's (1962) experiments with thin plate vibrations suggested that dilatational strain energy might play a role in material dissipation. Whittier speculated that microscopic anisotropy (due to grains) might lead to such an effect. Moreover, his rolled steel sheets were probably not isotropic, the consequences of which have not been worked out clearly. Nevertheless, his observation is not captured by the present model and suggests a possible direction for future work.

Finally, we suggest that for practical engineering designing purposes for metallic components and for moderate $m$ (say, $m$ between 2 to 6) a distortional strain energy based power law formula might be reasonable. For our finite element computation of effective damping ratios in the next chapter, we will adopt this formula.

# Chapter 5

# Modal damping computation examples with solid and shell elements

## 5.1 Introduction

In this chapter, we present some examples of computation of modal damping using solid elements. A second motivation for this chapter is the fact that many engineering structures are made of thin-walled (shell type) components. Use of solid elements for finite element modeling of these structures is computationally expensive and shell elements are preferred. With this view, we develop a computational procedure for calculating modal damping ratios of shell like structures using shell elements in ANSYS.

We have suggested, in the previous chapter, that for practical engineering design purposes for metallic components, a distortional strain energy based power law formula may be reasonable provided the index ($m$) of the power law is not large. In this chapter, we adopt this distortional strain energy based formula[1]. Accordingly, the equivalent stress ($\sigma_{eq}$) in

$$D = \xi \sigma_{eq}^{m} \tag{5.1}$$

---

[1] However, the procedure outlined in this chapter can be used for computation of modal damping using any other dissipation formula.

is obtained using

$$\sigma_{eq}^2 = I_1^2 - 3I_2 = 3J_2 = \frac{1}{2}\left\{(\sigma_1-\sigma_2)^2 + (\sigma_2-\sigma_3)^2 + (\sigma_3-\sigma_1)^2\right\}, \tag{5.2}$$

where $I_1$ and $I_2$ are the first and second stress invariants respectively, $J_2$ is the second invariant of the deviatoric stress, and $\sigma_1$, $\sigma_2$, and $\sigma_3$ are the three principal stresses[2].

The distortional strain energy based damping formula is simple, and allows some analytical progress. We can compute the modal damping ratios analytically for a few selected cases. We will validate our finite element computations below against such analytical results.

We will first consider solid elements (SOLID187) for which the procedural details have already been presented in Chapter 2. After validating our solid element results, we will consider shell elements (SHELL181) and develop a computational procedure for modal damping computation. Shell results will be verified against both analytical and solid element results.

## 5.2 Computation of $\zeta_{\mathit{eff}}$ using solid elements

Use of SOLID187 in computation of $\zeta_{\mathit{eff}}$ has been presented earlier in section 2.5.3 where the dissipation was computed using Eq. (2.11). In comparison to the procedure outlined there, the dissipation formula will be the only change here. In the present case, the dissipation at each Gauss point has to be calculated using Eq. (5.1) instead of Eq. (2.11) and the rest of the calculation remains the same.

For the reader's convenience, we summarize the entire calculation procedure in this paragraph. The given geometry is first modeled using 10 noded tetrahedral elements (SOLID187) using automatic meshing within ANSYS. Modal analysis is carried out in ANSYS and nodal displacements for each mode are extracted. Element wise volume integration of $\sigma_{eq}^m$ is then carried out externally using Gauss quadrature, where again interpolation using the element shape function is used to compute strains and then stresses. The element wise integrals of $\sigma_{eq}^m$ are added to obtain the total energy dissipation ($-\Delta\overline{E}$). $\zeta_{\mathit{eff}}$ is computed using Eq. (2.14) after noting that the total kinetic energy ($\overline{E}$) is just $\frac{1}{2}\omega^2$ because the mode shape is mass normalized (see Eq. (2.18)).

---

[2] Note that if we use strain in place of stress in Eq. (5.1), the final result will be the same because the macroscopic dissipation ($D$) is based on distortional strain energy.

### 5.2.1 Validation of $\zeta_{\mathit{eff}}$ computation with known analytical results

In this section, we validate our finite element calculations of $\zeta_{\mathit{eff}}$ against a few selected cases for which analytical results can be obtained. We mostly consider $m = 2$ in Eq. (5.1). We will discuss computations for $m \geq 2$ in section 5.4 below.

#### 5.2.1.1 Transverse vibration of a simply supported beam

The fundamental mode shape for transverse vibration of a simply supported beam (Fig. 5.1) is a half sine, and so we take the displacements

$$y(x,t) = A_1 \sin\frac{\pi x}{L}\sin\omega t. \tag{5.3}$$

The maximum strain energy for this vibration mode is

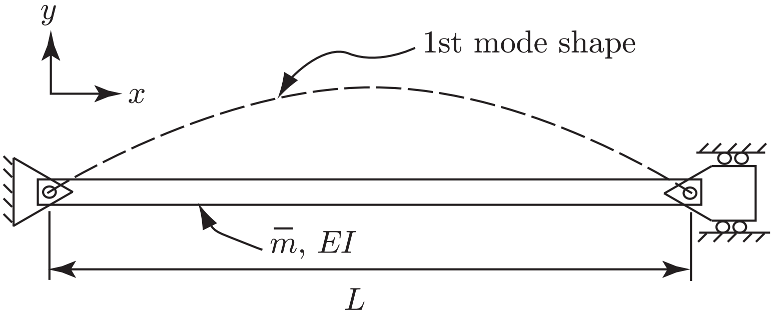

Figure 5.1: Transverse vibration of a simply supported beam.

$$\overline{E} = A_1^2\int_0^L \frac{EI}{2}\left(\frac{\pi^2}{L^2}\right)^2 \sin^2\frac{\pi x}{L}dx = \frac{A_1^2 EI\pi^4}{4L^3}. \tag{5.4}$$

The amplitude of the bending stress at a distance $z$ from the neutral axis of the beam is given by

$$\sigma = \frac{EI\phi''(x)z}{I} = -\frac{E\pi^2}{L^2}A_1\sin\frac{\pi x}{L}z. \tag{5.5}$$

This same value of $\sigma$ will be used as $\sigma_{eq}$. Now, using Eq. (5.2), we calculate the energy dissipated over one cycle as

$$-\Delta\overline{E} = \xi \int_V \sigma_{eq}^2 dV = \left(\frac{\xi A_1^2 E^2 \pi^4}{L^4}\right) \times \int_V \sin^2 \frac{\pi x}{L} z^2 dV$$
$$= \left(\frac{\xi A_1^2 E^2 \pi^4}{L^4}\right) \times \frac{LI}{2} = \frac{\xi A_1^2 E^2 I \pi^4}{2L^3}. \tag{5.6}$$

Thus,

$$\zeta_{\mathit{eff}} = \frac{1}{4\pi} \times \frac{-\Delta\overline{E}}{\overline{E}} = \frac{\xi E}{2\pi}. \tag{5.7}$$

From the above equation we get

$$\frac{2\pi\zeta_{\mathit{eff}}}{\xi E} = 1. \tag{5.8}$$

Here, $E$ is the Young's modulus of the material, not to be confused with $\overline{E}$ which is the total energy of the system averaged over one cycle.

In the rest of this section, all the bodies considered will be continuum objects but we will consider specific modes thereof. For each mode, the effective damping ratios will be normalized with $\frac{\xi E}{2\pi}$ and we will report $\frac{2\pi\zeta_{\mathit{eff}}}{\xi E}$ and compare with unity.

#### 5.2.1.2 Comparison with finite element computation

A finite element model of the simply supported uniform beam (Fig. 5.1) is shown in Fig. 5.2 (a). The total number of elements in the model is 33237. The beam dimensions are 1.0 m × 0.05 m × 0.025 m. As a realization of simple supports, nodal displacements were constrained along a horizontal line passing through the middle of each end face. Material properties for this model are given in Table 5.1.

| | |
|---|---|
| Young's modulus ($E$ in GPa) | 210 |
| Poisson's ratio ($\nu$) | 0.3 |
| Density ($\rho$ in Kg/m$^3$) | 7800 |

Table 5.1: Material properties considered in the finite element model.

The finite element procedure as described above has given $\frac{2\pi\zeta_{\mathit{eff}}}{\xi E}$ for the mode shown in Fig. 5.2 (b) to be 1.001, which agrees well with Eq. (5.7).

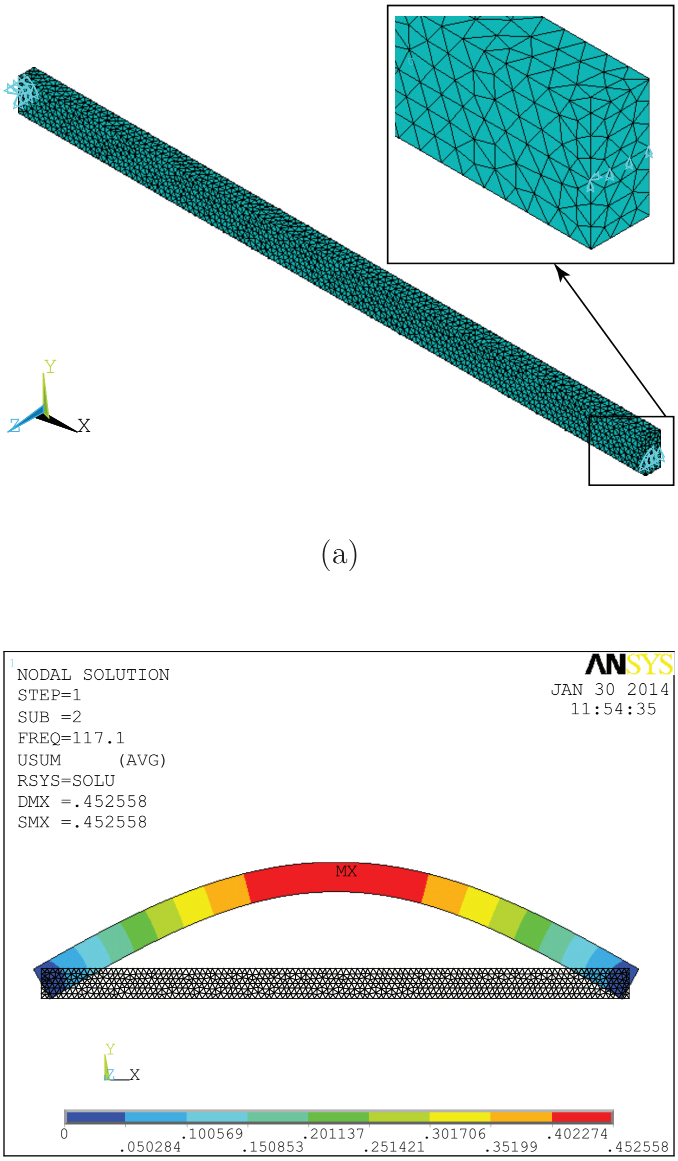
Y
Z
X
NODAL SOLUTION
STEP=1
SUB =2
FREQ=117.1
USUM (AVG)
RSYS=SOLU
DMX =.452558
SMX =.452558
ANSYS
JAN 30 2014
11:54:35
MX
0
.050284
.100569
.150853
.201137
.251421
.301706
.35199
.402274
.452558

(a)

(b)

Figure 5.2: (a) Finite element model of the simply supported beam. (b) Transverse vibration mode from the FE model. Note that the bending is in-plane and this is not the first mode of vibration. However, this is a mode where beam theory is more accurate.

#### 5.2.1.3 Modal damping in other analytically tractable geometries

We now consider several different geometries and compute their modal damping values for specific modes. For the geometries considered here, a few closed-form solutions are readily available. The finite element results are verified against those closed-form results.

We consider the following cases:

1) Torsion of a circular rod

2) Bending of a thin rectangular plate

3) Uniform radial mode of a thin-walled spherical shell

4) Longitudinal vibration of a laterally constrained rod

5) First purely radial mode of a solid sphere

Detailed description of both analytical and computational approach for the above five solid bodies are presented in Appendix C. However, the net results in each case are summarized in Table 5.2. The beam bending case is also included.

| | Solid models | Modes | Numerical $\dfrac{2\pi\zeta_{\mathit{eff}}}{\xi E}$ | |
|---|---|---|---|---|
| | | | ANSYS | Analytical |
| 1 | Circular rod | Torsion | 1.154 | 1.154 |
| 2 | Beam | Bending | 1.001 | 1.000 |
| 3 | Plate | Bending | 0.867 | 0.868 |
| 4 | Thin sphere | Radial | 0.714 | 0.714 |
| 5 | Laterally constrained rod | Axial | 0.440 | 0.440 |
| 6 | Solid sphere | Radial | 0.114 | 0.114 |

Table 5.2: Values of $\zeta_{\mathit{eff}}$ for six solid models considered.

Although the numerical method can compute $\zeta_{\mathit{eff}}$ for as many vibration modes as we wish, we have identified some that are intuitively simple and can be analytically studied as well, as listed in Table 5.2. An interesting result is that the ratio $\dfrac{2\pi\zeta_{\mathit{eff}}}{\xi E}$ varies over one order of magnitude over the cases considered. The torsion dominated mode has the greatest damping. The bending mode which has zero volume change has next highest damping. Radial mode of the spherical shell which has stretching in two directions and Poisson's effect in one direction has less damping presumably because some of the energy goes into volumetric strain. The laterally constrained rod is intermediate, and the first purely radial mode of a sphere is the least damped of all. Thus, it is seen that shape can have an effect on damping of specific modes of objects even when $m = 2$ in Eq. (5.1) ($m$ other than 2 will be discussed later).

## 5.3 Computation of $\zeta_{\mathit{eff}}$ using shell elements

In practical situations, we might be interested to compute $\zeta_{\mathit{eff}}$ for thin-walled structures. Use of shell elements is convenient for finite element simulation of such structures. For this reason, in this section, we present finite element computation of $\zeta_{\mathit{eff}}$ using shell elements (SHELL181) in ANSYS.

### 5.3.1 Analysis method

The SHELL181 element in ANSYS is used for analyzing thin to moderately-thick shell structures. It is a four-node element with six degrees of freedom at each node: three translations ($u$, $v$, and $w$ in $x$, $y$, and $z$ direction respectively), and three rotations ($\theta_x$, $\theta_y$, and $\theta_z$ about the $x$, $y$, and $z$-axis respectively).

The displacement shape function (in terms of local coordinates $s$ and $t$ on the parent element) for $u$ is given as

$$u = \frac{1}{4}u_I(1-s)(1-t) + \frac{1}{4}u_J(1+s)(1-t) + \frac{1}{4}u_K(1+s)(1+t) + \frac{1}{4}u_L(1-s)(1+t). \quad (5.9)$$

Shape functions for $v$, $w$, $\theta_x$ ,$\theta_y$, and $\theta_z$ are analogous to Eq. (5.9). Further details of this element can be found in ANSYS theory manual (ANSYS manual, 2009), and in Dvorkin (1982), Dvorkin (1984), Bathe and Dvorkin (1985), and Bathe and Dvorkin (1986).

We note here that the SHELL181 element formulation within ANSYS gives element stresses at **TOP**, **MID**DLE, and **BOT**TOM of the shell thickness, if proper key-option (KEYOPT(8)=2) is used during analysis (see Fig. 5.3 for the normal stress component in the $x$ direction).

We also note that in a shell formulation (see Bathe (1996)), within a shell element, the stress components vary differently in the thickness direction. The in-plane stress components ($\sigma_x$, $\sigma_y$, and $\tau_{xy}$) have linear variation through the element thick-

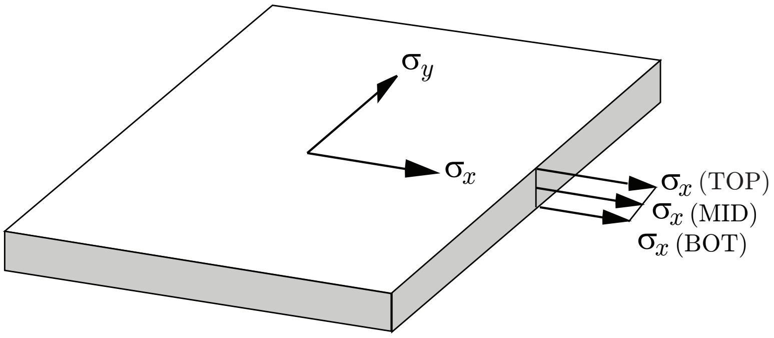

Figure 5.3: SHELL181 stress output at three locations through the element thickness.

ness whereas the variation of the out-of-plane shear stresses ($\tau_{yz}$ and $\tau_{zx}$) is quadratic. Accordingly, knowing the three stresses (using SHELL TOP, MID and BOT stresses in ANSYS) at three points through the thickness, we can use quadratic interpolation and find the assumed stresses correctly. Consequently, more complicated functions (for example, $\sigma_{eq}$ in our case) of those stresses can be integrated using several Gauss points through the thickness, without any contradiction. We have used five Gauss points in our computations.

We briefly present the computational procedure of $\zeta_{eff}$ using SHELL181 elements in ANSYS and compare the results against known analytical results. The thin-walled vibrating object of interest is first meshed using SHELL181 elements using automatic meshing within ANSYS. Then modal analysis is carried out which yields natural frequencies and mass-normalized mode shapes. For each vibration mode, the element stresses at three locations (TOP, MIDDLE and BOTTOM) are extracted for every element in the model. Gauss point (through the thickness) stresses for each element are calculated separately using interpolated stress values as mentioned above. Then, the equivalent stresses are computed at these locations. The dissipation over each element volume is approximated using

$$(D)^e = \frac{\text{element volume}}{2} \times \sum_{k=1}^{5} w_k \sigma_{eq,k}^2. \tag{5.10}$$

The constant $\xi$ is not incorporated here. Final results have to be multiplied by $\xi$

(as fitted from data for the material of interest).

The elementwise integrals are added up to obtain the total dissipation per cycle,

$$-\Delta\overline{E} = \sum_{\text{all elements}} (D)^e. \tag{5.11}$$

We have used mass-normalized mode shapes. Therefore, the total kinetic energy of the body in this vibration mode is

$$\overline{E} = \frac{1}{2}\omega^2 \int_V \rho \boldsymbol{\phi}^{\mathsf{T}} \boldsymbol{\phi} \, dV = \frac{\omega^2}{2}, \tag{5.12}$$

where $\omega$ is the natural frequency of the selected vibration mode.

Using Eqs. (5.10), (5.11), and (5.12) we obtain the effective damping ratio ($\zeta_{\mathit{eff}}$) as

$$\zeta_{\mathit{eff}} = \frac{1}{4\pi} \times \left( \frac{-\Delta\overline{E}}{\overline{E}} \right) = \frac{1}{4\pi} \times \frac{\xi \sum (D)^e}{\frac{1}{2}\omega^2}. \tag{5.13}$$

### 5.3.2 Comparison with known analytical results

We now compare the SHELL181 analysis results of $\zeta_{\mathit{eff}}$ with previously obtained analytical results for two cases. In the first case, we consider the transverse vibration of a simply supported rectangular plate. The plate (1.0 m × 0.5 m × 0.005 m) is modeled using 648 shell elements (see Fig. 5.4). In the second case, we consider the purely radial mode of the thin-walled spherical shell. The spherical shell (mean diameter 4 m and thickness 0.1 m) is modeled using 2944 elements (see Fig. 5.5). The material properties taken for these two cases were shown in Table 5.1.

| Geometry | Modes | Numerical $\frac{2\pi\zeta_{\mathit{eff}}}{\xi E}$ | | |
|---|---|---|---|---|
| | | ANSYS Shell | ANSYS Solid | Analytical |
| Plate | Bending | 0.867 | 0.867 | 0.868 |
| Thin sphere | Radial | 0.714 | 0.714 | 0.714 |

Table 5.3: Results for two shell models considered for validation of $\zeta_{\mathit{eff}}$ computations using SHELL181 elements. The results obtained previously using solid elements are also given here.

The computed effective damping ratios for these shell models using above shell formulation are reported in Table 5.3. For completeness the $\zeta_{\mathit{eff}}$ values from the

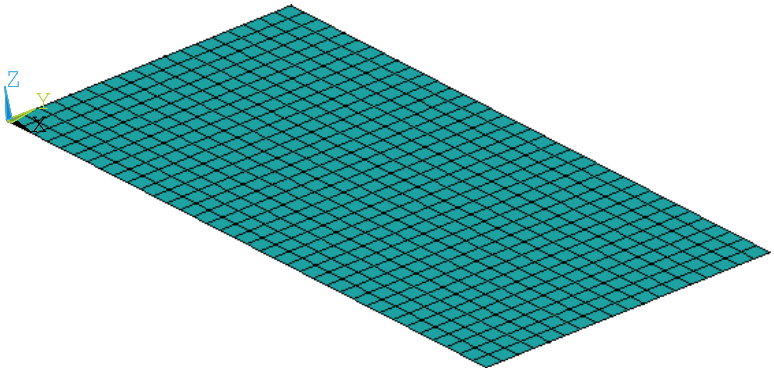

Figure 5.4: Shell model of thin rectangular plate.

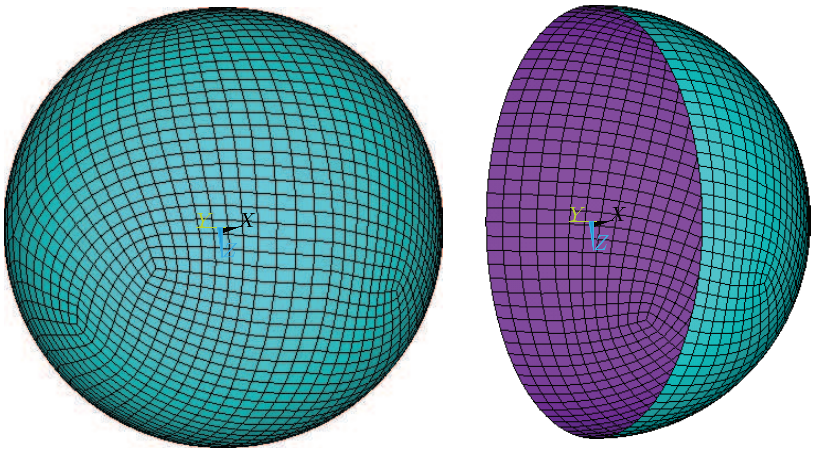

Figure 5.5: Shell model of thin-walled spherical shell. Half of the model is shown on the right.

previous solid element computations are also reported in the table. We note that shell elements give accurate results with few elements and less computation.

## 5.4 Normalization for $m > 2$

So far, in our computational examples, we have considered $m = 2$ in Eq. (5.1). Now, we consider $m \geq 2$. For $m > 2$ we require a normalization (or scaling) that has to be incorporated in the mode shapes of our finite element computations.

If the mode shapes (i.e. the eigenvectors) are multiplied by a factor $k_s$, then the strain energy ($\overline{E}$) will increase by a factor of $k_s^2$. And for $m = 2$ the dissipated energy ($-\Delta\overline{E}$) will also increase by a factor of $k_s^2$. Therefore, $\zeta_{\mathit{eff}}$ will not change due to such scaling factors when $m$ is 2.

However, when $m$ is greater than 2, the scaling of the eigenvectors matters. We have chosen to scale the eigenvectors so that the *average volumetric strain energy density* is unity (in our case because we are using SI units in this chapter it will be 1 Joule/m$^3$). For steel under uniaxial tension, this corresponds to an extremely small strain of the order of $10^{-11}$. An analyst wishing to use a different normalizing value can easily adapt our procedure for the same.

As a consequence of the above scaling we note that, for any arbitrary $m$, the size (or the volume) of a solid object does not affect the damping values. As an example, two simply supported beams of dimensions 1.0 m × 0.05 m × 0.025 m, and 2.0 m × 0.1 m × 0.05 m will lead to the same $\zeta_{\mathit{eff}}$. The advantage of such scaling is that we can compare damping values of different *shapes* of objects without worrying about their sizes being unequal.

As the mode shapes ($\boldsymbol{\phi}$) are to be scaled by $k_s$ to set the *average volumetric strain energy density* to unity, we write

$$\frac{k_s^2\left(\frac{1}{2}\omega^2\int_V \rho\boldsymbol{\phi}^{\mathsf{T}}\boldsymbol{\phi}\,dV\right)}{V} = 1, \tag{5.14}$$

where $V$ is the total volume of the body and the mass-normalized mode shape $\boldsymbol{\phi}$ is to be scaled by $k_s$. Now, noting that $\int_V \rho\boldsymbol{\phi}^{\mathsf{T}}\boldsymbol{\phi}\,dV = 1$ for the mass-normalized mode shape, we get

$$k_s = \sqrt{\frac{2V}{\omega^2}}. \tag{5.15}$$

Both $\omega$ and $V$ are obtained from the finite element simulation. The effective damping ratio is calculated as

$$\zeta_{\mathit{eff}} = \frac{1}{4\pi} \times \frac{\xi\sum(D)^e}{V}, \tag{5.16}$$

where the dissipation $(D)^e$ depends on $k_s$ and the denominator is just $V$, because the average volumetric strain energy density is already set to 1.

The above normalization for the mode shape (i.e. extracted nodal displacements from ANSYS) is directly applicable for the case of SOLID187 elements. But for computations using SHELL181 element, we directly extract the element stresses from ANSYS. Therefore, above scaling ($k_s$ in Eq. (5.15)) has to be directly applied to the element stresses and then $\zeta_{\mathit{eff}}$ will be calculated using Eq. (5.16).

## 5.5 Matlab GUI for automated computation of $\zeta_{\mathit{eff}}$

For fast and reliable computations of $\zeta_{\mathit{eff}}$, a Matlab based graphical user interface (GUI) has been developed using GUIDE, the graphical user interface development environment of Matlab.

The geometry of the solid object is meshed (either using SOLID187 or SHELL181 elements) within ANSYS with proper boundary conditions and material properties. Subsequently, this model is used in the GUI for both modal analysis and the $\zeta_{\mathit{eff}}$ computations for several chosen modes.

A screen shot of the GUI is shown in Fig. 5.6. The GUI consists of five panels. In *ANSYS Model* panel the job directory, the ANSYS finite element model (the database file) and the path of the ANSYS executable should be provided. The *Modal Analysis* panel is for doing the modal simulation. The number of modes to be extracted has to be given here. The third panel, *Solid or Shell Model*, is for the selection of element type (SOLID187 or SHELL181) used in the ANSYS database file. One of this box should be clicked during the analysis. The *Modal Damping* panel is for the $\zeta_{\mathit{eff}}$ computations for the selected vibration modes. *Save/Run* is for the final run. *Save* is for saving the existing settings in GUI for a future run, whereas *Run* is for the entire computation for extracting the effective damping ratios. The final results, i.e. the computed $\zeta_{\mathit{eff}}$ values, will be saved in a text file in the job directory.

## 5.6 Effects of stress concentration on damping

In the previous sections, we have developed a procedure of $\zeta_{\mathit{eff}}$ computations using both solid and shell elements in ANSYS. We have also verified our computations against a few analytical results.

Now, we consider a pair of objects of less analytically tractable shape and com-

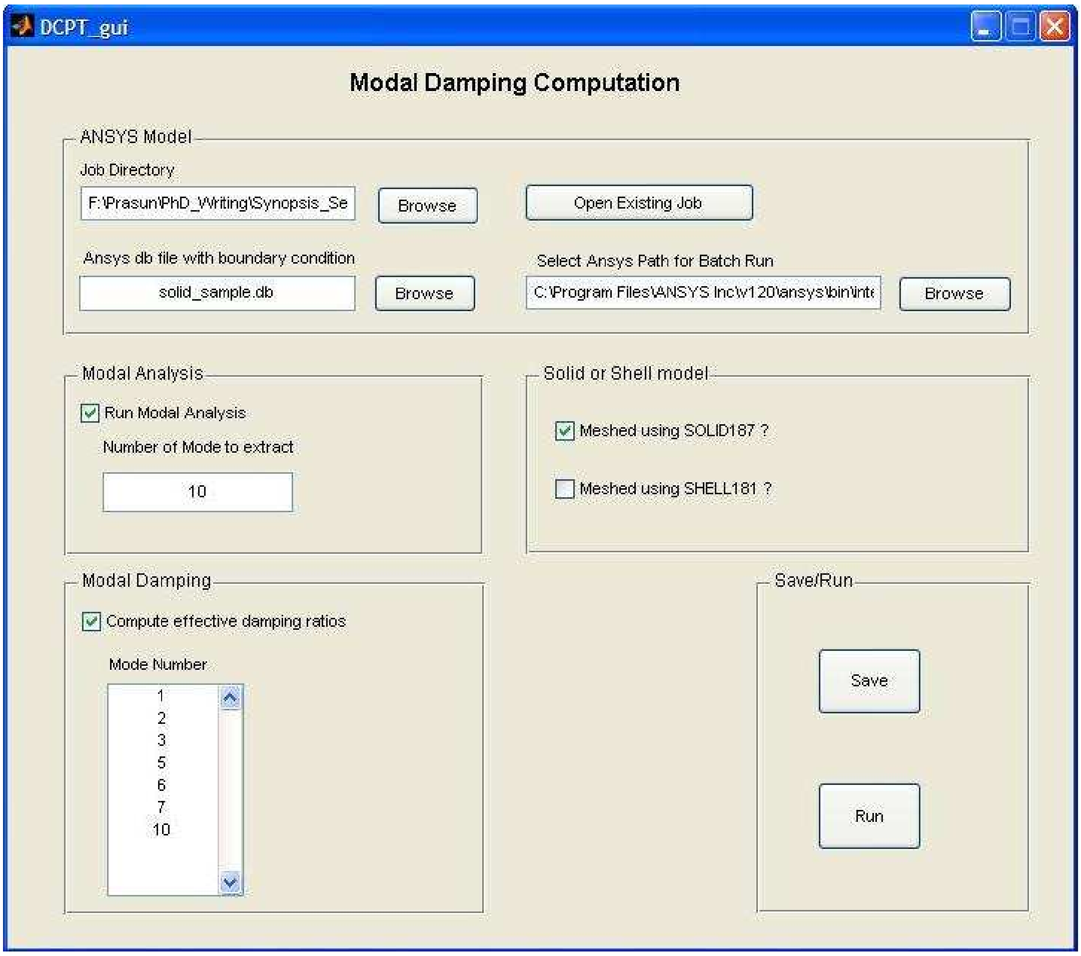

DCPT_gui

Modal Damping Computation

ANSYS Model

Job Directory: F:\Prasun\PhD_Writing\Synopsis_Se

Ansys db file with boundary condition: solid_sample.db

Select Ansys Path for Batch Run: C:\Program Files\ANSYS Inc\v120\ansys\bin\int

Modal Analysis

☑ Run Modal Analysis

Number of Mode to extract: 10

Solid or Shell model

☑ Meshed using SOLID187 ?

☐ Meshed using SHELL181 ?

Modal Damping

☑ Compute effective damping ratios

Mode Number:
1
2
3
5
6
7
10

Figure 5.6: Matlab based GUI for computing $\zeta_{eff}$ using ANSYS.

pute their modal damping ratios. We consider $m \geq 2$ in Eq. (5.1). We show, with a computational example, that for $m > 2$ stress concentrations play a role in determining damping values. In our computational example, we consider two flat rectangular plates. See Fig. 5.7. In Fig. 5.7 (b), slots are introduced in the plate to introduce stress concentrations within the vibration modes. The planar dimensions of both the plates are taken to be the same (1 m × 1 m), and the thicknesses are adjusted such that the first natural frequencies of both plates are approximately equal. We use SOLID187 elements for the mesh. We compute the effective damping ratios for the first few modes of these plates with unconstrained boundary conditions. The first three vibration modes of these plates are shown in Fig. 5.8. The figure shows that the overall displacements in the corresponding vibration modes of these two

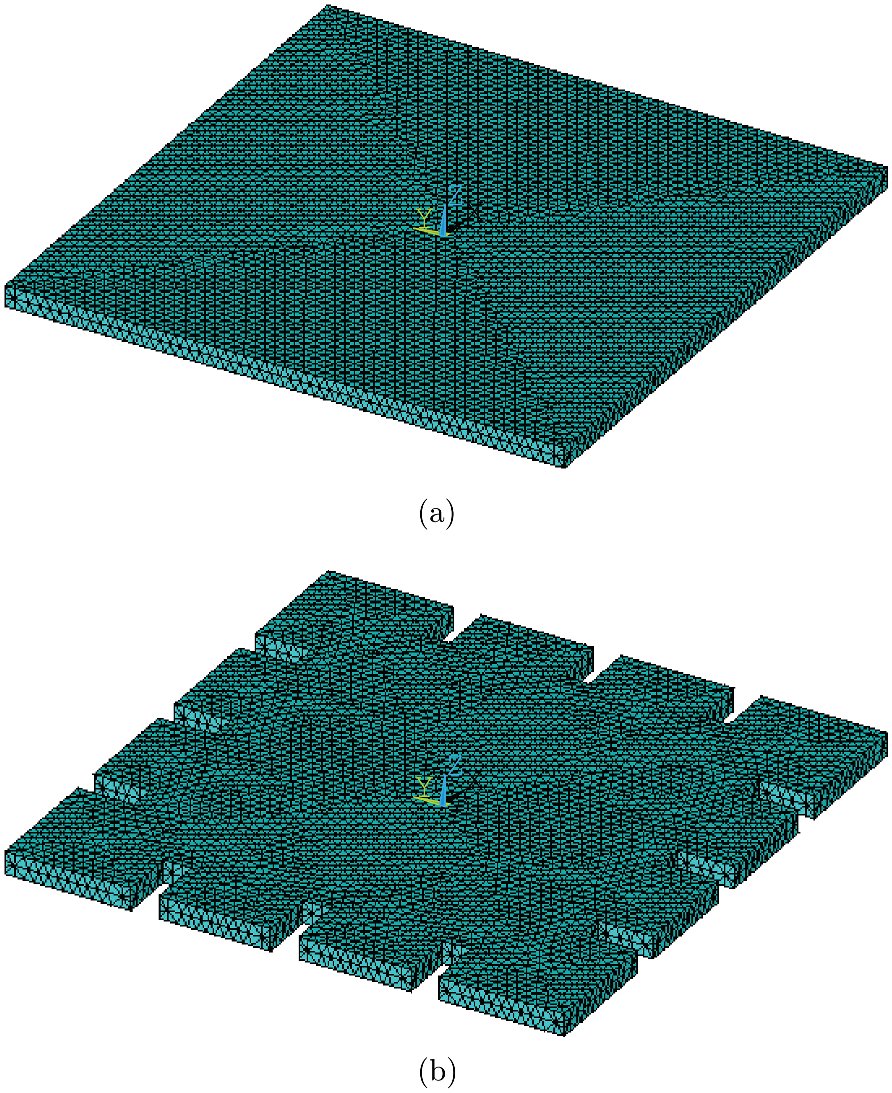

(a)

(b)

Figure 5.7: Rectangular plates meshed using solid elements. (a) Uncut plate with dimensions 1 m×1 m×0.0365 m (39856 elements). (b) Slotted plate with dimensions 1 m × 1 m × 0.04 m (53590 elements). Near the edges of this plate, 12 rectangular (0.1 m × 0.05 m) slots are cut to introduce stress concentrations.

plates are similar.

The damping results are reported in Table 5.4 for $m = 2$, 3, and 6. For comparison purposes, the $\zeta_{eff}$ values are normalized with respect to the first vibration mode of the uncut plate (i.e., for each $m$ the $\zeta_{eff}$ values for the first mode of the uncut plate is set to 1). It is seen that the damping values are higher in the slotted plate. This is due to the presence of stress concentration. It is also seen that the effect of

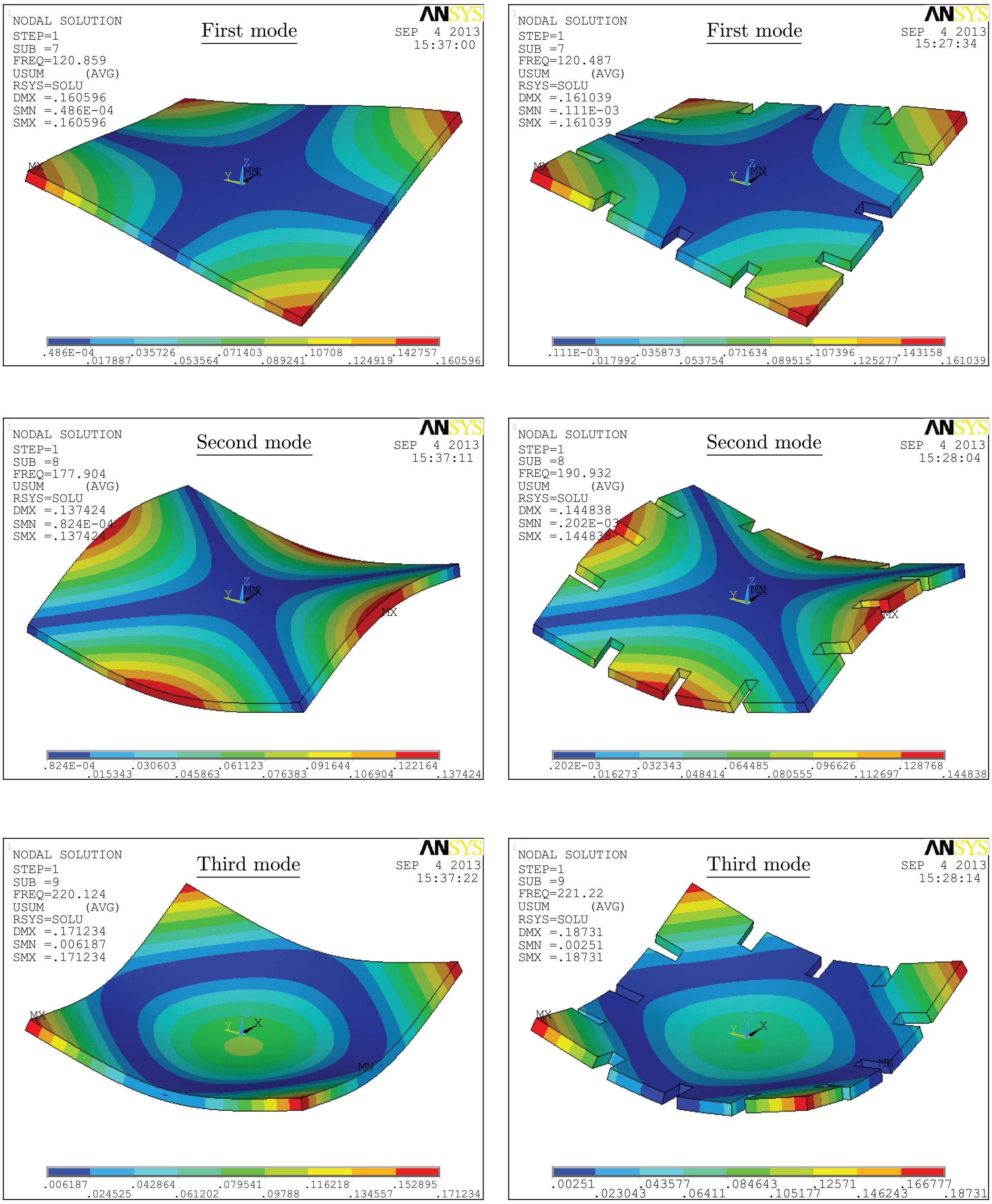
First mode

First mode

Second mode

Second mode

Third mode

Third mode
NODAL SOLUTION
STEP=1
SUB =7
FREQ=120.859
USUM (AVG)
RSYS=SOLU
DMX =.160596
SMN =.486E-04
SMX =.160596
SEP 4 2013
15:37:00
MX
MN
.486E-04 .017887 .035726 .053564 .071403 .089241 .10708 .124919 .142757 .160596
NODAL SOLUTION
STEP=1
SUB =7
FREQ=120.487
USUM (AVG)
RSYS=SOLU
DMX =.161039
SMN =.111E-03
SMX =.161039
SEP 4 2013
15:27:34
MX
MN
.111E-03 .017992 .035873 .053754 .071634 .089515 .107396 .125277 .143158 .161039
NODAL SOLUTION
STEP=1
SUB =8
FREQ=177.904
USUM (AVG)
RSYS=SOLU
DMX =.137424
SMN =.824E-04
SMX =.137424
SEP 4 2013
15:37:11
MN
MX
.824E-04 .015343 .030603 .045863 .061123 .076383 .091644 .106904 .122164 .137424
NODAL SOLUTION
STEP=1
SUB =8
FREQ=190.932
USUM (AVG)
RSYS=SOLU
DMX =.144838
SMN =.202E-03
SMX =.144838
SEP 4 2013
15:28:04
MN
MX
.202E-03 .016273 .032343 .048414 .064485 .080555 .096626 .112697 .128768 .144838
NODAL SOLUTION
STEP=1
SUB =9
FREQ=220.124
USUM (AVG)
RSYS=SOLU
DMX =.171234
SMN =.006187
SMX =.171234
SEP 4 2013
15:37:22
MX
MN
.006187 .024525 .042864 .061202 .079541 .09788 .116218 .134557 .152895 .171234
NODAL SOLUTION
STEP=1
SUB =9
FREQ=221.22
USUM (AVG)
RSYS=SOLU
DMX =.18731
SMN =.00251
SMX =.18731
SEP 4 2013
15:28:14
MX
MN
.00251 .023043 .043577 .06411 .084643 .105177 .12571 .146243 .166777 .18731

Figure 5.8: First three vibration modes of the rectangular plates.

the stress concentration increases as $m$ increases. An increase of approximately one and a half to two times in the $\zeta_{eff}$ values is seen for $m = 6$.

| Mode | Frequency (Hz) | | $\zeta_{\mathit{eff}}$ for $m = 2$ | | $\zeta_{\mathit{eff}}$ for $m = 3$ | | $\zeta_{\mathit{eff}}$ for $m = 6$ | |
|---|---|---|---|---|---|---|---|---|
| | Plate 1 | Plate 2 | Plate 1 | Plate 2 | Plate 1 | Plate 2 | Plate 1 | Plate 2 |
| 1 | 120.86 | 120.49 | 1.000 | 1.007 | 1.000 | 1.159 | 1.000 | 1.958 |
| 2 | 177.90 | 190.93 | 0.963 | 0.986 | 1.016 | 1.160 | 1.294 | 2.260 |
| 3 | 220.12 | 221.22 | 0.697 | 0.731 | 0.654 | 0.715 | 0.628 | 0.942 |

Table 5.4: Computed $\zeta_{\mathit{eff}}$ results for both the plates. The uncut plate is denoted as "Plate 1" and the slotted plate is denoted as "Plate 2". For comparison purposes, the $\zeta_{\mathit{eff}}$ values are normalized with respect to the first vibration mode of the uncut plate (Plate 1) for each $m$.

## 5.7 Summary

In this chapter, we have demonstrated how the distortional strain energy based damping formula can be used in finite element computations of modal damping ratios using both solid and shell elements in ANSYS. We have verified our finite element computations with several analytical results.

We have used a normalization, within the damping computation, with respect to the average volumetric strain energy density such that the $\zeta_{\mathit{eff}}$ values are size independent.

Finally, we have shown, with a computational example, that stress concentrations within a material can increase the damping values. For materials with higher $m$, a significant improvement in damping can be achieved with the introduction of stress concentrations. That stress concentrations improve damping for materials with $m > 2$ is not a fundamentally new observation; it was mentioned in passing in Mallik and Ghosh (1973). However, our detailed computational check of the same, for an object of complex shape, is presented both for completeness as well as suggested direction for more practical design oriented investigations in the future.

# Chapter 6

# Conclusions

In this thesis, we have developed multiaxial damping formulas based on assumed underlying micromechanical models of internal dissipation. Guided by empirical evidence, we have considered two mathematically simple rate-independent dissipative phenomena: (i) Coulomb friction, and (ii) ambient-temperature plasticity. In our first model, we have considered dissipation due to randomly distributed frictional microcracks embedded inside the solid body. We have used Monte Carlo averaging for calculating the net dissipation and developed a single empirically fitted dissipation formula valid over a useful range of the friction coefficient. We have also shown how this formula can be used in a three dimensional setting to compute an effective measure of damping in any arbitrarily shaped solid object.

In the second model, we have considered dissipation due to a multitude of randomly distributed microscopic elasto-plastic flaws. We have used finite element simulations in ABAQUS to study the deformation and dissipation in these flaws under far-field loading (both monotonic and cyclic). We have also developed a semi-analytical calculation based on Eshelby's (1957) formulas for ellipsoidal flaws. We have found two simple special cases for which the plastic dissipation is governed by a well-defined scalar quantity. When the flaw is spherical the dissipation is governed by the second deviatoric stress invariant ($J_2$), which is proportional to the distortional strain energy. For this case, our averaged dissipation over random flaw distributions results in a purely distortional strain energy based damping formula. In the other special case, namely a flat and thin ellipsoidal flaw, the dissipation is governed by the resolved shear stress applied parallel to the near-flat surface of the ellipsoid. Somewhat surprisingly, upon averaging over all possible flaw plane orientations, the resulting dissipation formula for this case shows simple and near-exact dependence on the distortional strain energy for about $2 \leq m \leq 6$. Therefore, we have suggested that for practical engineering design purposes, and for those materials for which $m$ is not too large, a distortional strain energy based dissipation formula might be reasonable. Academically, an important contribution of this elasto-plastic flaw based formula is that it incorporates the triaxiality of the stress states starting from some underlying micromechanics as opposed to prior *ad hoc* proposals, although the final recommendation turns out to be based on a simple stress invariant.

The distortional strain energy based formula is finally used for finite element computations of modal damping ratios of lightly damped objects of arbitrary shape. We have used both solid and shell elements in ANSYS for the computation and obtained accurate results as demonstrated by comparison against available analytical formulas.

For $m \geq 2$ in the damping power law, we have used normalization based on the average volumetric strain energy density, so as to obtain results that depend on shape but not on size. We have also shown that introduction of stress concentrations in the material can, at least in some cases, significantly increase the damping values.

We note that the damping models we have developed in this thesis have fitted material constants: $C$ and $\mu$ in the frictional microcrack based model and $\xi$ in the model due to elasto-plastic flaws. These fitted constants have to be obtained from experimental data. In all our damping calculations, we have used some normalized values and studied our results. However, in practical cases the actual fitted values of these material constants, obtained from suitable experiments, should be used for exact quantification of the damping results.

As a final comment, in this thesis we have presented a complete analysis procedure of modal damping values for any arbitrarily shaped solid body starting from the development of a multiaxial damping model to the finite element formulation. We hope that such damping computation using multiaxial damping formula might eventually be built into commercial finite element codes, so that modal damping values could be computed and compared routinely along with natural frequencies and mode shapes.

# Appendix A

# Supplementary materials for Chapter 2

## A.1 On possible waveforms within the dissipation calculation

The dissipation simulation results from ABAQUS, and the subsequently used single spring-block based formula, both hold for a variety of periodic stress histories provided (i) the *changes* in far-field normal and shear stresses maintain a fixed proportion throughout the load cycle (i.e., the time-varying parts have similar waveforms), and (ii) there are only two points of stress reversal per cycle. Many waveforms are allowed within these restrictions. For example, the waveforms shown in (a), (b), and (c) within Fig. A.1 are allowed but (d) is not allowed because it has more than two points of stress reversal per cycle.

## A.2 Simulation results from 2D finite element analysis

Finite element simulations were carried out in ABAQUS Standard, version 6.9. In the finite element mesh, 4-node bilinear plane stress quadrilateral elements (CPS4) were used. The domain is 10 mm × 10 mm (the out-of-plane thickness is specified as 2 mm), the crack is 1 mm long, and contact is “hard” (no artificial numerical contact compliance). Since the material is assumed elastic, the Young’s modulus $E$ used only scales the result by a constant; here, we arbitrarily took $E = 210$ GPa and

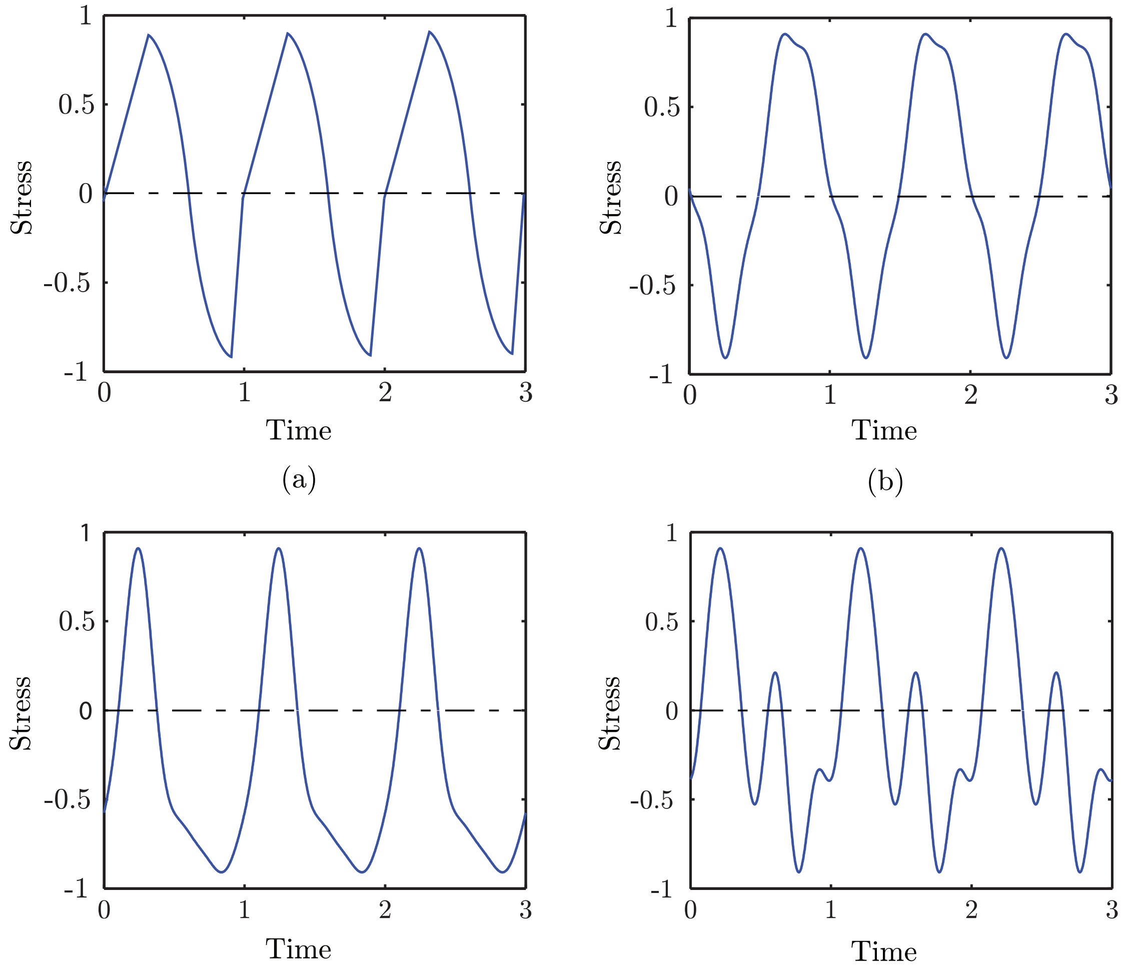

(a) (b) (c) (d)

Figure A.1: Some waveforms: (a), (b), (c) are allowed, but (d) is not. The scale is arbitrary, for both stress and time.

Poisson's ratio $\nu = 0.3$. The energy dissipation was computed using pseudostatic simulation. Refinement of both mesh size in space and load steps in time showed convergence. Figure A.2 shows an intermediate mesh: the final results below used a finer mesh. Figures A.3 and A.4 show typical results from the convergence study. Several load cases were run with different values of stress amplitudes as well as the friction coefficient $\mu$, and the results are given in Table A.1.

We mention that extreme refinement near the crack tip is not necessary to obtain a useful value for the dissipation. The crack tip stress singularity even with Coulomb friction is like $1/\sqrt{r}$ (see, e.g., Xiaomin (1994)), and so errors are triply small: small

| $\mu$ | $\tau_a$ (MPa) | $\sigma_a$(MPa) | $\beta = \left(\dfrac{\sigma_m}{\sigma_a}\right)$ | $\alpha = \left(\dfrac{\tau_m}{\tau_a}\right)$ | Dissipation (N-mm) |
|---|---|---|---|---|---|
| 0.3 | 70 | 30 | 0.4 | 0 | 0.0142 |
| 0.3 | 70 | 30 | 0.4 | 1.2 | 0.0142 |
| 0.5 | 90 | 40 | 0.6 | 0 | 0.0439 |
| 0.5 | 90 | 40 | 0.6 | 0.4 | 0.0439 |
| 0.4 | 100 | 50 | 0.6 | 0 | 0.0512 |
| 0.3 | 100 | 30 | 1.1 | 0 | 0.0496 |
| 0.3 | 80 | 30 | 0.6 | 0 | 0.0220 |
| 0.3 | 140 | 100 | 0 | 0 | 0.0406 |
| 0.3 | 140 | 80 | 0 | 0 | 0.0355 |
| 0.3 | 160 | 120 | 0 | 0 | 0.0545 |
| 0.3 | 100 | 100 | 0 | 0 | 0.0241 |
| 0.3 | 170 | 110 | 0 | 0 | 0.0566 |
| 0.3 | 40 | 100 | 0 | 0 | 0.0025 |
| 0.3 | 50 | 100 | 0 | 0 | 0.0055 |
| 0.3 | 180 | 200 | 0 | 0 | 0.0808 |
| 0.35 | 120 | 90 | 1 | 0 | 0.1327 |
| 0.4 | 110 | 60 | 0.4 | 0 | 0.0498 |
| 0.4 | 100 | 40 | 1.2 | 0 | 0.0828 |
| 0.4 | 100 | 100 | 1.2 | 0 | 0.1187 |
| 0.4 | 120 | 70 | −0.4 | 0 | 0.0112 |
| 0.4 | 110 | 100 | 0 | 0 | 0.0306 |
| 0.4 | 60 | 100 | 0 | 0 | 0.0071 |
| 0.4 | 70 | 100 | 0 | 0 | 0.0113 |
| 0.4 | 80 | 100 | 0 | 0 | 0.0159 |
| 0.4 | 90 | 100 | 0 | 0 | 0.0206 |
| 0.4 | 190 | 200 | 0 | 0 | 0.0927 |
| 0.45 | 95 | 75 | 1 | 0 | 0.0916 |
| 0.5 | 80 | 40 | 0.4 | 0 | 0.0281 |
| 0.5 | 80 | 60 | 1.1 | 0 | 0.0715 |
| 0.5 | 110 | 80 | −0.2 | 0 | 0.0196 |
| 0.5 | 160 | 110 | 0 | 0 | 0.0643 |
| 0.5 | 170 | 190 | 0 | 0 | 0.0684 |
| 0.5 | 80 | 60 | 2.57 | 0 | 0.0113 |
| 0.5 | 80 | 60 | 2.45 | 0 | 0.0264 |
| 0.5 | 80 | 60 | −1.1 | 0 | 0.0000 |
| 0.5 | 80 | 60 | −0.6 | 0 | 0.0026 |
| 0.5 | 80 | 60 | 0 | 0 | 0.0163 |
| 0.5 | 80 | 60 | 0.3 | 0 | 0.0276 |
| 0.5 | 80 | 60 | 1.4 | 0 | 0.0812 |
| 0.5 | 80 | 60 | 2.2 | 0 | 0.0521 |
| 0.5 | 80 | 60 | 2.5 | 0 | 0.0203 |
| 0.5 | 80 | 60 | 2.66 | 0 | 0.0000 |

Table A.1: Dissipation results for various cases in the two-dimensional finite element analysis. The first 4 rows show that the mean value of the shear stress does not affect the dissipation per cycle.

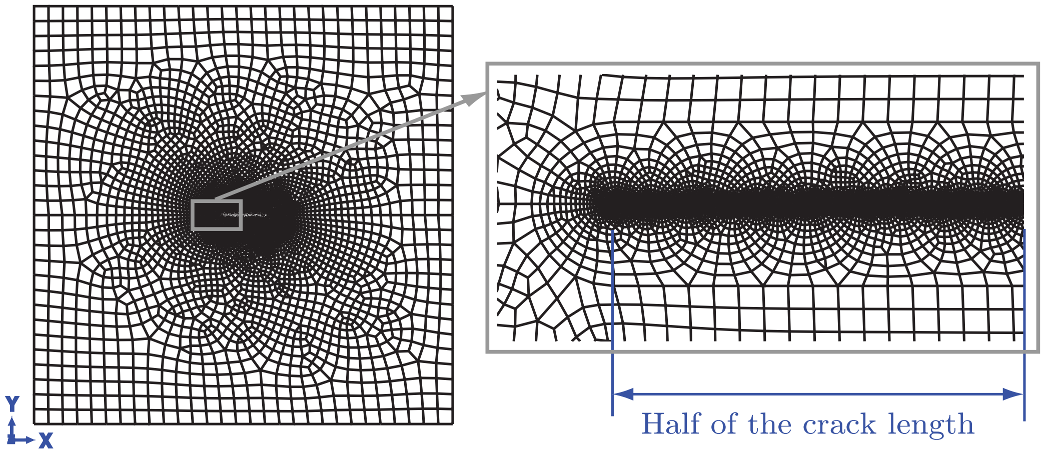

Figure A.2: Finite element mesh of the 2D model. A small region is shown enlarged. The rectangles and the arrow were drawn in later, manually and approximately, for visualization.

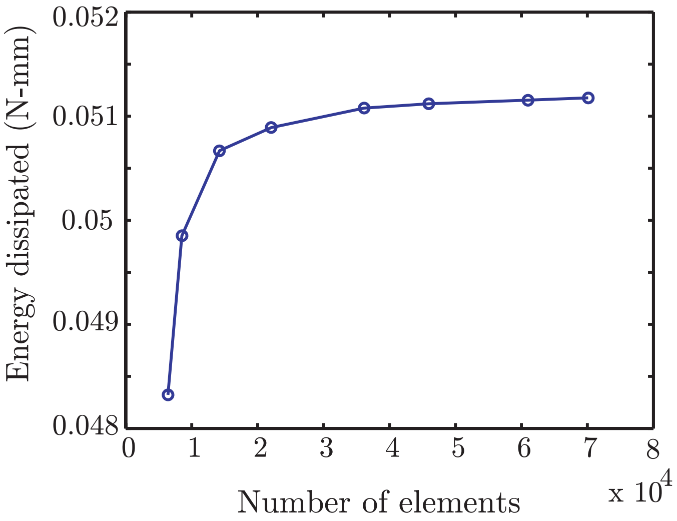

Figure A.3: Mesh convergence for a particular load case (fifth row of table A.1) using 200 time steps in the loading cycle.

errors due to moderate refinement in the small-sliding ($\sqrt{r}$) dissipations in a small region near the crack tip add up to very little overall error. For this reason, the finite element results are accurate enough for our purposes.

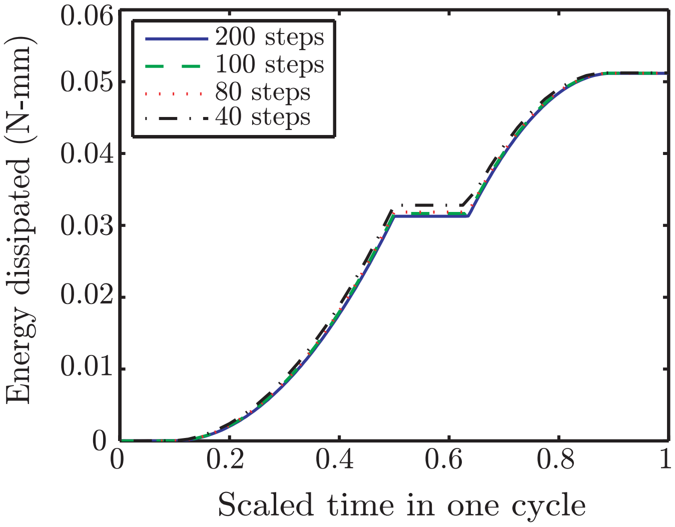

Figure A.4: Effect of changing the number of time steps used.

## A.3 The dissipation formula from the spring block model

We consider the spring and massless-block model of Fig. A.5. If the normal stress $\sigma$ becomes tensile, there is no dissipation; for compressive $\sigma$, there is Coulomb friction as indicated. Several distinct cases occur, for which individual dissipation formulas are presented below. All these cases can be collected into a single formula containing logical variables. In all these formulas, the mean shear stress $\tau_m$ plays no role, because it affects the mean position of the block but not the steady state cyclic dissipation.

As indicated in Fig. A.5, $\tau_a$ is the amplitude of the tangential loading, $\sigma_a$ is the amplitude of normal loading, $\sigma_m$ is the mean value of normal loading (compressive taken as positive), and $\mu$ is the coefficient of friction. We define the following non-dimensional ratios

$$\zeta = \frac{\tau_a}{\sigma_a} \quad \text{and} \quad \beta = \frac{\sigma_m}{\sigma_a}.$$

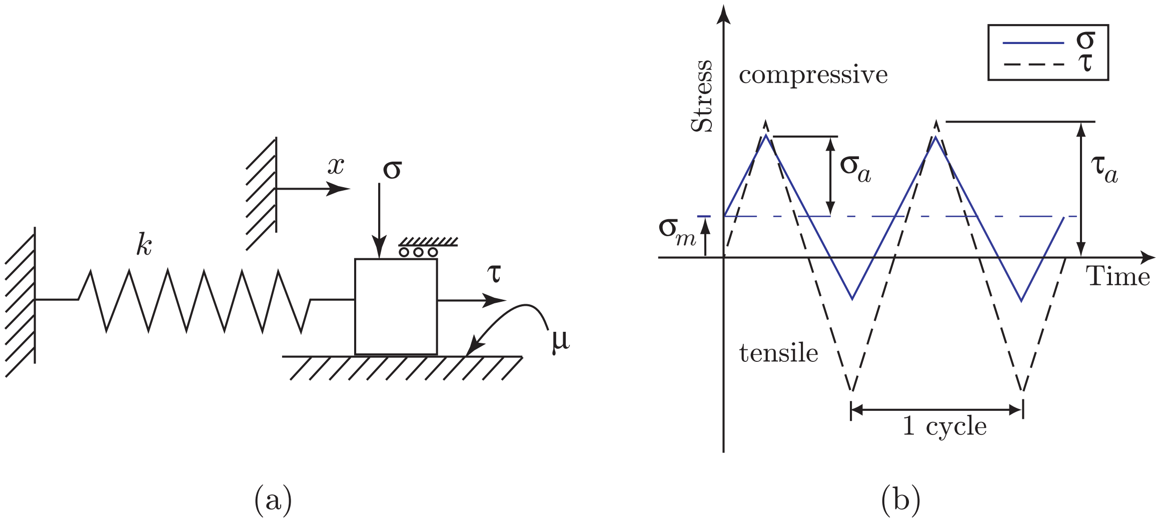

(a) (b)

Figure A.5: (a) A spring block system under periodic normal and tangential load. (b) Applied normal and shear loads. Note the sign convention: compressive mean normal stress is positive.

### A.3.1 Case 1: zero mean normal stress ($\beta = 0$)

In each load cycle, the crack closes when the normal stress is compressive, and opens when it is tensile. When the crack opens, prior loading history effects disappear. Upon crack closure, sliding (and hence energy dissipation) occurs only if $\tau_a > \mu\sigma_a$ (or $\zeta > \mu$). The steady cyclic energy dissipation for this case can be shown to be

$$D = [\zeta > \mu] \times C\sigma_a^2\mu\zeta \left\{ \frac{\zeta - \mu}{\zeta + \mu} \right\}, \tag{A.1}$$

where $C$ is a constant depending on the stiffness; and where the square brackets denote a logical variable, taking the value 1 if the inequality holds and 0 otherwise.

### A.3.2 Case 2: $-1 < \beta < 1$

The case of $-1 < \beta < 1$ is similar to that of case 1, in that the crack opens and closes once in each cycle. The dissipation can be computed using the foregoing result by noting that the instant of crack closure can be used as a reference point, and subsequent stress increments until the next crack opening can be treated in the same way as in Case 1 above. The net result is

$$D = [\zeta > \mu] \times [-1 < \beta < 1] \times C\sigma_a^2 \mu\zeta \left\{ (1+\beta)^2 \frac{\zeta - \mu}{\zeta + \mu} \right\}, \tag{A.2}$$

where putting $\beta = 0$ recovers Case 1.

### A.3.3 Case 3: $\beta < -1$

For $\beta < -1$ the crack remain always open and there is no dissipation.

### A.3.4 Case 4: $\beta > 1$

If $\beta > 1$, then the crack never opens. It can be shown that, starting from zero displacements, the cyclic state is reached in one forcing cycle. To obtain a formula for the steady state cyclic dissipation, the displacement at the instant of minimum compression is first assumed to be some $x_0$; then subsequent displacements are computed over one cycle; and the final displacement is set equal to $x_0$ again. Upon solving for $x_0$, the dissipation per cycle can be easily calculated. It is

$$D = [\zeta > \mu] \times C\sigma_a^2 \mu\zeta \left\{ (1+\beta)^2 \frac{\zeta - \mu}{\zeta + \mu} - (\beta - 1)^2 \frac{\zeta + \mu}{\zeta - \mu} \right\}. \tag{A.3}$$

The above formula holds for $\beta < \dfrac{\zeta}{\mu}$, beyond which there is no cyclic dissipation.

### A.3.5 Single formula

All the foregoing results can be combined into one formula as follows:

$$D = [\beta < \frac{\zeta}{\mu}] \times [\zeta > \mu] \times [\beta > -1] \times C\sigma_a^2 \mu\zeta \left\{ (1+\beta)^2 \frac{\zeta - \mu}{\zeta + \mu} - [\beta > 1](\beta - 1)^2 \frac{\zeta + \mu}{\zeta - \mu} \right\}, \tag{A.4}$$

which involves a single load-independent and friction-independent fitted coefficient $C$.

## A.4 Simulation results from 3D finite element analysis

The dissipation formula of Eq. (2.3) was verified using 3D finite element simulations of a circular and a triangular crack. Some details of those simulations are presented below.

### A.4.1 Circular crack

A cube of 10 mm edge length was considered, with a central circular crack of 1 mm radius. 10-noded tetrahedral elements were used to discretize the volume. Using symmetry, one half of the system was analyzed. The bottom half of that half is shown in Fig. A.6.

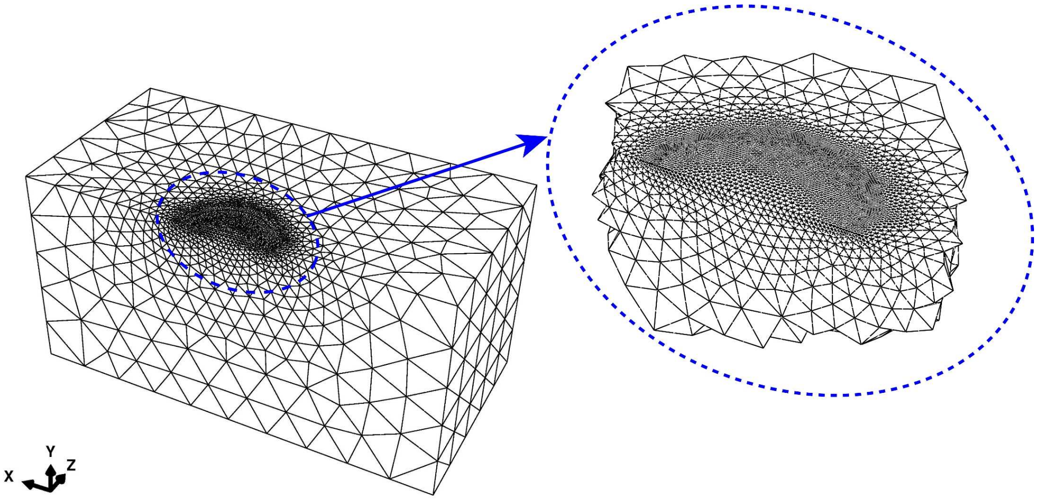

Figure A.6: One half of the 3D finite element mesh with circular crack.

Figures A.7 and A.8 show typical results from a convergence study. Note, however, that we have used an irregular mesh, and the mesh refinement was not done by some rational quantifiable criteria, but rather by manual (mouse-driven) selection of regions within the mesh by a human user. As a result, the convergence against number of elements $N$ need not show a well defined function. Nevertheless, an empirical fit was attempted, and the resulting extrapolated value for $N \to \infty$ was within 1 percent of the dissipation calculated with our most refined mesh.

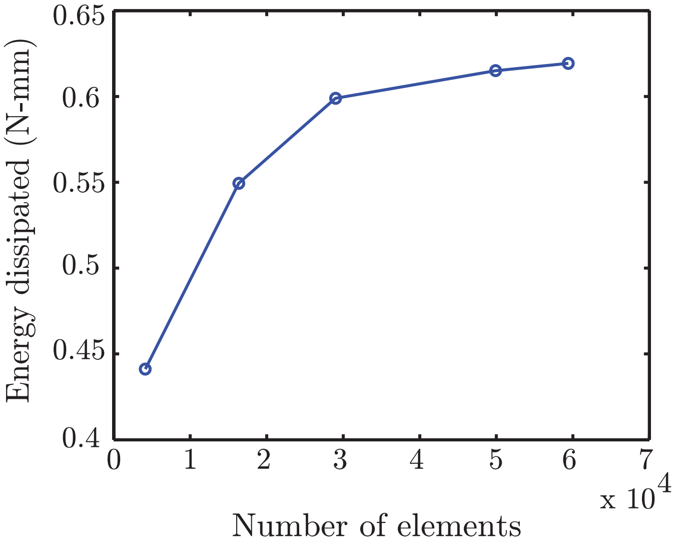

Figure A.7: Convergence study for the circular crack. Mesh refinement, using 100 time steps in the loading cycle. The largest number of solid elements used was 59,410. The dissipation values are fitted fairly well (empirically) by a curve of the form $a_0 + \frac{a_1}{N^2} + \frac{a_2}{N^3}$, where $N$ is the number of elements. The limiting value, $a_0$, matches the last computed value to within about 1 percent, and so further refinement was not attempted.

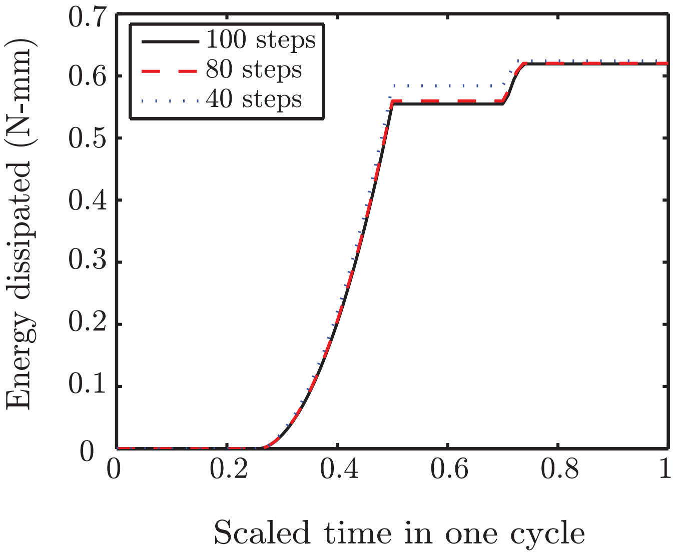

Figure A.8: Effect of changing the number of time steps used. Since convergence of the final dissipated amount was rapid, and the computation was slow, more than 100 steps within the cycle were not used.

Various loading cases were simulated and are shown in Table A.2. The computed dissipation results from the finite element simulations were compared with Eq. (2.3) above. Figure A.9 shows the results obtained, and the match is excellent.

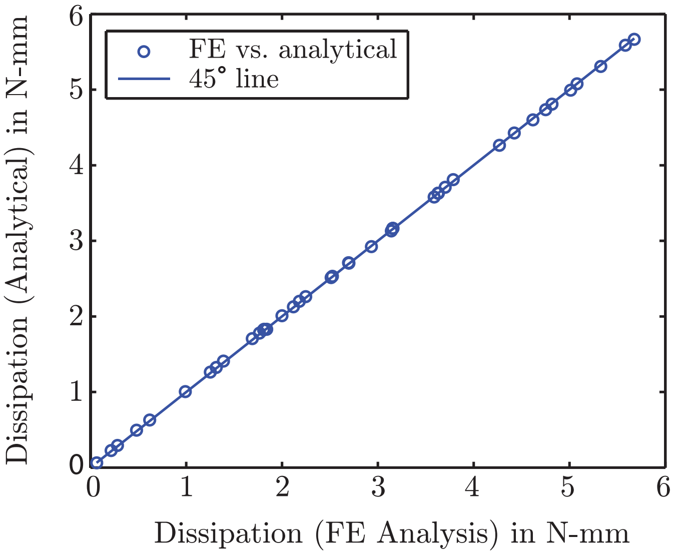

Figure A.9: Analytical formula for dissipation against computed value from finite element (FE) simulation (with one fitted constant $C$) for the circular crack. The numbers are larger than for the 2D computations because the stresses used here are larger; note, however, that the material is linearly elastic and stress magnitudes are notional.

### A.4.2 Triangular crack

For the triangular crack, the analysis procedures and the overall dimensions of the cubic cell were the same as for the circular crack case, only the crack was here an isoceles triangle of base 2 mm and height 2 mm. Using symmetry, one half of the system was analyzed. The bottom half of that half is shown in Fig. A.10. The number of solid elements used was 53,499, and a systematic convergence study was not carried out.

Various loading cases were simulated and are shown in Table A.3. The computed dissipation results from the finite element simulations were compared with Eq. (2.3) above. Figure A.11 shows the results obtained, and the match is excellent.

| $\mu$ | $\tau_a$ (MPa) | $\sigma_a$(MPa) | $\beta = \left(\dfrac{\sigma_m}{\sigma_a}\right)$ | $\alpha = \left(\dfrac{\tau_m}{\tau_a}\right)$ | Dissipation (N-mm) |
|---|---|---|---|---|---|
| 0.2 | 1100 | 1000 | 0 | 0 | 2.0002 |
| 0.2 | 1100 | 1000 | 0 | 0.4 | 1.9997 |
| 0.3 | 1400 | 1000 | 0 | 0 | 3.5870 |
| 0.3 | 1400 | 800 | 0 | 0 | 3.1418 |
| 0.3 | 1600 | 1200 | 0 | 0 | 4.8161 |
| 0.3 | 1000 | 1000 | 0 | 0 | 2.1160 |
| 0.4 | 500 | 1000 | 0 | 0 | 0.2822 |
| 0.4 | 600 | 1000 | 0 | 0 | 0.6193 |
| 0.2 | 1100 | 800 | 0.3 | 0 | 2.9342 |
| 0.4 | 700 | 1000 | 0 | 0 | 0.9909 |
| 0.4 | 800 | 1000 | 0 | 0 | 1.3891 |
| 0.4 | 1000 | 1000 | 0 | 0 | 2.2460 |
| 0.4 | 1100 | 1000 | 0 | 0 | 2.6960 |
| 0.3 | 800 | 10 | 0.4 | 0 | 0.0641 |
| 0.4 | 1200 | 1000 | 0 | 0 | 3.1566 |
| 0.4 | 1300 | 1000 | 0 | 0 | 3.6265 |
| 0.5 | 1600 | 1100 | 0 | 0 | 5.6768 |
| 0.4 | 1100 | 1000 | 0.4 | 0 | 5.3253 |
| 0.5 | 1000 | 1000 | 0 | 0 | 2.1828 |
| 0.5 | 1300 | 800 | 0 | 0 | 3.6301 |
| 0.5 | 900 | 900 | 0 | 0 | 1.7645 |
| 0.2 | 1300 | 1000 | 0 | 0 | 2.5135 |
| 0.2 | 1400 | 1600 | 0 | 0 | 3.7009 |
| 0.2 | 800 | 1000 | 0 | 0 | 1.2498 |
| 0.2 | 900 | 800 | 0 | 0 | 1.3148 |
| 0.3 | 1200 | 900 | 0 | 0 | 2.6988 |
| 0.3 | 1700 | 1100 | 0 | 0 | 5.0128 |
| 0.3 | 400 | 1000 | 0 | 0 | 0.2151 |
| 0.4 | 600 | 1000 | 0.7 | 0 | 1.8383 |
| 0.3 | 500 | 1000 | 0 | 0 | 0.4796 |
| 0.6 | 1500 | 1100 | 0 | 0 | 5.0804 |
| 0.6 | 1200 | 1000 | 0 | 0 | 3.1555 |
| 0.45 | 900 | 900 | 0 | 0 | 1.8072 |
| 0.25 | 1300 | 2000 | 0 | 0 | 3.7867 |
| 0.35 | 1430 | 1290 | 0 | 0 | 4.4251 |
| 0.35 | 1600 | 950 | 0 | 0 | 4.6179 |
| 0.35 | 1600 | 1000 | 0 | 0 | 4.7496 |
| 0.45 | 1400 | 1000 | 0 | 0 | 4.2683 |
| 0.55 | 1700 | 1900 | 0 | 0 | 5.5847 |
| 0.55 | 900 | 900 | 0 | 0 | 1.6910 |

Table A.2: Dissipation results for various load cases: flat circular crack. The first 2 rows show that the mean value of the shear stress does not affect the dissipation per cycle.

| $\mu$ | $\tau_a$ (MPa) | $\sigma_a$(MPa) | $\beta = \left(\dfrac{\sigma_m}{\sigma_a}\right)$ | $\alpha = \left(\dfrac{\tau_m}{\tau_a}\right)$ | Dissipation (N-mm) |
|---|---|---|---|---|---|
| 0.2 | 800 | 1000 | 0 | 0 | 0.5538 |
| 0.2 | 800 | 1000 | 0 | 0.4 | 0.5536 |
| 0.4 | 1000 | 1000 | 0 | 0 | 0.9971 |
| 0.4 | 1000 | 1000 | 0 | 0.4 | 0.9968 |
| 0.2 | 900 | 800 | 0 | 0 | 0.5834 |
| 0.2 | 1100 | 800 | 0.3 | 0 | 1.3077 |
| 0.2 | 1400 | 1600 | 0 | 0 | 1.6494 |
| 0.3 | 500 | 1000 | 0 | 0 | 0.2103 |
| 0.3 | 800 | 1000 | 0.4 | 0 | 1.2506 |
| 0.3 | 1000 | 400 | 0 | 0 | 0.5508 |
| 0.3 | 1400 | 1000 | 0 | 0 | 1.5981 |
| 0.3 | 1600 | 1200 | 0 | 0 | 2.1478 |
| 0.4 | 500 | 1000 | 0 | 0 | 0.1222 |
| 0.4 | 600 | 1000 | 0 | 0 | 0.2722 |
| 0.4 | 600 | 1000 | 0.7 | 0 | 0.8148 |
| 0.4 | 700 | 1000 | 0 | 0 | 0.4375 |
| 0.4 | 700 | 900 | 0.3 | 0 | 0.7951 |
| 0.4 | 800 | 1000 | 0 | 0 | 0.6150 |
| 0.4 | 1100 | 1000 | 0.4 | 0 | 2.3731 |
| 0.4 | 1200 | 700 | $-0.4$ | 0 | 0.4346 |
| 0.5 | 900 | 900 | 0 | 0 | 0.7824 |
| 0.5 | 1100 | 800 | $-0.2$ | 0 | 0.7631 |
| 0.5 | 1300 | 800 | 0 | 0 | 1.6159 |
| 0.6 | 1500 | 1100 | 0 | 0 | 2.2634 |
| 0.3 | 1300 | 1000 | 0 | 0 | 1.4303 |
| 0.42 | 1300 | 1100 | 0 | 0 | 1.6746 |
| 0.48 | 1200 | 800 | 0 | 0 | 1.3904 |
| 0.5 | 1500 | 900 | 0 | 0 | 2.1401 |
| 0.57 | 1400 | 1000 | 0 | 0 | 1.9743 |
| 0.35 | 1100 | 900 | 0 | 0 | 1.1227 |
| 0.33 | 1400 | 1400 | 0 | 0 | 1.9110 |

Table A.3: Dissipation results for various load cases: flat triangular crack. The first 4 rows show that the mean value of the shear stress does not affect the dissipation per cycle.

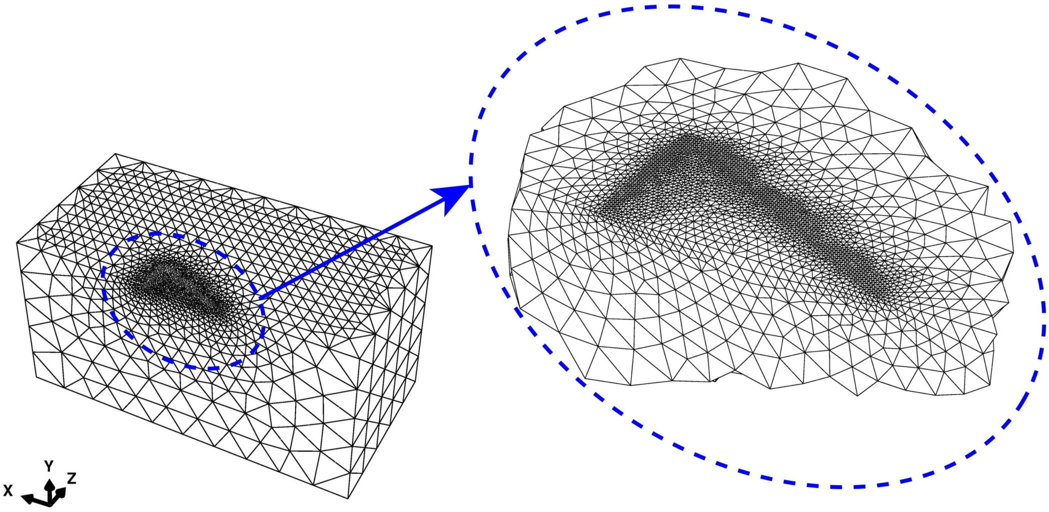

Figure A.10: One half of the 3D finite element mesh with a triangular crack.

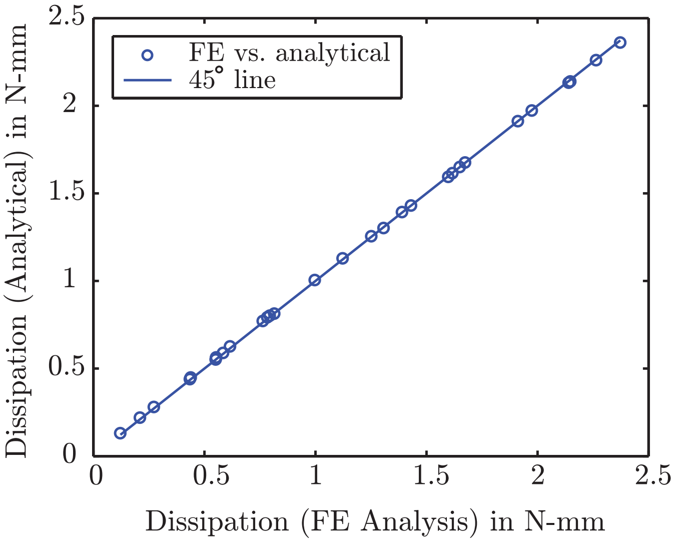

Figure A.11: Analytical formula for dissipation against computed value from finite element (FE) simulation (with one fitted constant $C$). The crack is an isoceles triangle.

## A.5 Matrix B for the constitutive model

For Eq. (2.11), the fitted matrix **B** was found to be

$$\mathbf{B} = \begin{bmatrix} 0.0502 & -0.2919 & 1.4014 & -2.2672 & 1.2207 \\ -0.2404 & 1.1032 & -8.5528 & 15.6248 & -8.8444 \\ 0.9590 & -1.9703 & 19.1510 & -37.1280 & 22.1110 \\ -1.3023 & 1.7092 & -18.3802 & 37.1835 & -23.2254 \\ 0.5354 & -0.5540 & 6.3899 & -13.4358 & 8.7562 \\ -0.1639 & 0.2904 & -2.4921 & 5.2895 & -3.4713 \\ 1.4849 & -1.5920 & 22.4593 & -53.7902 & 37.0354 \\ -4.4902 & 5.6752 & -70.7569 & 170.3431 & -117.5853 \\ 5.0411 & -8.3716 & 88.1836 & -208.9717 & 143.4247 \\ -1.8201 & 3.9436 & -37.2935 & 87.0923 & -59.4126 \\ 0.2007 & -0.3217 & 3.4993 & -8.2660 & 5.6588 \\ -1.8590 & 3.0802 & -34.4736 & 84.1598 & -58.3400 \\ 5.0382 & -11.5023 & 111.2467 & -266.1229 & 182.3608 \\ -5.0664 & 16.2774 & -139.9197 & 326.2059 & -220.4225 \\ 1.6216 & -7.4579 & 59.4630 & -135.8272 & 90.6983 \\ -0.0755 & 0.1573 & -1.6178 & 3.8573 & -2.6340 \\ 0.6723 & -1.6798 & 15.9470 & -38.2460 & 26.1804 \\ -1.6712 & 5.9580 & -50.6344 & 118.6870 & -80.1494 \\ 1.5056 & -8.0587 & 62.8622 & -143.7174 & 95.6099 \\ -0.4069 & 3.5941 & -26.4779 & 59.3444 & -38.9797 \end{bmatrix}. \tag{A.5}$$

## A.6 Brief review of some topics in vibration theory

### A.6.1 Response of a typical damped harmonic oscillator

Consider the lightly damped harmonic oscillator

$$\ddot{x} + 2\zeta\dot{x} + x = \sin\omega t. \tag{A.6}$$

The steady state response amplitude is $\dfrac{1}{\sqrt{(1-\omega^2)^2 + 4\zeta^2\omega^2}}$, which is plotted in Fig. A.12. It is seen that small damping has a sensible effect on the response only close to resonance.

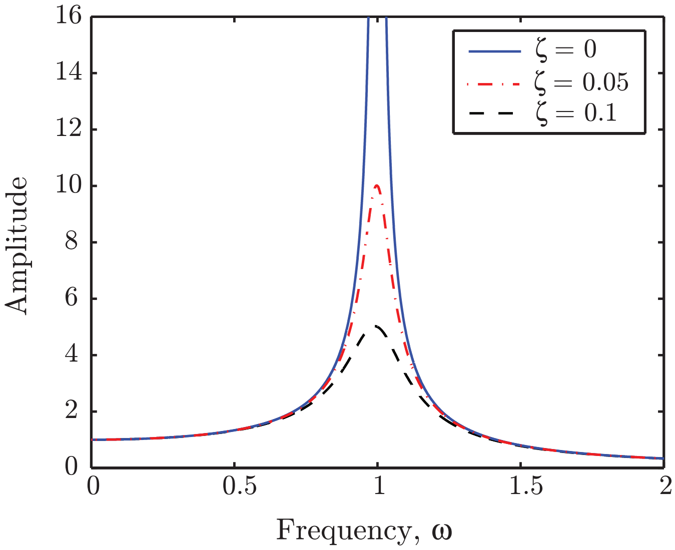

Figure A.12: Response of the damped oscillator in Eq. (A.6).

### A.6.2 Modal damping

In the commonest version of linear vibration theory, we work with discrete systems of the form

$$M\ddot{x} + C_d\dot{x} + Kx = f, \tag{A.7}$$

where overdots denote time derivatives, lower case symbols denote $n \times 1$ column matrices, upper case symbols denote $n \times n$ matrices, $M = M^T > 0$ (symmetric positive definite; no confusion with $\mathbf{M}$ of Eq. (2.11)), $K = K^T \geq 0$ (symmetric positive semidefinite), and $C_d = C_d^T \geq 0$ as well.

The unforced and undamped system is

$$M\ddot{x} + Kx = 0. \tag{A.8}$$

Assembling the (guaranteed real) eigenvectors of the system in a matrix $\Phi$, it is shown in elementary textbooks that $\Phi^T M \Phi$ can be chosen (by scaling) to be the identity matrix $I$, for which choice

$$\Phi^T K \Phi = \Lambda,$$

a diagonal matrix whose diagonal elements are the squares of the natural frequencies.

Considering the unforced but damped system, however, if $C_d$ has no special structure then the system has complex eigenvectors (the structure, even when vibrating in a single mode, does not have all parts of it moving perfectly in phase).

In the special case where the real eigenvectors of the undamped system also diagonalize the damping matrix $C_d$, the damped system continues to have real eigenvectors. In such cases, staying within real arithmetic, the system can be diagonalized and the responses of individual modes can be studied independently. In many applications, it is routine to assume that $C_d$ can be so diagonalized. Examples lie in experimental modal analysis, and in estimating the responses of some structures under arbitrary loading (where the investigators might, e.g., assume 2 percent damping uniformly for all modes).

Academically, it remains to ask what matrices $C_d$ can be so diagonalized. A restricted answer is

$$C_d = \alpha_0 M + \alpha_1 K,$$

commonly called proportional damping, which is itself a special case of

$$C_d = M \sum_{i=0}^{n-1} \alpha_i (M^{-1}K)^i = \alpha_0 M + \alpha_1 K + \alpha_2 K M^{-1} K + \cdots + \alpha_{n-1} K (M^{-1}K)^{n-2}. \quad \text{(A.9)}$$

The representation of Eq. (A.9) is well known (see e.g., Adhikari (2001)). Retention of higher powers of $M^{-1}K$ adds no modeling benefit because of the Cayley-Hamilton theorem.

Note that the above representation is in the end merely a convenient matrix-algebra trick: it has no physical basis. After all, the linear viscous damping model is already invalidated by the observed frequency-independence of per-cycle dissipation (Lord Kelvin, 1865; and many others after him).

The linear viscous damping model continues to be widely used in engineering models, however, especially for lightly-damped structures. This is both for convenience as well as the fact that small damping is only important near resonance anyway (see above), and in near-resonance responses merely matching the energy dissipated per cycle may meet many modeling goals.

The net result is that, provided the energy dissipation in each individual mode is correctly captured by whatever equivalent damping ratio we are using in our model, further details of the damping become irrelevant for many practical purposes.

With this background motivation, assume (for convenience or simplicity) that $C_d$ can in fact be diagonalized as above. Let us now consider modal coordinates $q$ such that $x = \Phi q$. Equation (A.7) becomes

$$M\Phi\ddot{q} + C_d\Phi\dot{q} + K\Phi q = f, \tag{A.10}$$

or

$$\Phi^T M\Phi\ddot{q} + \Phi^T C_d\Phi\dot{q} + \Phi^T K\Phi q = \Phi^T f, \tag{A.11}$$

or (as discussed above)

$$I\ddot{q} + D_d\dot{q} + \Lambda q = \bar{f}, \tag{A.12}$$

where $D_d$ is a diagonal matrix by assumption. The decoupled equations now look like

$$\ddot{q}_i + d_i\dot{q}_i + \omega_i^2 q_i = \bar{f}_i, \tag{A.13}$$

where $\omega_i$ is the $i^{\text{th}}$ natural frequency, $d_i$ is the $i^{\text{th}}$ diagonal element of $D_d$, and $\bar{f}_i$ can be called the $i^{\text{th}}$ modal forcing. For simplest interpretation, we usually write

$$d_i = 2\zeta_i\omega_i, \tag{A.14}$$

where $\zeta_i$ is the $i^{\text{th}}$ nondimensional damping ratio. In applied work (e.g., simulations of automotive components in industrial design), $\zeta_i$ is often estimated or even arbitrarily specified in simulation, e.g., "$\zeta_i = 0.02$ for all $i$". That is, one works with effective modal damping values, usually small values, without regard to the source of the damping. The fact that damping plays a significant role only close to resonance makes this a reasonable approach in many cases.

Finally, if we have a way (as explained in Chapter 2) of considering the modes one by one; of assuming that the structure has a response dominated by that mode; and then of estimating its equivalent damping ratio $\zeta_i$; then we have $D_d$ by Eq.

(A.14). We then automatically have

$$C_d = \Phi^{-T} D_d \Phi^{-1}, \tag{A.15}$$

should we need it. *Not* assuming that $C_d$ is diagonalizable as above would lead to greater modeling complications and numerical difficulties, with doubtful incremental benefits.

# Appendix B

# Supplementary materials for Chapter 3

## B.1 Eshelby tensor for an ellipsoidal inclusion

We present below the formula for calculating the Eshelby tensor for a general ellipsoidal inclusion. For details of this formula, see Mura (1987).

For an ellipsoidal inclusion described by $\dfrac{x^2}{a_1^2} + \dfrac{y^2}{a_2^2} + \dfrac{z^2}{a_3^2} \leq 1$ with $a_1 > a_2 > a_3$, we denote

$$F(\theta, k) = \int_0^{\theta} \frac{dw}{\sqrt{1 - k^2 \sin^2 w}},$$

and

$$E(\theta, k) = \int_0^{\theta} \sqrt{1 - k^2 \sin^2 w}\, dw,$$

where we define $\theta = \sin^{-1}\sqrt{1 - \dfrac{a_3^2}{a_1^2}}$, and $k = \sqrt{\dfrac{a_1^2 - a_2^2}{a_1^2 - a_3^2}}$.

We now define $I_i$ and $I_{ij}$ values as follows (no confusion with $I_1$, $I_2$ and $I_3$ for the first, second, and third stress invariants respectively).

$$\begin{aligned}
I_1 &= \frac{4\pi a_1 a_2 a_3}{(a_1^2 - a_2^2)\sqrt{a_1^2 - a_3^2}} \left(F(\theta, k) - E(\theta, k)\right) \\
I_3 &= \frac{4\pi a_1 a_2 a_3}{(a_1^2 - a_2^2)\sqrt{a_1^2 - a_3^2}} \left(\frac{a_2\sqrt{a_1^2 - a_3^2}}{a_1 a_3} - E(\theta, k)\right) \\
I_2 &= 4\pi - I_1 - I_3 \\
I_{12} &= \frac{I_2 - I_1}{a_1^2 - a_2^2}
\end{aligned} \tag{B.1}$$

$$\begin{aligned}
I_{13} &= \frac{I_3 - I_1}{a_1^2 - a_3^2} \\
I_{23} &= \frac{I_3 - I_2}{a_2^2 - a_3^2} \\
I_{11} &= \frac{1}{3}\left(\frac{4\pi}{a_1^2} - I_{12} - I_{13}\right) \\
I_{22} &= \frac{1}{3}\left(\frac{4\pi}{a_2^2} - I_{12} - I_{23}\right) \\
I_{33} &= \frac{1}{3}\left(\frac{4\pi}{a_3^2} - I_{13} - I_{23}\right),
\end{aligned} \tag{B.2}$$

Having defined the above, the Eshelby tensor for an isotropic material in Voigt form is

$$\mathbf{S} = \begin{bmatrix} S_{1111} & S_{1122} & S_{1133} & 0 & 0 & 0 \\ S_{2211} & S_{2222} & S_{2233} & 0 & 0 & 0 \\ S_{3311} & S_{3322} & S_{3333} & 0 & 0 & 0 \\ 0 & 0 & 0 & 2S_{2323} & 0 & 0 \\ 0 & 0 & 0 & 0 & 2S_{3131} & 0 \\ 0 & 0 & 0 & 0 & 0 & 2S_{1212} \end{bmatrix}, \tag{B.3}$$

where the elements ($S_{ijkl}$) are

$$\begin{aligned}
S_{1111} &= \frac{3}{8\pi(1-\nu)} a_1^2 I_{11} + \frac{1-2\nu}{8\pi(1-\nu)} I_1 \\
S_{1122} &= \frac{1}{8\pi(1-\nu)} a_2^2 I_{12} - \frac{1-2\nu}{8\pi(1-\nu)} I_1 \\
S_{1133} &= \frac{1}{8\pi(1-\nu)} a_3^2 I_{13} - \frac{1-2\nu}{8\pi(1-\nu)} I_1 \\
S_{1212} &= \frac{a_1^2 + a_2^2}{16\pi(1-\nu)} I_{12} + \frac{1-2\nu}{16\pi(1-\nu)} (I_1 + I_2) \\
S_{2222} &= \frac{3}{8\pi(1-\nu)} a_2^2 I_{22} + \frac{1-2\nu}{8\pi(1-\nu)} I_2 \\
S_{2211} &= \frac{1}{8\pi(1-\nu)} a_1^2 I_{12} - \frac{1-2\nu}{8\pi(1-\nu)} I_2 \\
S_{2233} &= \frac{1}{8\pi(1-\nu)} a_3^2 I_{23} - \frac{1-2\nu}{8\pi(1-\nu)} I_2 \\
S_{2323} &= \frac{a_2^2 + a_3^2}{16\pi(1-\nu)} I_{23} + \frac{1-2\nu}{16\pi(1-\nu)} (I_2 + I_3)
\end{aligned} \tag{B.4}$$

$$\begin{aligned}
S_{3333} &= \frac{3}{8\pi(1-\nu)}a_3^2 I_{33} + \frac{1-2\nu}{8\pi(1-\nu)}I_3 \\
S_{3311} &= \frac{1}{8\pi(1-\nu)}a_1^2 I_{13} - \frac{1-2\nu}{8\pi(1-\nu)}I_3 \\
S_{3322} &= \frac{1}{8\pi(1-\nu)}a_2^2 I_{23} - \frac{1-2\nu}{8\pi(1-\nu)}I_3 \\
S_{3131} &= \frac{a_1^2+a_3^2}{16\pi(1-\nu)}I_{13} + \frac{1-2\nu}{16\pi(1-\nu)}(I_1+I_3). \qquad \text{(B.5)}
\end{aligned}$$

## B.2 Details of 6 × 6 matrices G and H

The tensors **G** and **H** of Eq. (3.9) are given by

$$\mathbf{G} = \mathbf{C}^* - \mathbf{C}^*\mathbf{S}\mathbf{P}, \text{ and } \mathbf{H} = \mathbf{C}^*\mathbf{S}\mathbf{Q} - \mathbf{C}^*,$$

where

$$\mathbf{P} = \left[\mathbf{C} + (\mathbf{C}^* - \mathbf{C})\mathbf{S}\right]^{-1}(\mathbf{C} - \mathbf{C}^*), \text{ and } \mathbf{Q} = \left[\mathbf{C} + (\mathbf{C}^* - \mathbf{C})\mathbf{S}\right]^{-1}\mathbf{C}^*.$$

In the above equations, **S** is the Eshelby tensor in Voigt form ($6\times 6$ matrix) as given above, and the matrices **C** and $\mathbf{C}^*$ are the stiffness tensors, given also in Voigt form as

$$\mathbf{C} = \frac{E}{(1+\nu)(1-2\nu)}\begin{bmatrix} 1-\nu & \nu & \nu & 0 & 0 & 0 \\ \nu & 1-\nu & \nu & 0 & 0 & 0 \\ \nu & \nu & 1-\nu & 0 & 0 & 0 \\ 0 & 0 & 0 & \frac{1}{2}-\nu & 0 & 0 \\ 0 & 0 & 0 & 0 & \frac{1}{2}-\nu & 0 \\ 0 & 0 & 0 & 0 & 0 & \frac{1}{2}-\nu \end{bmatrix}, \qquad \text{(B.6)}$$

and

$$\mathbf{C}^* = \frac{E^*}{(1+\nu^*)(1-2\nu^*)}\begin{bmatrix} 1-\nu^* & \nu^* & \nu^* & 0 & 0 & 0 \\ \nu^* & 1-\nu^* & \nu^* & 0 & 0 & 0 \\ \nu^* & \nu^* & 1-\nu^* & 0 & 0 & 0 \\ 0 & 0 & 0 & \frac{1}{2}-\nu^* & 0 & 0 \\ 0 & 0 & 0 & 0 & \frac{1}{2}-\nu^* & 0 \\ 0 & 0 & 0 & 0 & 0 & \frac{1}{2}-\nu^* \end{bmatrix}, \qquad \text{(B.7)}$$

where $E$ and $\nu$ are the Young's moduli and Poission's ratio of the outer material, and $E^*$ and $\nu^*$ are the Young's moduli and Poission's ratio of the flaw material.

# Appendix C

# Supplementary materials for Chapter 4

## C.1 $D$ from Eq. (4.10) for even integer $m$

It appears that when $m$ is an even integer, $D_{\mathrm{ff}}$ can be expressed as a function of $J_2$ and $J_3$. Some results for $m > 4$ are given below. We have not investigated this issue further.

$$
\begin{aligned}
D_{\mathrm{ff}}|_{m=6} &= \frac{16}{5005}(49J_2^3 - 27J_3^2) \\
D_{\mathrm{ff}}|_{m=8} &= \frac{128}{85085}(79J_2^4 - 108J_2J_3^2) \\
D_{\mathrm{ff}}|_{m=10} &= \frac{768}{969969}(121J_2^5 - 270J_2^2J_3^2) \\
D_{\mathrm{ff}}|_{m=12} &= \frac{1024}{185910725}(14579J_2^6 - 44820J_2^3J_3^2 + 3645J_3^4)
\end{aligned}
$$

We can also introduce a new symmetrical variable $\zeta = \chi(1-\chi)$, and obtain

$$
\begin{aligned}
D_{\mathrm{ff}}|_{m=2} &= \frac{2}{15}(\sigma_1 - \sigma_3)^2(1-\zeta) \\
D_{\mathrm{ff}}|_{m=4} &= \frac{8}{315}(\sigma_1 - \sigma_3)^4(1-\zeta)^2 \\
D_{\mathrm{ff}}|_{m=6} &= \frac{16}{3003}(\sigma_1 - \sigma_3)^6\left(1 - 3\zeta + \frac{18}{5}\zeta^2 - \zeta^3\right) \\
D_{\mathrm{ff}}|_{m=8} &= \frac{128}{109395}(\sigma_1 - \sigma_3)^8(1-\zeta)\left(1 - 3\zeta + \frac{33}{7}\zeta^2 - \zeta^3\right) \\
D_{\mathrm{ff}}|_{m=10} &= \frac{256}{969969}(\sigma_1 - \sigma_3)^{10}(1-\zeta)^2\left(1 - 3\zeta + \frac{19}{3}\zeta^2 - \zeta^3\right)
\end{aligned}
$$

$$D_{\text{ff}}|_{m=12} = \frac{1024}{16900975}(\sigma_1 - \sigma_3)^{10}\left(1 - 6\zeta + \frac{225}{11}\zeta^2 - \frac{400}{11}\zeta^3 + \frac{350}{11}\zeta^4 - \frac{126}{11}\zeta^5 + \zeta^6\right)$$

## C.2 Mathematical details of the large $m$ approximation

We note that our proposed dissipation mechanism is shear driven. Therefore, the dissipation for large $m$ would be due to the maximum shear $(\sigma_1 - \sigma_3)$ and the contributions from other shear stress components can be neglected. In Fig. 4.2 we see that the maximum shear is at $\theta = \pi/4$ and $\phi = 0$ (*i.e.* $\widehat{n} = (1/\sqrt{2}, 0, \pm 1/\sqrt{2})$). Using this fact we have used Laplace's method to determine the large $m$ approximation of the integral. We briefly present the calculations below.

We first rewrite the integral in Eq. (4.10) as

$$I(m,\chi) = \int_0^{2\pi}\int_0^{\frac{\pi}{2}} e^{\frac{m}{2}\log(\overline{\tau}^2)} \sin\theta d\theta d\phi. \tag{C.1}$$

The above integral can be looked upon as a more general integral of the form

$$I(m,\chi) = \int_a^b\int_c^d e^{-mf_1(\chi;\,\theta,\phi)} f_2(\chi;\,\theta,\phi) d\theta d\phi. \tag{C.2}$$

Here $f_1(\chi;\,\theta,\phi)$ has minimum at $\theta = \pi/4$ and $\phi = 0$ or $\pi$ (minimum because a minus sign is introduced in Eq. (C.2)). We approximate the integral about one critical point ($\phi = 0$) and later the result is multiplied by 2 to compensate for the other critical point ($\phi = \pi$). To obtain the asymptotic approximation both $f_1$ and $f_2$ are replaced by local Taylor approximations of appropriate degree about the critical point ($\theta = \pi/4 + \zeta$ and $\phi = 0 + \eta$). Now for large $m$, the main contribution to the integral comes from a small neighborhood of the critical point only, therefore the integral limit can be taken as $-\infty$ to $\infty$.

To illustrate, let the Taylor expansion of $f_1$ be written as

$$\begin{aligned} f_1 &\sim \alpha_0 + \alpha_1\zeta^2 + \beta_1\eta^2 + \alpha_2\zeta^3 + \beta_2\eta^3 + \alpha_3\zeta^4 + \beta_3\eta^4 + \dots \\ &= (\alpha_0 + \alpha_1\zeta^2 + \beta_1\eta^2) + g_1(m,\chi;\zeta,\eta) \end{aligned} \tag{C.3}$$

where, $\alpha_k$ and $\beta_k$ are functions of $m$ and $\chi$. A truncated Taylor expansion of $f_2$ gives some other function $g_2(\chi;\zeta,\eta)$. Therefore, the integral in Eq. (C.2)) becomes

$$I(m,\chi) \sim \int_{-\infty}^{\infty}\int_{-\infty}^{\infty} e^{-m(\alpha_0+\alpha_1\zeta^2+\beta_1\eta^2)} h_1(m,\chi;\zeta,\eta)d\zeta d\eta, \tag{C.4}$$

where

$$h_1(m,\chi,\zeta,\eta) = e^{-mg_1(m,\chi;\zeta,\eta)} g_2(\chi;\zeta,\eta).$$

We now Taylor expand $h_1(m,\chi;\zeta,\eta)$ and evaluate the integral in Eq. (C.4)). Note that for each Taylor expansion we need to keep sufficiently many terms for getting the higher-order correction terms.

Using the above method for the leading-order approximation of Eq. (C.1) we get

$$\begin{aligned} I(m,\chi) &\sim \frac{2}{2^m}\int_{-\infty}^{\infty}\int_{-\infty}^{\infty} e^{-m(\alpha_1\zeta^2+\beta_1\eta^2)}\frac{1}{\sqrt{2}}d\zeta d\eta \\ &= \frac{1}{2^m}\times\frac{2\pi}{m\sqrt{2\alpha_1\beta_1}}. \end{aligned} \tag{C.5}$$

In our specific case, $\alpha_1 = 2$ and $\beta_1 = \chi(1-\chi)$. A higher-order approximation including the correction terms is

$$I(m,\chi) \sim \frac{2\pi}{m2^{m+1}\sqrt{\chi(1-\chi)}}\left(1+\frac{6\chi^2-6\chi+1}{4m\chi(1-\chi)}+\frac{68\chi^4-136\chi^3+116\chi^2-48\chi+9}{32m^2\chi^2(1-\chi)^2}\right) \tag{C.6}$$

### C.2.1 Corrections terms for $\chi = 0$ or $1$

For $\chi = 0$ the integral of Eq. (4.10) is just

$$I(m,0) = \int_0^{2\pi}\int_0^{\frac{\pi}{2}} \sin^m\theta\cos^m\theta\sin\theta d\theta d\phi \tag{C.7}$$

which is a Beta function. However, to develop a series along the above lines, we can rewrite Eq. (C.7) as

$$I(m,0) = \frac{1}{2^m}\int_0^{2\pi}\int_0^{\frac{\pi}{2}} e^{m\log(\sin 2\theta)}\sin\theta d\theta d\phi. \tag{C.8}$$

We know that the dissipation curve is symmetric about $\chi = 0.5$. Therefore, the integrals in Eq. (C.7) and Eq. (C.8) are also applied to $\chi = 1$. We now use the approach outlined above for the Laplace's method and get the higher-order approximation of Eq. (C.8) as

$$I(m, 0) \sim \frac{2\pi\sqrt{\pi}}{2^{m+1}\sqrt{m}} \left(1 - \frac{3}{8m} + \frac{25}{128m^2}\right). \tag{C.9}$$

# Appendix D

# Supplementary materials for Chapter 5

## D.1 Torsion of a circular rod

### D.1.1 Analytical calculation

The governing differential equation of torsional vibration of a circular rod is given by

$$I_0 \frac{\partial^2 \phi}{\partial^2 t} = G I_p \frac{\partial^2 \phi}{\partial^2 x} \tag{D.1}$$

where $I_0$ is the mass polar moment of inertia per unit length, $I_p$ is the area polar moment of inertia of the cross section of the rod, and $G$ is the shear modulus of the material. The angular displacement ($\phi$) of the built-in rod (see Fig. D.1) executing first mode of torsional vibration is given by

$$\phi(x,t) = A_1 \sin \frac{\pi x}{2L} \sin \omega t. \tag{D.2}$$

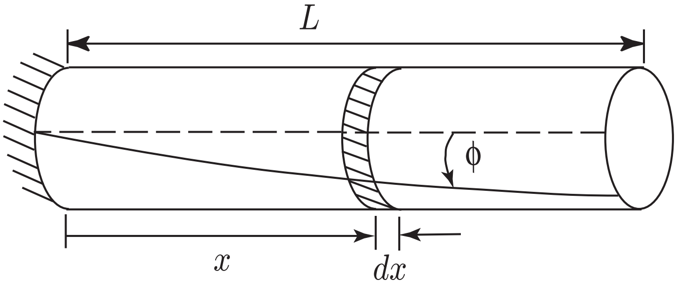

Figure D.1: Pure torsional vibration of a circular rod.

Using Eqs. (D.2) and (D.1), we get the natural frequency of the torsional mode as

$$\omega = \frac{\pi}{2L}\sqrt{\frac{G}{\rho}}, \tag{D.3}$$

where $\rho$ is the mass density of the material. The maximum kinetic energy of this torsional mode is

$$\overline{E} = \frac{1}{2} I_0 \omega^2 \int_0^L A_1^2 \sin^2 \frac{\pi x}{2L} dx = \frac{A_1^2 L I_0 \omega^2}{4}. \tag{D.4}$$

For this pure torsional mode, $\sigma_{eq}^2 = 3\tau^2$, where $\tau$ is the shear stress at a distance $r$ from the neutral axis. The shear stress $\tau$ is given by

$$\tau = \frac{Tr}{I_p},$$

where $T = GI_p \dfrac{\partial \phi}{\partial x}$. The dissipated energy (see Eq. (5.2)) over one cycle is obtained as

$$-\Delta\overline{E} = \xi \int_V \sigma_{eq}^2 dV = \xi \int_V 3\tau^2 dV = 3\xi A_1^2 G^2 I_p \frac{\pi^2}{8L}. \tag{D.5}$$

Using Eqs. (D.4), and (D.5) we obtain the effective damping ratio as

$$\zeta_{\mathit{eff}} = \frac{1}{4\pi} \times \frac{-\Delta\overline{E}}{\overline{E}} = \frac{3G\xi}{2\pi} = \frac{3\xi E}{4\pi(1+\nu)}. \tag{D.6}$$

For $\nu = 0.3$, we get

$$\frac{2\pi\zeta_{\mathit{eff}}}{\xi E} = 1.154 \tag{D.7}$$

### D.1.2 Finite element computations of $\zeta_{\mathit{eff}}$

The finite element model of the circular rod is shown in Fig. D.2. The rod, built-in at one end and free at the other end, is of length 1.0 m and of circular cross section with radius 0.025 m. 29816 elements are used for the mesh. Material properties considered for this model are the same as in Table 5.1. General 3D motions of this rod were considered in the analysis, and so bending, twisting, and stretching modes were all in principle included.

The first few modes of the rod are bending modes (see Table D.1). The seventh

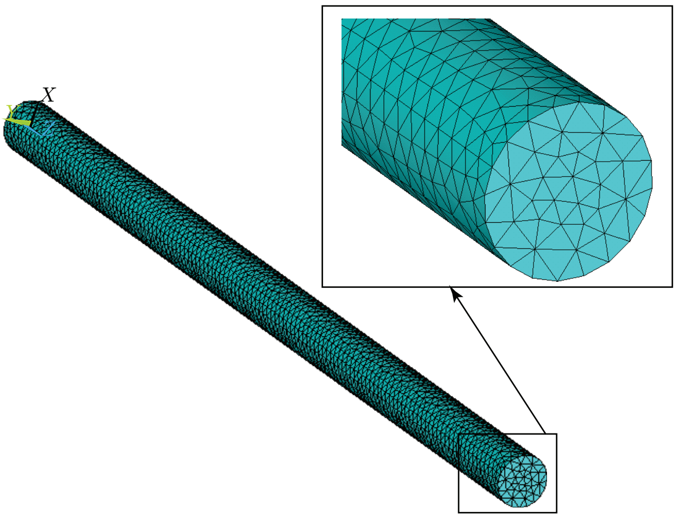

Figure D.2: FE model of the rounded rod.

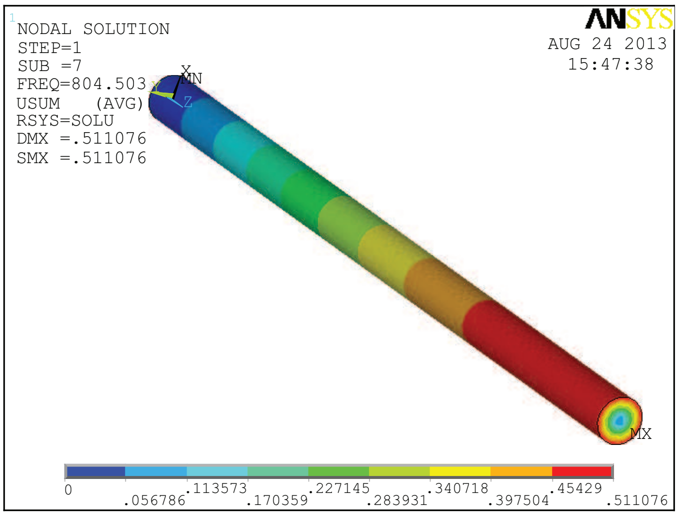

```
NODAL SOLUTION
STEP=1
SUB =7
FREQ=804.503
USUM    (AVG)
RSYS=SOLU
DMX =.511076
SMX =.511076
```

Figure D.3: Mode shape of the torsional mode.

mode for the present geometry happens to be a torsional mode. The lateral modes are basically bending modes and the effective damping ratio (normalized by $\frac{\xi E}{2\pi}$ as mentioned earlier) for those modes are very close to 1[1]. The computed $\frac{2\pi\zeta_{\mathit{eff}}}{\xi E}$ for the torsional mode is 1.154, which matches Eq. (D.7). The mode shape of the torsional mode is shown in Fig. D.3.

---

[1] Wherever the state of stress varies over the body only in terms of a scalar multiple the damping ratios for these cases are found to be the same for $m = 2$. We will also see this below in other examples

| Mode No. | Frequency (Hz) | Numerical $\frac{2\pi\zeta_{eff}}{\xi E}$ | Mode type |
|---|---|---|---|
| 1 | 36.32 | 0.994 | bending mode |
| 2 | 36.32 | 0.994 | bending mode |
| 3 | 225.73 | 0.996 | bending mode |
| 4 | 225.73 | 0.996 | bending mode |
| 5 | 623.88 | 0.998 | bending mode |
| 6 | 623.88 | 0.998 | bending mode |
| 7 | 804.50 | 1.154 | torsional mode |
| 8 | 1200.40 | 1.001 | bending mode |

Table D.1: First eight vibration modes of the circular rod and their corresponding normalized $\zeta_{eff}$ values.

## D.2 Bending of a thin rectangular plate

### D.2.1 Analytical approach

We have used Kirchhoff's plate model for our analytical calculation. The displacement variables of the simply supported rectangular plate (see Fig. D.4), vibrating in its first fundamental mode, are

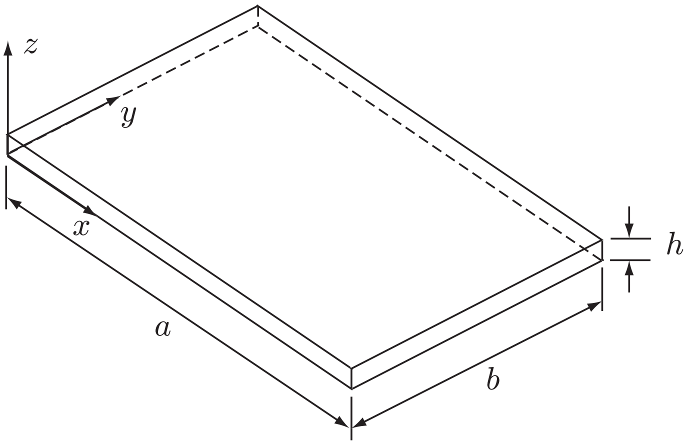

Figure D.4: Thin rectangular plate.

$$
\begin{aligned}
w &= A_1 \sin\frac{\pi x}{a}\sin\frac{\pi y}{b} \\
u &= -z\frac{\partial w}{\partial x} \\
v &= -z\frac{\partial w}{\partial y}.
\end{aligned}
\tag{D.8}
$$

In this case, the strain-displacement relations are

$$\begin{aligned}\epsilon_x &= \frac{\partial u}{\partial x} = \frac{A_1\pi^2}{a^2} z \sin\frac{\pi x}{a}\sin\frac{\pi y}{b}\\ \epsilon_y &= \frac{\partial v}{\partial y} = \frac{A_1\pi^2}{b^2} z \sin\frac{\pi x}{a}\sin\frac{\pi y}{b}\\ \gamma_{xy} = \frac{\partial u}{\partial y} + \frac{\partial v}{\partial x} &= -\frac{2A_1\pi^2}{ab} z \cos\frac{\pi x}{a}\cos\frac{\pi y}{b},\end{aligned} \tag{D.9}$$

and the stress-strain relations are

$$\begin{aligned}\sigma_x &= \frac{E}{1-\nu^2}(\epsilon_x + \nu\epsilon_y)\\ \sigma_y &= \frac{E}{1-\nu^2}(\epsilon_y + \nu\epsilon_x)\\ \tau_{xy} &= \frac{E}{2(1+\nu)}\gamma_{xy}.\end{aligned} \tag{D.10}$$

Here, the out-of-plane normal stress ($\sigma_z$), and shear stresses ($\tau_{yz}$, and $\tau_{zx}$) are assumed to be small, and neglected.

The first and second stress invariants, for this case, turn out to be

$$\begin{aligned}I_1 &= \sigma_x + \sigma_y\\ I_2 &= \sigma_x\sigma_y - \tau_{xy}^2.\end{aligned} \tag{D.11}$$

Now, using Eqs. (D.8), (D.9), (D.10), and (D.11), the dissipated energy over one cycle is obtained as

$$-\Delta\overline{E} = \xi\int_V (I_1^2 - 3I_2)dV = \frac{\xi A_1^2E^2h^3\pi^4(a^2+b^2)^2(1-\nu+\nu^2)}{48a^3b^3(1-\nu^2)^2} \tag{D.12}$$

The total energy is

$$\overline{E} = \frac{1}{2}\int_V(\sigma_x\epsilon_x + \sigma_y\epsilon_y + \tau_{xy}\gamma_{xy})dV = \frac{A_1^2Eh^3\pi^4(a^2+b^2)^2}{96a^3b^3(1-\nu^2)} \tag{D.13}$$

Therefore, we obtain $\zeta_{eff}$ as

$$\zeta_{eff} = \frac{1}{4\pi}\times\frac{-\Delta\overline{E}}{\overline{E}} = \frac{\xi E(1-\nu+\nu^2)}{2\pi(1-\nu^2)}. \tag{D.14}$$

For $\nu = 0.3$, $\dfrac{2\pi\zeta_{eff}}{\xi E}$ turns out to be 0.868.

### D.2.2 Computational solution

The finite element model of the rectangular plate is shown in Fig. D.5. The plate is of dimensions 1.0 m × 0.5 m × 0.005 m. A total of 30559 elements are used in the mesh. Material properties taken for this model are the same as in Table 5.1. Simply supported boundary condition is applied on all the four edges.

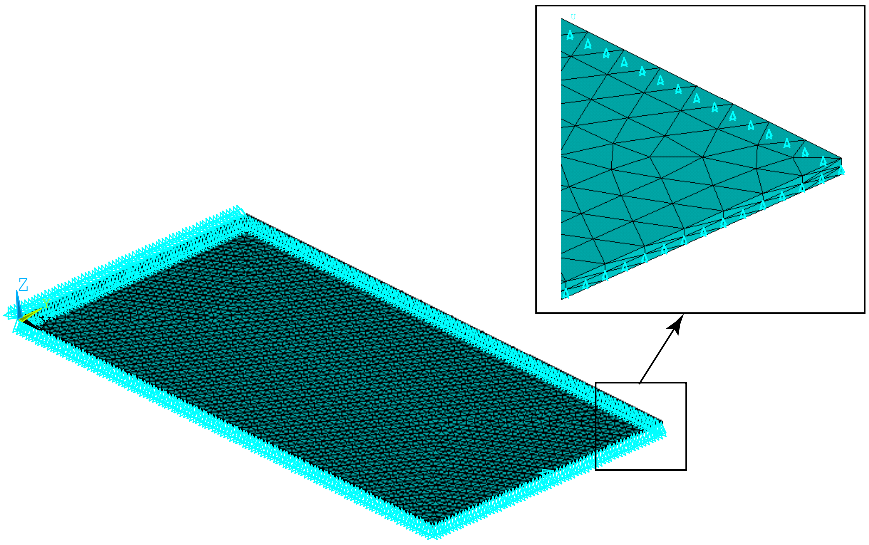

Figure D.5: FE model of the rectangular plate.

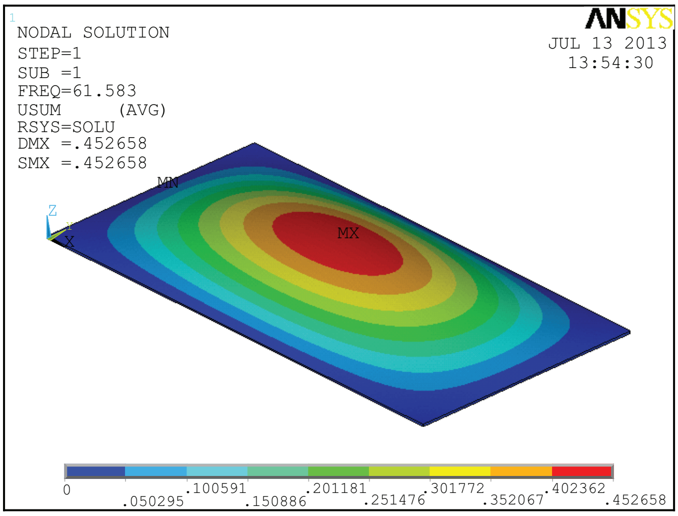

Figure D.6: First vibration mode of the simply supported rectangular plate.

The computed results for the first five modes (see Fig. D.6 for the first mode) of transverse vibration are tabulated in Table. D.2. The computed $\zeta_{\mathit{eff}}$ matches well with the analytical result.

| Mode No. | Frequency (Hz) | Numerical $\frac{2\pi\zeta_{\mathit{eff}}}{\xi E}$ | Mode type |
|---|---|---|---|
| 1 | 61.58 | 0.867 | bending mode |
| 2 | 98.46 | 0.867 | bending mode |
| 3 | 160.05 | 0.867 | bending mode |
| 4 | 209.56 | 0.868 | bending mode |
| 5 | 246.34 | 0.867 | bending mode |

Table D.2: $\zeta_{\mathit{eff}}$ in the transverse vibration of the rectangular plate.

# D.3 Radial mode of a thin-walled spherical shell

## D.3.1 Analytical calculation

A schematic of the radial mode vibration of a thin-walled spherical shell is shown in Fig. D.7. For this vibration mode, the stresses in the radial and hoop directions are the principal stresses and are identical by symmetry. Therefore, the state of stress (or strain) are

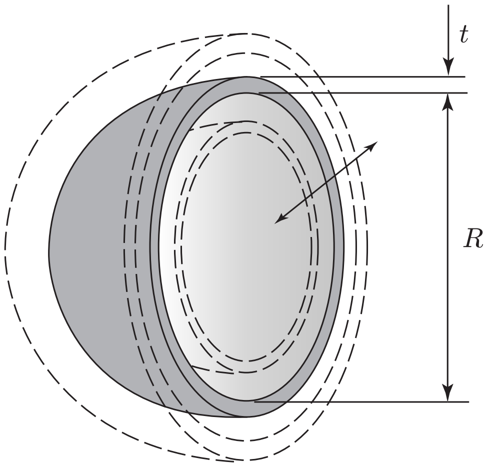

Figure D.7: Radial mode vibration of thin-walled spherical shell (half of the sphere is shown).

$$\epsilon_1 = \epsilon_2 = \epsilon \ ; \ \sigma_1 = \sigma_2 = \sigma \ ; \ \sigma_3 = 0,$$

which gives

$$\sigma = \frac{E\epsilon}{(1-\nu)}. \tag{D.15}$$

The first and second stress invariants, for this case, are

$$I_1 = \sigma_1 + \sigma_2 + \sigma_3 = \frac{2E\epsilon}{(1-\nu)}$$

$$I_2 = \sigma_1\sigma_2 + \sigma_2\sigma_3 + \sigma_3\sigma_1 = \frac{E^2\epsilon^2}{(1-\nu)^2} \tag{D.16}$$

The equivalent stress is calculated using

$$\sigma_{eq}^2 = I_1^2 - 3I_2 = \frac{E^2\epsilon^2}{(1-\nu)^2}. \tag{D.17}$$

Maximum strain energy ($SE_{max}$) over one cycle of vibration is

$$SE_{max} = \frac{I_1^2}{2E} - \frac{(1+\nu)I_2}{E} = \frac{E\epsilon^2}{(1-\nu)}. \tag{D.18}$$

Now, using Eqs. (D.17), and (D.18), we obtain $\zeta_{eff}$ as

$$\zeta_{eff} = \frac{1}{4\pi} \times \frac{\int_V \xi\sigma_{eq}^2 dV}{\int_V SE_{max} dV} = \frac{\xi E}{4\pi(1-\nu)}.$$

For $\nu = 0.3$, $\frac{2\pi\zeta_{eff}}{\xi E}$ turns out to be 0.714.

### D.3.2 Computational solution

The finite element model of a thin-walled spherical shell is shown in Fig. D.8. The spherical shell is of mean diameter 4 m and thickness 0.1 m. Material properties taken for this model are the same as in Table 5.1. Total number of elements in the mesh is 8488. The element size is on the order of the wall thickness. This does not affect us adversely in this particular calculation because our primary interest is in the uniform radial breathing mode.

It turns out that the 108th mode is the uniform breathing radial mode (see Fig. D.9). For that mode we find the $\frac{2\pi\zeta_{eff}}{\xi E}$ is 0.714, which matches well with the analytical result.

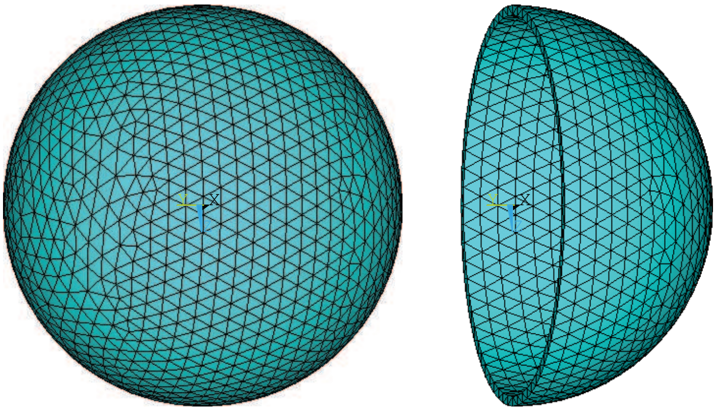

Full model Half portion

Figure D.8: FE model of the thin sphere.

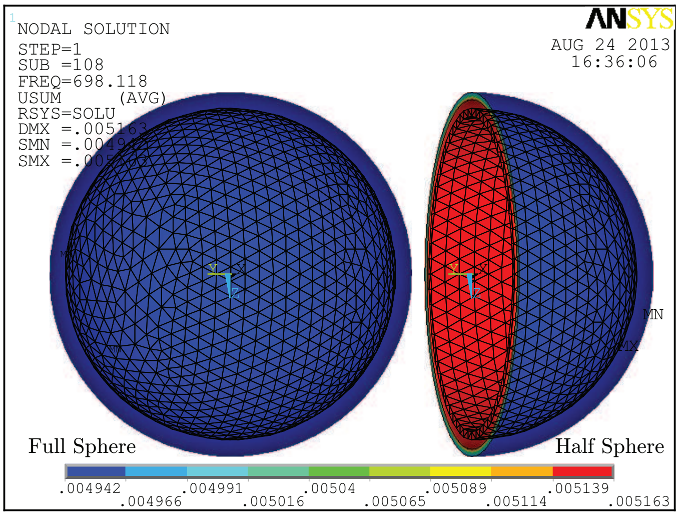
1
NODAL SOLUTION
STEP=1
SUB =108
FREQ=698.118
USUM (AVG)
RSYS=SOLU
DMX =.005163
SMN =.004942
SMX =.005163
ANSYS
AUG 24 2013
16:36:06
Y
X
Z
Y
X
Z
MN
MN
MX
Full Sphere
Half Sphere
.004942
.004966
.004991
.005016
.00504
.005065
.005089
.005114
.005139
.005163

Figure D.9: Uniform radial mode vibration of the sphere.

| Mode No. | Frequency (Hz) | Numerical $\dfrac{2\pi\zeta_{eff}}{\xi E}$ | Mode type |
|---|---|---|---|
| 7 to 11 | 304.1 | 1.096 | bending mode |
| 12 to 18 | 363.6 | 1.053 | bending mode |
| 19 to 27 | 395.3 | 1.027 | bending mode |
| 28 to 38 | 425.8 | 1.006 | bending mode |
| 108 | 698.1 | 0.714 | uniform radial mode |

Table D.3: $\zeta_{eff}$ for thin spherical shell.

## D.4 Longitudinal vibration of a laterally constrained rod

### D.4.1 Analytical approach

The rod shown in Fig. D.10 is constrained in $y$ and $z$-directions. Thus, the stress state of the beam is given by

$$\begin{aligned}\sigma_1 &= C(1-\nu)\epsilon_1 \\ \sigma_2 &= \sigma_3 = C\nu\epsilon_1,\end{aligned} \tag{D.19}$$

where

$$C = \frac{E}{(1+\nu)(1-2\nu)}. \tag{D.20}$$

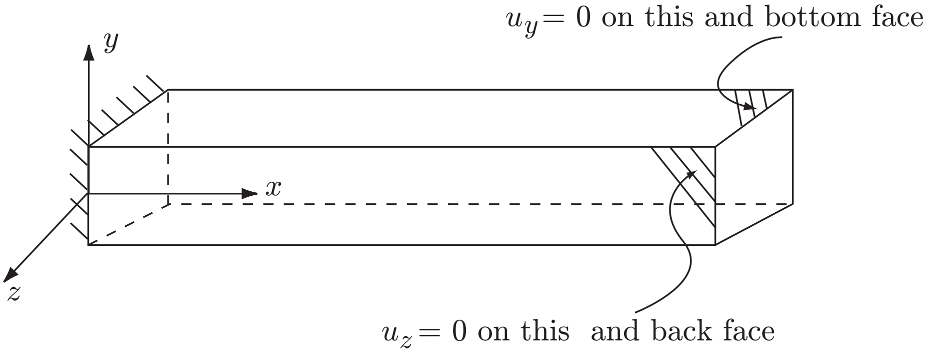
$u_y$= 0 on this and bottom face
$y$
$x$
$z$
$u_z$= 0 on this and back face

Figure D.10: Laterally constrained rod. $u_y = 0$ on the top and bottom faces. $u_z = 0$ on the front and back faces. Displacements are unconstrained in the right most face. The left most face is fixed.

The stress invariants, for this case, are

$$I_1 = \sigma_1 + \sigma_2 + \sigma_3 = C\epsilon_1(1+\nu)$$

$$I_2 = \sigma_1\sigma_2 + \sigma_2\sigma_3 + \sigma_3\sigma_1 = C^2\epsilon_1^2(2\nu - \nu^2). \tag{D.21}$$

Therefore, the equivalent stress is

$$\sigma_{eq}^2 = I_1^2 - 3I_2 = C^2\epsilon_1^2(1-2\nu)^2. \tag{D.22}$$

Maximum strain energy ($SE_{max}$) over one cycle of oscillation is

$$SE_{max} = \frac{I_1^2}{2E} - \frac{(1+\nu)I_2}{E} = \frac{C^2\epsilon_1^2}{2E}(1-\nu^2)(1-2\nu). \tag{D.23}$$

Now, using Eq. (D.22) and Eq. (D.23), we obtain $\zeta_{eff}$ as

$$\zeta_{eff} = \frac{1}{4\pi} \times \frac{\int_V \xi\sigma_{eq}^2 dV}{\int_V SE_{max} dV} = \frac{\xi E(1-2\nu)}{2\pi(1-\nu^2)}. \tag{D.24}$$

For $\nu = 0.3$, we get $\dfrac{2\pi\zeta_{eff}}{\xi E} = 0.440$.

## D.4.2 Computational solution

A 15 m × 1 m × 1 m rod is modeled in ANSYS. Material properties taken for this model are the same as in Table 5.1. The FE model is shown in Fig. D.11. The model is built-in at one end and laterally constrained. The FE model has 17919 elements.

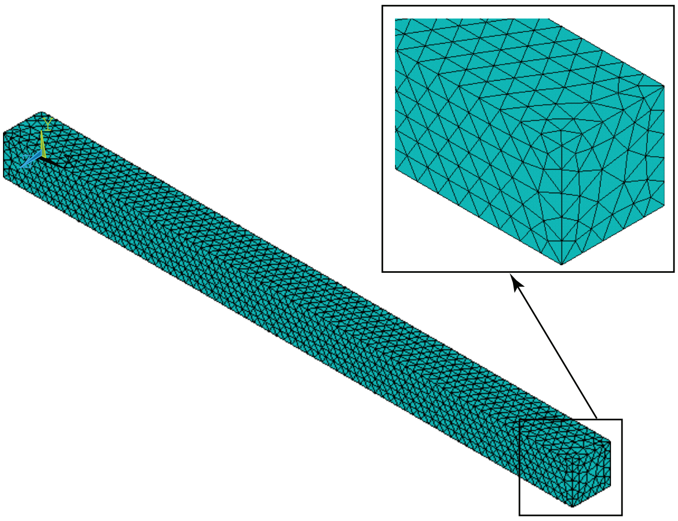

Figure D.11: FE model of the laterally constrained rod.

The calculated $\dfrac{2\pi\zeta_{eff}}{\xi E}$ using this model turns out to be 0.440, which matches the analytical result. The first mode shape is shown in Fig. D.12.

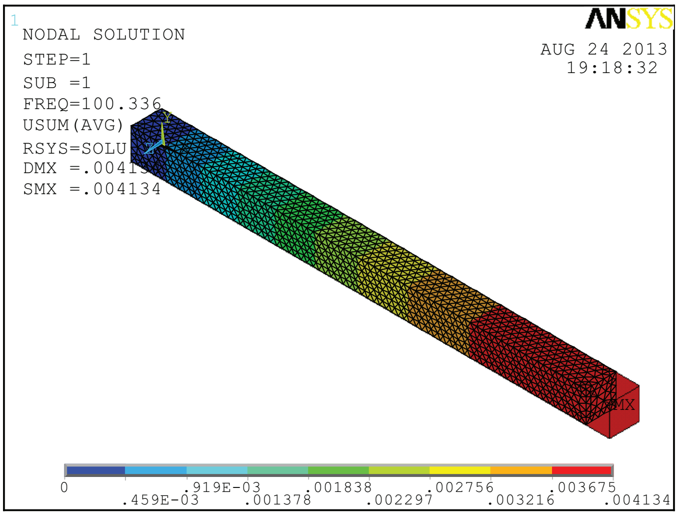

Figure D.12: First mode of the laterally constrained rod.

# D.5 First radial mode of a solid sphere

## D.5.1 Analytical calculation for the radial mode

Here, we compute the frequency as well as the effective damping ratio of a solid sphere when it executes a purely radial mode of vibration. Fig. D.13 shows a schematic representation of the radial mode oscillation.

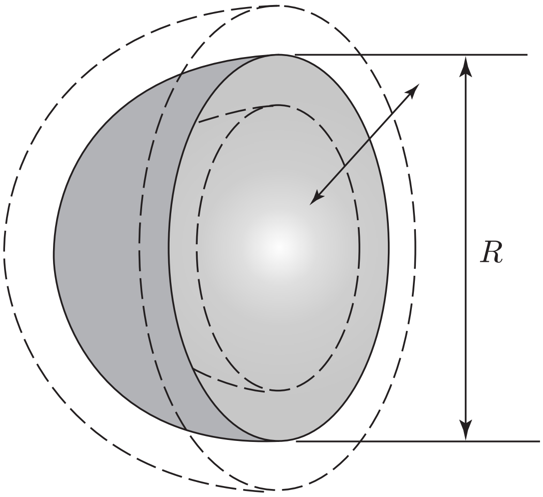

Figure D.13: Radial mode vibration of solid sphere (half of the sphere is shown).

Fig. D.14 represents the free body diagram of a small elemental volume for the radial mode of vibration. Carrying out force balance in the radial direction (assuming radially outward forces as positive) we write

$$\begin{aligned}\rho r^2 \Delta\theta\,\Delta\phi\,\Delta\,r\,\ddot{u} &= -2\sigma_t\left(r+\frac{\Delta r}{2}\right)\Delta\phi\,\Delta r\,\Delta\theta - \sigma_r r^2 \Delta\theta\,\Delta\phi \\ &\quad + \left(\sigma_r + \frac{\partial \sigma_r}{\partial r}\Delta r\right)(r+\Delta r)^2 \Delta\theta\,\Delta\phi. \qquad \text{(D.25)}\end{aligned}$$

Here, $u$ is the displacement in the radial direction. Assuming a harmonic solution ($\ddot{u} = -\omega^2 u$) and eliminating the higher order terms we obtain

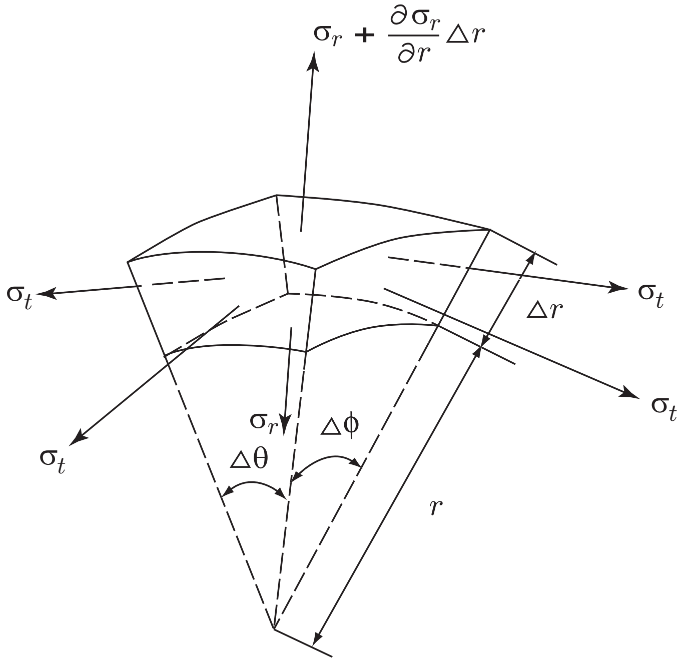

Figure D.14: Free body diagram of the element.

$$-2\sigma_t + 2\sigma_r + r\frac{\partial \sigma_r}{\partial r} + \rho r \omega^2 u = 0. \qquad \text{(D.26)}$$

The stress-strain relations for the radial mode of vibration are

$$\epsilon_r = \frac{\sigma_r}{E} - 2\nu\frac{\sigma_t}{E} \text{ and } \epsilon_\theta = \frac{(1-\nu)\sigma_t}{E} - \nu\frac{\sigma_r}{E}. \qquad \text{(D.27)}$$

The strain-displacement relations are

$$\epsilon_r = \frac{\partial u}{\partial r} \text{ and } \epsilon_\theta = \frac{u}{r}. \qquad \text{(D.28)}$$

Combining Eqs. (D.26), (D.27), and (D.28) we get a partial differential equation (PDE) involving $u(r)$ as

$$r\frac{\partial^2 u}{\partial r^2}+2\frac{\partial u}{\partial r}+\frac{2}{r}u+\frac{\rho\omega^2 r(1-\nu-2\nu^2)}{E(1-\nu)}u=0. \tag{D.29}$$

The boundary conditions for the above PDE are

$$u(0)=0,\ \text{and}\ \sigma_r(R)=0. \tag{D.30}$$

Now, we need to solve Eq. (D.29) with the boundary conditions in Eq. (D.30). It is difficult to obtain the solution in algebraic form. So, we solve Eq. (D.29) with $R = 1$ m and the material properties of Table 5.1. The calculations are carried out using the symbolic computation software Maple. Long symbolic calculations are not reproduced here for reasons of space. The calculated values for frequency and effective damping ratio are (details skipped)

$$\omega = 16075.18\,\text{rad/sec},$$

and

$$\frac{2\pi\zeta_{\mathit{eff}}}{\xi E}=0.114. \tag{D.31}$$

## D.5.2 Computational solution

A solid sphere with 1 m radius is modeled in ANSYS. The finite element model is shown in Fig. D.15. Total number of elements in the model is 10457. Material properties used for this model are the same as in Table 5.1.

Effective damping ratios have been calculated for 50 modes of unconstrained vibrations of the sphere. The first six modes are rigid body modes. The 7th to 33rd modes are not purely radial. Numerical results are reported in Table D.4. The $34^{\text{th}}$ mode is a purely radial mode. The radial mode ($34^{\text{th}}$) and a twisting mode ($7^{\text{th}}$) are shown in Figs. D.16 and D.17 respectively.

For the radial mode we find,

$$\frac{2\pi\zeta_{\mathit{eff}}}{\xi E}=0.114 \tag{D.32}$$

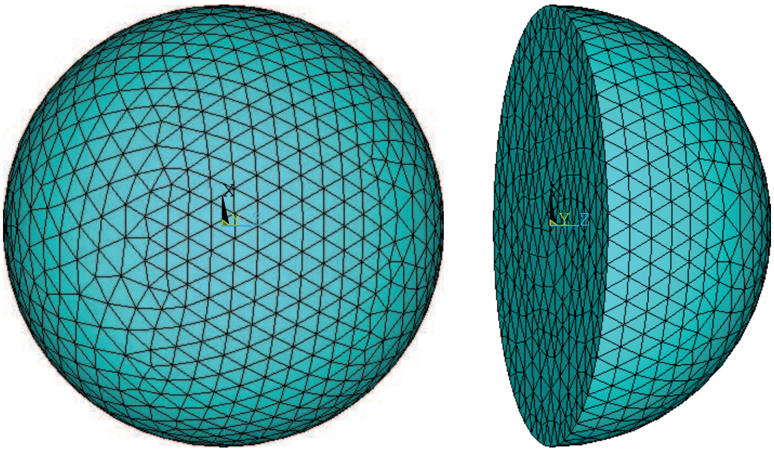

Full model Half portion

Figure D.15: FE model of the solid sphere.

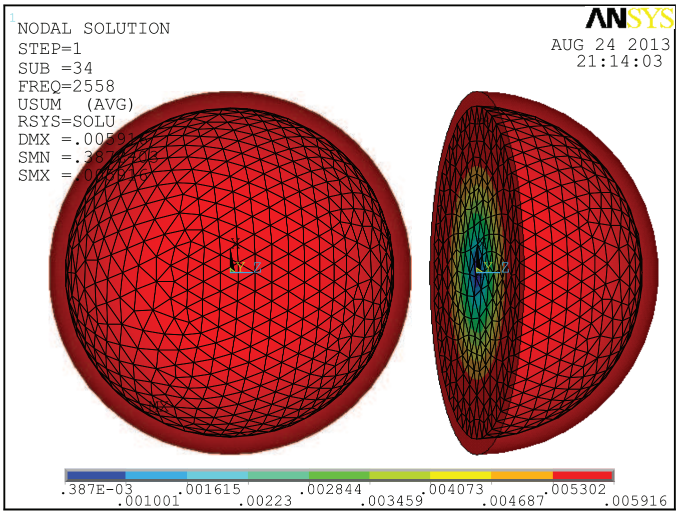
1
NODAL SOLUTION
STEP=1
SUB =34
FREQ=2558
USUM (AVG)
RSYS=SOLU
DMX =.005916
SMN =.387E-03
SMX =.005916
ANSYS
AUG 24 2013
21:14:03
X
Y
Z
MX
.387E-03
.001001
.001615
.00223
.002844
.003459
.004073
.004687
.005302
.005916

Figure D.16: Radial mode of the solid sphere.

which matches Eq. (D.31).

The $\zeta_{eff}$ for this radial mode is the lowest among all the cases we have studied so far (either analytically or numerically). This may be a consequence of considering the fact that the damping is based on the distortional strain energy. If there is damping associated with volumetric strain, then this damping estimate will be higher. It is interesting that the damping value for the twisting mode equals that for twisting of a circular rod (Fig. D.17).

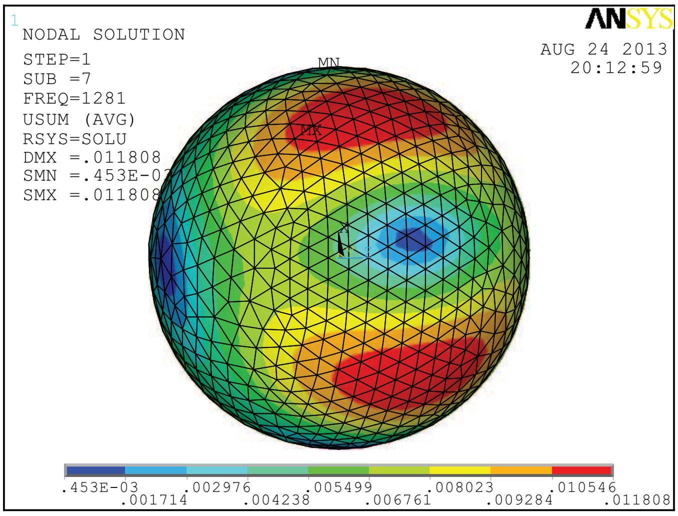
1
NODAL SOLUTION
STEP=1
SUB =7
FREQ=1281
USUM (AVG)
RSYS=SOLU
DMX =.011808
SMN =.453E-03
SMX =.011808
ANSYS
AUG 24 2013
20:12:59
MN
MX
X
Y
Z
.453E-03
.001714
.002976
.004238
.005499
.006761
.008023
.009284
.010546
.011808

Figure D.17: Twisting mode of the solid sphere.

| Mode No. | Frequency (Hz) | Numerical $\dfrac{2\pi\zeta_{eff}}{\xi E}$ | Mode type |
|---|---|---|---|
| 7 to 11 | 1281.0 | 1.154 | twisting modes |
| 12 to 16 | 1355.2 | 1.136 | bending and twisting modes |
| 17 to 19 | 1808.0 | 0.923 | bending modes |
| 20 to 26 | 1979.5 | 1.154 | twisting modes |
| 27 to 33 | 2016.9 | 1.113 | bending and twisting modes |
| 34 | 2558.4 | 0.114 | pure radial mode |
| 35 to 39 | 2565.0 | 0.934 | bending modes |

Table D.4: $\zeta_{eff}$ for solid sphere.

# References

ABAQUS Inc., (2009), *ABAQUS Analysis User's Manual*, Release 6.9 Documentation for ABAQUS.

Abu Al-Rub, R. K. and Palazotto, A. N., (2010), Micromechanical, theoretical, and computational modeling of energy dissipation due to nonlinear vibration of hard ceramic coatings with microstructural recursive faults, *International Journal of Solids and Structures*, **47**, 2131–2142.

Adhikari, S., (2001), Classical normal modes in nonviscously damped linear systems, *AIAA Journal*, **39(5)**, 978–980.

Aleshin, V. and Abeele, K. V. D., (2007), Friction in unconforming grain contacts as a mechanism for tensorial stress-strain hysteresis, *Journal of the Mechanics and Physics of Solids*, **55**, 765–787.

ANSYS Inc., (2009), *ANSYS Reference Manual*, Release 12.1 Documentation for ANSYS.

Barber, J. R., (2011), Frictional systems subjected to oscillating loads, *Annals of Solid and Structural Mechanics*, **2**, 45–55.

Barber, J. R., Davies, M. and Hills, D. A., (2011), Frictional elastic contact with periodic loading, *International Journal of Solids and Structures*, **48**, 2041–2047.

Barquins, M., (1985), Sliding friction of rubber and Schallamach waves - A review, *Materials Science and Engineering*, **73**, 45–63.

Bathe, K. J., (1996), *Finite Element Procedures*, New Jersey: Prentice-Hall.

Bathe, K. J. and Dvorkin, E. N., (1985), A four-node plate bending element based on mindlin/reissner plate theory and a mixed interpolation, *International Journal for Numerical Methods in Engineering*, **21**, 367–383.

Bathe, K. J. and Dvorkin, E. N., (1986), A formulation of general shell elements - the use of mixed interpolation of tensorial components, *International Journal for Numerical Methods in Engineering*, **22**, 697–722.

Dawson, T. H., (1978), Continuum description of hysteresis damping of vibration, *International Journal of Solids and Structures*, **14**, 457–464.

Deshpande, V. S. and Evans, A. G., (2008), Inelastic deformation and energy dissipation in ceramics: A mechanism-based constitutive model, *Journal of the Mechanics and Physics of Solids*, **56**, 3077–3100.

Dvorkin, E. N., (1982), *On nonlinear finite element analysis of shell structures*, Ph.D Thesis, Massuchusetts Institute of Technology.

Dvorkin, E. N. and Bathe, K. J., (1984), A continuum mechanics based four-node shell element for general nonlinear analysis, *Engineering Computations*, **1**, 77–88.

Eshelby, J. D., (1957), The determination of the elastic field of an ellipsoidal inclusion, and related problems, *Proceedings of Royal Society of London* A, **241**, 376–396.

Granato, A. and Lücke, K., (1956), Theory of mechanical damping due to dislocations, *Journal of Applied Physics*, **27**, 583–593.

Holmes, M. H., (1995), *Introduction to Perturbation Methods*, New York: Springer-Verlag.

Hooker, R. J., (1969), Equivalent stresses for representing damping in combined stress, *Journal of Sound and Vibrations*, **10(1)**, 62–70.

Hooker, R. J., (1981), Damping in metals under combined stress loading, *Journal of Sound and Vibration*, **79(2)**, 243–262.

Hooker, R. J. and Mead, D. J., (1981), An apparatus for determination of the effect of mean strain on damping, *Journal of Physics E: Scientific Instruments*, **14**, 202–207.

Hooker, R. J. and Foster, C. G., (1995), A technique for biaxial damping measurement, *Journal of Sound and Vibration*, **188(1)**, 55-73.

Jana, P. and Chatterjee, A., (2013), Modal damping in vibrating objects via dissipation from dispersed frictional microcracks, *Proceedings of the Royal Society* A, **469: 20120685**.

Jang, Y. H. and Barber, J. R., (2011a), Frictional energy dissipation in materials containing cracks, *Journal of the Mechanics and Physics of Solids*, **59**, 583–594.

Jang, Y. H. and Barber, J. R., (2011b), Effect of phase on the frictional dissipation in systems subjected to harmonically varying loads, *European Journal of Mechanics A/Solids*, **30**, 269–274.

Johnson, N. L., Kotz, S. and Balakrishnan, N., (1994), *Continuous Univariate Distributions Vol. 1, 2nd ed.*, New York: Wiley. Published by Society of Automotive Engineers Inc., October 2002.

Kachanov, M., (1987), Elastic solids with many cracks: A simple method of analysis, *International Journal of Solids and Structures*, **23(1)**, 23–43.

Khan, A. S. and Huang, S., (1995), *Continuum Theory of Plasticity*, New York: John Wiley and Sons.

Kimball, A. L. and Lovell, D. E., (1927), Internal friction in solids, *Physical Review*, **30**, 948–959.

Lazan, B. J., (1968), *Damping of Materials and Members in Structural Mechanics*, New York: Pergamon Press.

Lord Kelvin (W. Thomson), (1865), On the elasticity and viscosity of metals, *Proceedings of the Royal Society of London*, **14**, 289–297.

Mallik, A. K. and Ghosh, A., (1973), Improvement of damping characteristics of structural members with high damping elastic inserts, *Journal of Sound and Vibration*, **27(l)**, 25–36.

Malvern, L. E., (1969), *Introduction to the Mechanics of a Continuous Medium*, New Jersey: Prentice-Hall.

Maslov, K. and Kinra, V. K., (2005), Amplitude-frequency dependence of damping properties of carbon foams, *Journal of Sound and Vibration*, **282**, 769–780.

Mead, D. J. and Mallik, A. K., (1976), Material damping under random excitation, *Journal of Sound and Vibration*, **45**, 487–494.

Mentel, T. J. and Chi, S. H., (1964), Experimental study of dilatational- versus distortional-straining action in material-damping production, *The Journal of the Acoustical Society of America*, **36(2)**, 357–365.

Mura, T., (1987), *Micromechanics of Defects in Solids, 2nd ed.*, Dordrecht, Netherlands: Martinus Nijhoff.

Muravskii, G. V., (2004), On frequency independent damping, *Journal of Sound and Vibration*, **274**, 653-68.

Putignano, C., Ciavarella, M. and Barber, J. R., (2011), Frictional energy dissipation in contact of nominally flat rough surfaces under harmonically varying loads, *Journal of the Mechanics and Physics of Solids*, **59**, 2442–2454.

Robertson, J. M. and Yorgiadis, A. J., (1946), Internal friction in engineering materials, *Transactions of the American Society of Mechanical Engineers*, **68**, A173–A182.

Rowett, F. E., (1914), Elastic hysteresis in steel, *Proceedings of the Royal Society of London* A,**89(614)**, 528–543.

Spitas, C., (2009), A continuous piecewise internal friction model of hysteresis for use in dynamical simulations, *Journal of Sound and Vibration*, **324**, 297-316.

Soong, T. T., (2004), *Fundamentals of Probability and Statistics For Engineers*, West Sussex, England: John Wiley and Sons Ltd.

Timoshenko, S. P. and Goodier, J. N., (1951), *Theory of Elasticity*, New York: McGraw-Hill Book Company.

Torvik, P. J., Chi, S. H. and Lazan, B. J., (1963), Damping of materials under biaxial stress, *Wright-Patterson Air Force Base Technical Documentary Report*, **No. ASD-TDR-62-1030**.

Whittier, J. S., (1962), Hysteretic damping of structural materials under biaxial dynamic stresses, *Experimental Mechanics*, **2(11)**, 321–328.

Xiaomin, D., (1994), An asymptotic analysis of stationary moving cracks with frictional contact along bimaterial interfaces and in homogeneous solids, *International Journal of Solids and Structures*, **31**, 2407–2429.

# Curriculum Vitae

## Prasun Jana

PhD student, IIT Kharagpur.

### Education:

**MS**–(2005): Aerospace Engineering: Indian Institute of Technology, Madras.
**BE**–(2002): Mechanical Engineering: Bengal Engineering College, Shibpur.

### Professional Experience:

**General Electric**, JFWTC, Bangalore: (2007 – 2010).
Position held: Engineer/Technologist.
Major Responsibilities: Design and analysis of wind turbine blades. Ownership of an inhouse Matlab and ANSYS based structural simulation tool.

**Indian Space Research Organization**, Trivandrum: (2005 – 2007).
Position held: Scientist/Engineer-'SC'.
Major Responsibilities: Design and analysis of composite structures for spacecraft components. Generation of fabrication drawings and process documents.

### Publications:

**Based on PhD work:**

1. Jana, P. and Chatterjee, A., An internal damping formula derived from dispersed elasto-plastic flaws with Weibull-distributed strengths, submitted to *International Journal of Mechanical Sciences.*

2. Jana, P. and Chatterjee, A., (2013), Modal damping in vibrating objects via dissipation from dispersed frictional microcracks, *Proceedings of the Royal Society* A, 469: 20120685.

3. Jana, P. and Chatterjee, A., (2011), Frictional dissipation at a small crack under multiaxial periodic stresses, *Proceedings of 15th National Conference on Machines and Mechanisms* (NaCoMM), IIT Madras, 232–239.

**Some earlier publications:**

4. Jana, P. and Bhaskar, K., (2007), Analytical solutions for buckling of simply supported rectangular plates under non-uniform biaxial compression or uniaxial compression with lateral restraint, *International Journal of Mechanical Sciences*, 49(10), 1104–1112.

5. Jana, P. and Bhaskar, K., (2007), Analytical solutions for buckling of simply supported rectangular plates due to non-linearly distributed in-plane bending stresses, *Structural Engineering and Mechanics*, 26(2), 151–162.

6. Jana, P. and Bhaskar, K., (2006), Stability analysis of simply supported rectangular plates under non-uniform uniaxial compression using approximate plane stress solution, *Thin-Walled Structures*, 44, 507–516.